GENERATION OF THERMO-ACOUSTIC WAVES FROM PULSED SOLAR/IR RADIATION

by

Aowabin Rahman

A thesis submitted to the faculty of
The University of Utah
in partial fulfillment of the requirements for the degree of

Master of Science

Department of Mechanical Engineering

The University of Utah

May 2014

The University of Utah Graduate School

STATEMENT OF THESIS APPROVAL

The following faculty members served as the supervisory committee chair and members for the thesis of Aowabin Rahman. Dates at right indicate the members' approval of the thesis.

Kuan Chen, Chair	03/17/2014
Geoffrey Silcox, Member	03/17/2014
Kent Udell, Member	03/17/2014

The thesis has also been approved by Tim Ameel, Chair of the Department of Mechanical Engineering and by David B. Kieda, Dean of The Graduate School.

ABSTRACT

Acoustic waves could potentially be used in a wide range of engineering applications; however, the high energy consumption in generating acoustic waves from electrical energy and the cost associated with the process limit the use of acoustic waves in industrial processes. Acoustic waves converted from solar radiation provide a feasible way of obtaining acoustic energy, without relying on conventional nonrenewable energy sources.

One of the goals of this thesis project was to experimentally study the conversion of thermal to acoustic energy using pulsed radiation. The experiments were categorized into “indoor” and “outdoor” experiments, each with a separate experimental setup. The indoor experiments used an IR heater to power the thermo-acoustic lasers and were primarily aimed at studying the effect of various experimental parameters on the amplitude of sound waves in the low frequency range (below 130 Hz). The IR radiation was modulated externally using a chopper wheel and then impinged on a porous solid, which was housed inside a thermo-acoustic (TA) converter. A microphone located at a certain distance from the porous solid inside the TA converter detected the acoustic signals. The “outdoor” experiments, which were targeted at TA conversion at comparatively higher frequencies (in 200 Hz–3 kHz range) used solar energy to power the thermo-acoustic laser.

The amplitudes (in RMS) of thermo-acoustic signals obtained in experiments using IR heater as radiation source were in the 80–100 dB range. The frequency of acoustic waves corresponded to the frequency of interceptions of the radiation beam by the chopper. The amplitudes of acoustic waves were influenced by several factors, including the chopping frequency, magnitude of radiation flux, type of porous material, length of porous material, external heating of the TA converter housing, location of microphone within the air column, and design of the TA converter. The time-dependent profile of the thermo-acoustic signals also showed "transient" behavior, meaning that the RMS amplitudes of TA signals varied over a time interval much greater than the time period of acoustic cycles. Acoustic amplitudes in the range of 75–95 dB were obtained using solar energy as the heat source, within the frequency range of 200 Hz–3 kHz.

TABLE OF CONTENTS

ACKNOWLEDGEMENTS

I would like to acknowledge the contributions of several coworkers who collaborated with this research. I would like to thank my advisor, Dr. Kuan Chen, who provided valuable ideas on theoretical aspects of thermo-acoustics and contributed with practical suggestions on experimental procedures and interpretation of experimental data. I would also like to acknowledge the contributions of Faisal Fathiel, who designed and machined TA converters and the experimental rig for the solar to acoustic energy converter, Dr. NJ Kim, who built the rig for the IR heater, and Mohammad Albonaeem, who helped with the uncertainty analysis of the experimental data.

This work was partially supported by a grant (No. 2011-0029820) from the National Research Foundation of Korea, which is greatly appreciated.

CHAPTER 1

INTRODUCTION

Thermo-acoustic oscillations are pressure oscillations that occur due to temperature variations. Sound waves are generally regarded as a combination of pressure and velocity oscillations of air molecules in space; however, these are coupled with temperature oscillations as well [1]. Conversely, temperature fluctuations in air induced by external sources can cause thermo-acoustic oscillations. The origins of thermo-acoustics can be traced back to 1777, when Bryon Higgins [2] observed that igniting a hydrogen flame inside a tube open at both ends produces sound waves that vary with the position of the flame within the tube. Experiments by Rijke and Sondhass confirmed Higgins' observations, and Lord Rayleigh suggested a qualitative explanation in 1896 [3]:

> "If heat be given to the air at the moment of greatest condensation, or be taken from it at the moment of greatest rarefaction, the vibration is encouraged. On the other hand, if heat be given at the moment of greatest rarefaction, or abstracted at the moment of greatest condensation, the vibration is discouraged."

Thermo-acoustic energy converters are of interest to engineers as they can be used as heat engines, where heat flowing through a porous media is converted to sounds [4], or as heat pumps, where externally generated pressure oscillations are used to transfer heat from a region of lower to higher temperature [4]. These thermo-acoustic devices

are easy to construct, and they do not release greenhouse gases. Thermo-acoustic devices can also be used for refrigeration purposes, particularly for cryogenic applications [5]. Methods of generating large-scale acoustic energy were not explored in great detail in the past, mainly due to concerns about the high cost of generating acoustic energy from electricity as well as potential safety hazards [6]. However, recent developments in solar-powered thermo-acoustic-lasers (TA lasers) [7] and refrigerators driven by waste energy, such as heat from exhaust gases from automobile engines [8,9], or heat from power plants, provided economical means of producing acoustic energy on a large-scale. Employing thermo-acoustic engines and heat pumps in such applications can reduce energy consumption as well as greenhouse gas emissions [10]. As a result, thermo-acoustic systems have recently been considered for industrial applications, such as liquefaction of natural gas and separation of gases [5].

Photo-acoustic oscillations are a type of thermo-acoustic oscillations that are generated when pulsed radiation is incident on a given sample, resulting in localized absorption of radiation within the sample and subsequent heat transfer to the surrounding medium [11]. The periodic nature of heat transfer results in pressure oscillations that can be detected as acoustic waves. The photo-acoustic effect was observed by Alexender Graham Bell, who used the phenomenon in his invention of the "photophone" [12, 13]. Bell's photophone reflected a beam of sunlight using a mirror to a selenium cell, which was connected to an ordinary telephone receiver. While working with the photophone, Bell noticed that mechanically modulating the incident light resulted in sound waves near the sample where light was incident. John Tyndall and Wilhelm Roentgen [14] picked up on Bell's research and proved that this phenomenon

extended to liquids and gases as well. In 1938, M.L Viengrev [15] used the photo-acoustic effect in gas analysis.

The main motivation behind this research was to find an inexpensive and renewable means of generating acoustic energy. Acoustic cleaners and filters, which use the concept of particle agglomeration under the influence of acoustic waves, have found applications in several engineering sectors, including petrochemical, pharmaceuticals, mining, biomedical and manufacturing industries, mainly due to the fact that acoustic cleaners can operate over a wide range of frequencies [16, 17]. Recent research has shown promising results for carbon dioxide capture using acoustically assisted fluidized beds and acoustically excited alkaline droplets [18–23]. However, one major challenge to the large-scale use of acoustic energy in these applications is that generating acoustic waves from electrical energy can be expensive and energy consuming. Thermo-acoustic waves generated from pulsed solar radiation provide a cheap and fairly available means of generating acoustic energy.

This thesis studies the behavior of acoustic oscillations under pulsed radiation and attempts to address some of the limitations of previous research. Acoustic waves generated due to thermal effects have been broadly categorized into two separate disciplines: “photo-acoustics” and “thermo-acoustics.” As mentioned, photo-acoustics is mainly concerned with acoustic generation as a result of periodic heating of a solid by incident radiation, but so far the applications of photo-acoustics have been limited primarily to material detection and characterization. Designs of conventional TA lasers usually involve thermo-acoustic elements called “stacks” placed inside tubes, where the temperature gradient across the stack is used to generate acoustic waves [24]. However,

difficulties in coupling multiple thermo-acoustic lasers (using the "stack-tube" design) limit the maximum acoustic amplitude that could be produced from multiple TA lasers.

Rosencwaig and Gersho developed a mathematical model, often called the RG model [25], which related closely to the experiments presented in this thesis. However, the RG model was primarily developed for material detection, and so it is not fully applicable to our TA laser research. Chapter 3 includes a review of the RG model, explains discrepancies between RG model and our experimental observations, and analyzes numerical simulations in COMSOL to illustrate the discrepancies.

As mentioned, experiments in this thesis aim to generate acoustic waves by periodic radiation on a porous solid. The fundamental difference between photo-acoustic experiments conducted previously and those in this thesis is that the latter attempt to explore the applications of photo-acoustics beyond spectroscopic techniques [26]. As a result, the primary aim of the experiments in this thesis was to achieve high acoustic energy output. Another key objective was to obtain high-frequency acoustic waves from solar energy, so my thesis correspondingly addresses the use of polychromatic radiation.

The experiments conducted in this thesis are, in concept, similar to those designed and conducted by Alexander Bell [13]. The experimental approach involved mechanically chopping the incident radiation by a rotating chopper wheel and impinging the pulsed radiation to a porous material, such as steel wool. The porous material was inserted in an air-tight TA converter, which also contained an air column behind the porous material. As the porous material was periodically heated by incident radiation during the "unchopped" half-cycles, it also heated the air inside the air

column, primarily by conduction. During the "chopped" half-cycles, heat was removed from air by conduction through the aluminum body of the TA-converter and the porous material. Consequently, temperature fluctuations occurred within the air column, resulting in periodic volume changes and thereby creating pressure oscillations. A microphone located at a fixed distance from the porous material measured acoustic signals produced as a result of pressure oscillations. The signals were analyzed in LabVIEW Signal Express 2009 and were converted to decibel scale using calibration tests.

The calibration techniques used were unique to this thesis. Most applications [27] convert microphone voltage to decibel scale using a prespecified sensitivity value at a given frequency. For the two microphones used in this thesis, no specified "sensitivity" values were available. To account for any variation in the sensitivity of microphone 1 with respect to acoustic frequency, the calibration tests were conducted between the frequency range of 100 Hz–3 KHz.

An infrared heater was used as the radiation source to power TA lasers for "indoor experiments." The purpose of the indoor experiments was to study how the acoustic signals were affected by the experimental parameters and design of TA converters. The frequency of the acoustic signals was observed to be equal to the chopping frequency of pulsed IR radiation, thus confirming Bell's observations [13]. The acoustic amplitudes (usually measured and presented in root mean square [RMS] of acoustic signal) were observed to depend upon the chopping frequency, magnitude of radiation flux, type and grade (i.e., porosity/interfilament spacing) of porous material, length of porous material, external heating conditions, location of the microphone

within the air column, and dimensions of the air column and TA converter opening. The acoustic signals were also observed to exhibit "transient" behavior; that is, the acoustic amplitudes were found to initially increase and then decrease over a time interval much greater than the time period of the periodic radiation flux (and thereby the time period of the corresponding acoustic cycle).

The experiments using the IR heater showed that thermo-acoustic oscillations within the SPL range of 80–100 dB could be generated by our TA lasers. The TA converters could then be used for "outdoor" experiments aimed at converting solar to acoustic energy. Components of the setup for outdoor experiments were assembled in a cart (a mobile experimental rig), which included a plastic Frensel lens, chopper wheel, electric motor, solar pyrometer and alignment surface, thermo-acoustic energy converter (TA converter), and data acquisition (NI-DAQ) card. These components were mounted on the cart platform, which was aimed at the sun manually so as to maximize the solar radiation entering the TA converter. Details of the experimental setup, procedures and alignment techniques for "outdoor" experiments are presented in Chapter 4. Corresponding results, including the time-domain TA signals converted from pulsed solar radiation, as well as RMS amplitudes obtained over a wide frequency range (200–3kHz) are presented in chapter 5.

The results obtained in this thesis are significant as they provide a way to produce acoustic energy directly from solar energy, which could then be used for applications such as acoustic cleaning and filtration. Using pulsed radiation allows easy modulation of the frequency of acoustic waves and provides a way of coupling multiple

TA lasers, such that the resulting acoustic wave is higher in amplitude than individual amplitudes of each TA laser.

CHAPTER 2

LITERATURE REVIEW

Most authors distinguish the discipline of photo-acoustics from thermo-acoustics. However, because this thesis focuses on photo-acoustic systems that can be run as thermal to acoustic energy converters, relevant literature from both photo-acoustics and thermo-acoustics are reviewed in this chapter.

2.1 Photo-acoustic oscillations

The idea of using incident electromagnetic radiation to produce audible sound has existed for more than 100 years. Alexander Graham Bell studied the acoustic effect produced by modulated radiation [12, 13] while inventing "An Improved Apparatus for Signaling and Communicating," which he called the "photophone." The photophone was a two-part construction; it included a "photophonic transmitter" and a "receiver." The transmitter included a mechanism (usually a chopper or a grating disc) that interrupted the incident beam. The receiver consisted of a focusing lens, a "sensitive body" and a tube constructed of soft-vulcanized rubber, brass, or soft wood. Bell obtained audible signals using several materials as the "sensitive body," including: hard rubber, gold, platinum, aluminum, iron, steel, antimony, Brass' steam packing, tanner iron, tin foil, brass, copper, German silver, and selenium membranes [12,13].

Bell claimed that the best results were obtained using materials that were in "loose, porous and spongy" conditions and had the "darkest" and "most absorbent" colors. In Bell's experiments, such materials included cotton-wool, worsted, fibrous materials, sponge, lamp black, platinum and "other metals in spongy condition" [12].

In his publications [12, 13], Bell claimed that the reason for observing the photo-acoustic effect was that the periodic intensity of solar radiation changed the "state of strain" of the "sensitive body." According to Bell's hypothesis [13], when the chopper periodically interrupts the incident radiation beam, the "sensitive body" physically expands and contracts in a periodic manner. Bell also suggested that if the vibrational motion of the body possesses a minimum frequency and amplitude, the motion will be "imparted" to the air "surrounding the body." Consequently, an audible signal could be detected, and its loudness would correspond to the sample's amplitude of vibration while its pitch would correspond to its frequency.

Later, John Tyndall and Wilhelm Roentgen extended the study of photo-acoustics to liquids and gases. Tyndall discovered that the intensity of sound produced in a fluid medium was proportional to the intensity of incident light. Viengerov [14] was the first to perform gas analysis using the concept of photo-acoustics, when he designed a gas detection method to measure the concentrations of carbon dioxide and nitrogen in air [14]. Luft [28] made adjustments to Viengrov's techniques and improved the sensitivity of absorption measurement of gaseous samples to a concentration range of ppm (10^{-6}).

Following Viengrov and Luft's publications, the photo-acoustic effect was extensively used for spectroscopic methods, largely owing to the invention of the laser.

The first photo-acoustic experiments with laser beams were conducted by Kerr and Atwood [29]. Patel et al. [30] used CO and CO_2 lasers to measure levels of nitric acid and water vapor in the stratosphere. Further work by Sigrist [31] enabled the photo-acoustic detection of volatile organic compounds such as ethane, propene, formaldehyde, and toluene in car exhaust using lasers of varying frequencies. Sigrist extended his research to solid state lasers that were tunable in the midinfrared range [32] and hypothesized on the main causes of photo-acoustic effect [31]

According to Sigrist [31], any one (or more) of five mechanisms could be responsible for generation of acoustic waves using electromagnetic radiation. These mechanisms were dielectric breakdown, vaporization or material ablation, thermo-elastic process, electro-restriction, and radiation pressure. Sigirist claimed that although dielectric breakdown efficiently converts optical to acoustic energy, the phenomenon is only observed at high radiation intensities, typically of the order $\sim 10^{10} W/cm^2$ [31]. Vaporization and transient transformation of solid samples to a plasma state only occur if the laser intensity within a given sample exceeds a certain threshold value. The fourth mechanism, electrostriction, occurs when local irradiation redistributes molecules within the sample depending upon their ability to polarize under incident radiation. According to Sigrist [31], the effect of radiation pressure is low, and it is a mechanism that can be neglected for most photo-acoustic purposes.

The thermo-elastic process (as hypothesized by Sigirist) was defined as "transient heating" of a "restricted volume" [31], which results in periodic thermal expansion and contraction of a gas volume. Sigirist assumed that the absorption of radiation by a gaseous medium was the primary cause behind the generation of acoustic

waves, but later it was suggested that periodic heat transfer (primarily by conduction) from the heated solid and the surrounding air was responsible of thermo-acoustic generation [25]. Other researchers followed up on Sigrist's work and made improvements to the experimental techniques used for gas analysis using photo-acoustic methods [32–36].

The "photo-acoustic theory in solids," forwarded by Rosencwaig and Gersho [25], is another key literature that relates closely to this thesis. Previously, Mercadier [37] hypothesized that pulsed incident radiation induces periodic heating and cooling in the "gaseous layer adhering" to the solid surface. Rosencwaig and Gersho performed photo-acoustic experiments involving two-dimensional solids and nonabsorbing noble gases [25]. Their most important experimental findings were

(a) The absorption of radiation in gases does not contribute to the generation of acoustic signals.

(b) Physical expansion and contraction of the solid are too small to contribute to acoustic signals.

(c) The pulsed thermal energy incident on the solid is transferred to the surrounding gas, primarily by conduction, which results in temperature fluctuations in the boundary layer near the heated solid surface. The boundary layer acts as a hypothetical "vibrating gas-piston" that is responsible for the acoustic signals.

Rosencwaig and Gersho's model, often termed the RG model, conforms to the theories suggested by Mercadier [37]. The RG model was extended for samples with optically absorbing coatings by Fernelius [38] and for transparent samples by Benett and Forman [39]. McDonald and Wetsel [40] suggested that the mechanical vibrations

due to thermal effects, which were found to be negligible for solid samples, were significant for liquids, and they subsequently proposed a combined model that included photo-acoustic effects in both solids and liquids. Park and Diebold [41] observed the photo-acoustic effect in strongly absorbing fluids.

Currently, photo-acoustic devices continue to be employed in a diverse range of applications, including gas analysis in pollution monitoring [26], biomedical applications [32], and in detection of material properties [25].

2.2 Thermo-acoustic oscillations and thermo-acoustic converters

The production of sound waves by heating effects was discovered in 1777 by Bryon Higgins, who noticed that placing hydrogen flames at an open end produced "singing flames" [42] in the tube. Sondhauss conducted a more comprehensive research on thermo-acoustic oscillations in 1850, using a tube keeping one end open and the other end heated to a high temperature [43]. In 1859, P.L Rijke conducted experiments with open-ended tubes of roughly 0.8 m in length and 30 millimeters in diameter, placing a wire mesh (81 meshes/cm^2) at a distance of about 0.2 m inside the tube [44]. The wire mesh was heated by a hydrogen lamp for a few seconds. This experiment, which later famously came to be known as the "Rijke tube" experiment, produced acoustic waves of considerable amplitude [44]. Rijke suggested that the generation of these acoustic waves was due to the periodic expansion of air, which occurred when air was being heated by the wire mesh, followed by periodic contraction, which occurred when it was being cooled by the inner walls of the tube. According to Rijke, the

convective air current that moved the hot air away from the wire mesh enhanced the thermo-acoustic process.

G. Kirchoff [45] worked on the theoretical aspects of thermo-acoustic waves produced due to oscillating heat transfer between an isothermal wall and a gas. In 1887, Lord Rayleigh [3] expanded on the work of Soundhass and Rijke and suggested a more comprehensive explanation for the thermo-acoustic phenomenon. Like Rijke, Rayleigh [3] claimed the thermo-acoustic effect resulted from a combination of convective air flow and the periodic expansion and contraction of air. According to Rayleigh, air flowed from both directions into the wire mesh as the mesh heated the surrounding air.

Taconis [46] proved that sound waves can also be produced when a tube full of helium is cooled to cryogenic temperatures using liquid nitrogen. N. Rott [47] investigated the theoretical aspects of thermo-acoustics and postulated the "linear thermo-acoustic theory" [47]. Practical applications of thermo-acoustics soon followed, with the first thermo-acoustic refrigerator being developed in 1986 by T.J Hofler. This refrigerator had a cooling power of 6 W and was operated by helium gas at 1020 kPa (10.2 bars) [48]. Garett et al. [49] developed a space thermo-acoustic refrigerator (STAR), which was flown on Space Shuttle Discovery in January 1992, as well as the Thermo-acoustic Life Sciences Refrigerator (TALSR) [49], which was the first thermo-acoustic refrigerator that could be used as a domestic food refrigerator/freezer. TASLR had the ability to pump thermal energy at 0.205 KW (700 Btu/hr) in refrigerator mode [49]. Both these thermo-acoustic refrigerators utilized acoustic waves driven by loudspeakers, to pump heat across a temperature gradient. The thermo-acoustic refrigerators were simple in construction and required no lubrication.

Other research suggested that the placement of the heating element could be important to producing sustained thermo-acoustic waves [50]. Fahey suggested that the rate of heat transfer is directly proportional to the acoustic velocity [50]. According to his research, the maximum temperature gradient at the point of maximum velocity would result in the highest amplitude of acoustic waves. This observation probably resulted in adjustments to the basic Sondhauss tube, such as placing a bundle of Pyrex tubes close to the electric heater on the side closest to the open end [50].

Garett and Backhaus [51] further predicted that thermo-acoustic engines would soon be commonplace and that they could be used to generate electricity and provide domestic space cooling, as their efficiencies were comparable to those of internal combustion engines and they did not have any harmful impact on the environment.

Los Alamos National Laboratory [52] provides a database of previous research carried out in the field of thermo-acoustics. Within this archive, Backhaus and Swift [4] provide an overview of several types of thermo-acoustic (TA) engines and broadly categorized TA engines into travelling-wave and standing-wave types. Wollan et al. [5] achieved an efficiency of 18% with an acoustic output as high as 17 KW, using standing-wave TA engines. Los Alamos National Lab also developed a travelling TA-engine that could reach an efficiency of 30% with acoustic output of 1.75 KW [53].

Thermo-acoustic systems have also been used in separation of gases. Swift and Geller [54,55] suggested a hypothesis for thermo-acoustic separation of gas mixtures, after successfully using thermo-acoustic waves to separate helium-xenon and helium-argon mixtures. According to the authors [54,55], when sound waves are imposed in a duct containing gas mixtures, the gases separate along the length of the duct as a result

of “oscillating thermal diffusion” in the radial direction, combined with “oscillating viscous motion” in the axial direction. Other researchers focused on the use of thermo-acoustic engines in the thermal management in microelectronics [56], the coupling effect of thermo-acoustic lasers [6], the influence of stack design on thermo-acoustic oscillations [57], and the utilization of waste heat from exhaust gases to drive thermo-acoustic engines [58]. Symko et al. [56] proved that by raising the driving acoustic frequency to kHz range (4–24 kHz) and scaling down the dimensions of components, the concepts of thermo-acoustic refrigeration could be applied to achieve effective spot cooling in electronic components [56]. Experiments involving a pair of coupled thermo-acoustic lasers showed that the sound amplitude depends on the phase difference between the TA waves and the distance between the focusing point and the laser output ports [6,59,60]. De Blok developed a thermo-acoustic engine, with an operating range of 70–200°C that could recover waste heat [58].

Like most of the previous research on conventional thermo-acoustic engines, this thesis attempts to generate high amplitude acoustic waves. However, unlike previous research, the frequency was modulated externally by a rotating chopper wheel. Modulating acoustic frequency by chopping incident radiation is fairly simple compared to other methods of modulating frequency. This is because in the case of thermo-acoustic waves generated by pulsed radiation, acoustic frequency is equal to the chopping frequency and is independent of the dimensions of the medium where the TA signals are generated. Previously, Chen et al. [6] found it difficult to modulate the frequency by synchronizing the operation of TA lasers powered by continuous radiation beams. Sanket [59] and Rohit [60] observed that the frequency of TA signals can only

be increased by reducing the tube length in a stack tube design. Chen et al. [6] investigated the coupling effect of a pair of TA lasers and further observed that the phase difference between a pair of TA lasers was not locked when the tube openings are far apart. When tube openings were close, the phase difference was "almost 180° out of phase at the focusing point." When "out-of-phase" thermo-acoustic waves are superimposed, the resulting amplitude is lower than the amplitude of the individual TA lasers. Because the frequency of TA lasers powered by pulsed radiation can be easily modulated, multiple TA lasers could potentially be constructed such that the resulting amplitude is higher than the individual amplitudes of the superimposed TA lasers. High-amplitude acoustic waves can subsequently be used for acoustic cleaning and carbon dioxide capture (explained in Section 2.3).

2.3 Research needs and motivations

Sections 2.1 and 2.2 review the applications of photo-acoustic and thermo-acoustic waves in material detection, refrigeration, and gas separation. However, on its own, acoustic energy can be utilized for a wide range of applications—most commonly in mining and materials processing as well as in the medical field, for cleaning and sterilizing surfaces and medical equipment [6]. Commercially available acoustic cleaners have applications in various other industries, including conventional power plants, as well as petrochemical, chemical and pharmaceutical plants [17]. They are also used in food processing, smelting, brewing and distilling, and manufacturing of products such as ceramics, detergent, cement and gypsum, carbon black, etc. [6]. Most commercially available acoustic cleaners have a range of 60 to 420 Hz, with a pressure

range of 480 to 620 kPa (70 to 90 psi) [17]. There are, however, some acoustic cleaners which operate in the infrasonic (below 40 Hz) and ultrasonic range (20–400 KHz). These acoustic cleaners provide a means to "prevent particulate build-up" and "material flow problems" [17], and their main functions include (but are not limited to) heat surfaces cleaners in boilers, electrostatic precipitators, super-heaters, ductwork, filters, cargo ship holds, spray dryers and rotary drum dryers, dry material bulk vehicles, ID fans, mixers and blenders, and other mechanical components [17].

The applications of acoustic waves often depend upon their amplitudes and frequencies. Low-frequency, high-amplitude acoustic waves can be used to remove dust from surfaces or to enhance particulate flows in conduits [61]. This type of acoustic waves can be applied in sonic soot blowers, and manufacturers such as Infrafone use this phenomenon to provide solutions to soot build-up in various thermal devices [61]. Using these sonic blowers prevents undesirable pressure drop and time delay in manual cleaning. High-frequency acoustic waves can be used in cleaning of soiled laundry and in food processing applications. They can also be used to sanitize or sterilize medical equipment or kitchenware [6].

Acoustic agglomeration is the physical phenomenon that allows applications such as acoustic cleaning and filtration of solid particles [62–65]. It was observed that when high amplitude acoustic waves are passed through aerosols, the suspended particles had a tendency to collide and form larger agglomerates [62]. In industrial applications, agglomeration has been used to remove small particulate matter using cyclone filters and electrostatic precipitators. The theory of acoustic agglomeration has

been covered extensively by several authors [62–64] and is beyond the scope of this thesis.

Acoustic waves have also shown promising use in carbon sequestration techniques. Several authors [18–23] have used acoustically assisted fluidized beds of activated carbon and zeolite to capture CO_2 from a $CO_25–N_2$ mixture. Activated carbon shows a much greater adsorption preference for CO_2 compared to other gases [66], and therefore it enables separation of CO_2 from a gas mixture. Acoustic signals were observed to enhance carbon dioxide adsorption in a fluidized bed of activated carbon [67]. Arena [67] and Raganati et al. [21] have shown an improvement of as much as 30% in CO_2 capture using acoustic signals from a loudspeaker. Applying acoustic signals also resulted in a decrease in fluidization velocity [52].

However, there are still major obstacles for sono-assisted CO_2 capture. Acoustic generation is expensive as well as energy intensive [19]. Moreover, beyond a threshold frequency of 120–130Hz, there is almost no enhancement in CO_2 capture in a fluidized bed.

Chen and Rahman [68] have designed a fluidized bed reactor to investigate carbon dioxide capture under both acoustic and thermo-acoustic conditions. Thermo-acoustic waves generated by solar radiation provide an inexpensive and fairly available means of obtaining acoustic energy. The proposed reactor design could potentially allow CO_2 capture over a wider range of frequencies. The proposed research also includes a comprehensive study of theoretical aspects of CO_2 adsorption behavior in solid-gas fluidized beds under acoustic and thermo-acoustic conditions, and it aims to develop a more comprehensive model that could explain experimental observations.

The purpose of this research is to generate thermo-acoustic waves at both low and high frequency ranges, such that they can be used in applications such as materials processing and acoustic cleaning [61]. Potential applications of this research would extend to the use of acoustic waves for the capture of carbon-dioxide in droplets and fluidized bed [68].

CHAPTER 3

MATHEMATICAL FORMULATION AND NUMERICAL SIMULATIONS

3.1 The Rosencwaig and Gersho (RG) model

Rosencwaig and Gersho [25] developed a mathematical model (often called the RG model) to analyze the temperature and pressure fluctuations that are generated when chopped radiation from a monochromatic radiation source is incident upon a sample solid inside a photo-acoustic cell. The RG model assumes that the primary cause of the acoustic signal is the periodic heat flow from solid to gas, and it ignores the possible effects of mechanical vibration of the solid and absorption of radiation by the gaseous medium. Figure 3.1 shows a schematic diagram of photo-acoustic cell, as presented by Rosencwaig and Gersho [25].

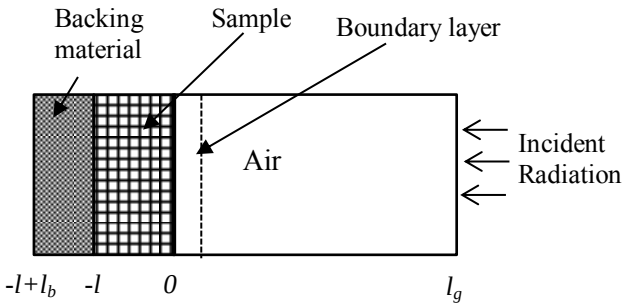

Figure 3.1: Schematic diagram of the photo-acoustic cell used in RG model. Adapted from [25].

The intensity (I) of the sinusoidal chopped radiation can be expressed as

$$I = 0.5I_0(1 + \cos \omega t) \tag{3.1}$$

Here, I_0 represents the incident radiation flux per unit area on the solid surface. If β is the absorptivity of the material at a given wavelength (λ), the intensity of IR radiation and the thermal diffusion equation for a given point within the solid can be expressed as

$$I = 0.5\beta\, I_0 \exp(\beta x)(1 + \cos\omega t) \tag{3.2}$$

$$\frac{d^2\Phi}{dx^2} = \frac{1}{\alpha_s}\frac{d\Phi}{dt} - A\exp(\beta x)[1 + \exp(j\omega t)] \tag{3.3}$$

$$A = \beta\, I_0\eta/2k_s \tag{3.4}$$

The equations (3.1)–(3.4) are applicable for x = [$-L_s$, 0]. Here, Φ (x, t) represents the solution for temperature, η is the efficiency with which the radiation is absorbed and k_s the thermal conductivity of the solid. α_s is the thermal diffusivity of the solid sample, and L_s the thickness of the solid sample. x = 0 is set at the interface of the solid and air column. For conduction through the air column [0, L_g]:

$$\frac{d^2\Phi}{dx^2} = \frac{1}{\alpha_g}\frac{d\Phi}{dt} \tag{3.5}$$

Here, L_g corresponds to the length of the air column, and α_g is the thermal diffusivity of air. The solution is complex-valued, and only the real part of the solution is of interest to this research. The actual temperature at a given position and time is expressed as

$$T(x,t) = Re[\Phi(x,t)] + T_{amb} \tag{3.6}$$

The spatially averaged temperature is given as

$$\Phi_{av} = (1/2\pi\mu_g)\int_0^{2\pi\mu g} \phi_{ac}(x,t)dx \tag{3.7}$$

ϕ_{ac} (x,t) is the sinusoidal component of the solution to Φ(x,t). The displacement of the gas piston due to periodic heating and the subsequent pressure fluctuations due to pulsed IR radiation can be obtained using the ideal adiabatic gas laws:

$$\delta x(t) = 2\pi\mu_g \frac{\phi_{av}}{T_0} \tag{3.8}$$

$$\delta P(t) = 2\pi\mu_g \frac{\gamma P_0}{g} \tag{3.9}$$

Rosencwaig and Gersho solved these equations analytically [25] to obtain an expression for the magnitude of sinusoidal pressure oscillations within the photo-acoustic cell. A complete mathematical derivation is beyond the scope of this thesis and can be found in other literature [25].

The RG model provides a useful mathematical platform for describing the thermo-acoustic effect due to pulsed incident radiation. However, the model does have a few limitations:

- The RG model was developed for a nonporous solid, and so it assumes that the heat transfer area between the sample material and the surrounding air is equal to the cross-sectional area of the sample solid. In this thesis, porous materials were used to absorb radiation, which means that the heat transfer area was much greater than the cross-sectional area of a nonporous solid of the same volume. Due to a much increased surface area for heat transfer, the volume of air contained within the hypothetical "gas-piston" was likely to be greater in volume, resulting in greater magnitude of acoustic amplitudes.
- According to the RG model, the only temperature changes in air occur within a small boundary layer of air near the heated sample. Rosencwaig and Gersho defined the boundary layer to be about 0.1 cm from the heated surface for a frequency of 100 Hz. The RG model uses the method of complex combinations to derive analytical solutions for the fluctuating or "ac" component of temperature, and it does not deal with the mean or "dc" component of temperature. In experiments presented in this thesis, it was observed that over a time interval much greater than the cyclic time-period of acoustic oscillations, the mean or "dc" temperature increased over time. COMSOL simulations (presented in Section 3.2) illustrate the increase of "dc" temperature and how it varied with time and axial location.
- The RG model assumes heat-flow in one-dimension only. Our experimental

observations showed that the diameters of TA converter opening, air column and chopper hole had a direct influence on the magnitude of acoustic waves. The RG model does not take into account the radial heat flow from the walls of the air columns, which facilitates cooling of air during the "chopped" half-cycles. In Section 5.6, it will be shown that externally heating the aluminum body of the TA converter (and thereby inhibiting the "cooling" process) significantly reduces the amplitude of acoustic waves.

- The RG model determines pressure inside the air column, assuming isentropic compression of an ideal gas and ignores pressure and temperature nonuniformities in the air column (except in the boundary layer). The length of the air column in the TA converter (in designs 2 and 3) is 3.2 cm. Taking the speed of sound as 343 m/s, the approximate time taken for the pressure wave to propagate through the air column can be calculated as $t_{pressurewave} = 0.032/343 = 8.8772 \times 10^{-5}$ s. For relatively low frequencies (less than 1kHz), this time interval is small compared to the time period of an acoustic cycle ($t_{pressurewave}$ is only 0.88% of acoustic time period for 100 Hz). In the kHz range, the time interval of a pressure wave to travel through the air column becomes more significant, compared to the time period of an acoustic cycle ($t_{pressurewave}$ is 8.8% of acoustic time period for 1 kHz). Therefore, air pressure within the air column cannot be considered uniform at higher frequencies.

3.2 2D numerical simulations of pressure oscillations inside the air column

Pressure and temperature distributions were obtained in a 2D axisymmetric geometry in COMSOL. With air inside the cylindrical domain, the geometry was assumed to be 3 cm long and 0.5 cm in diameter. The coordinates were assigned such that the center of the z-axis of the cylinder coincided with the origin of the coordinate system (i.e., r = 0, z = 0). The domain was periodically heated at surface 2, while surface 3 was insulated (Figure 3.2). The simulations were conducted for four cases. The initial and boundary conditions for case I are given as

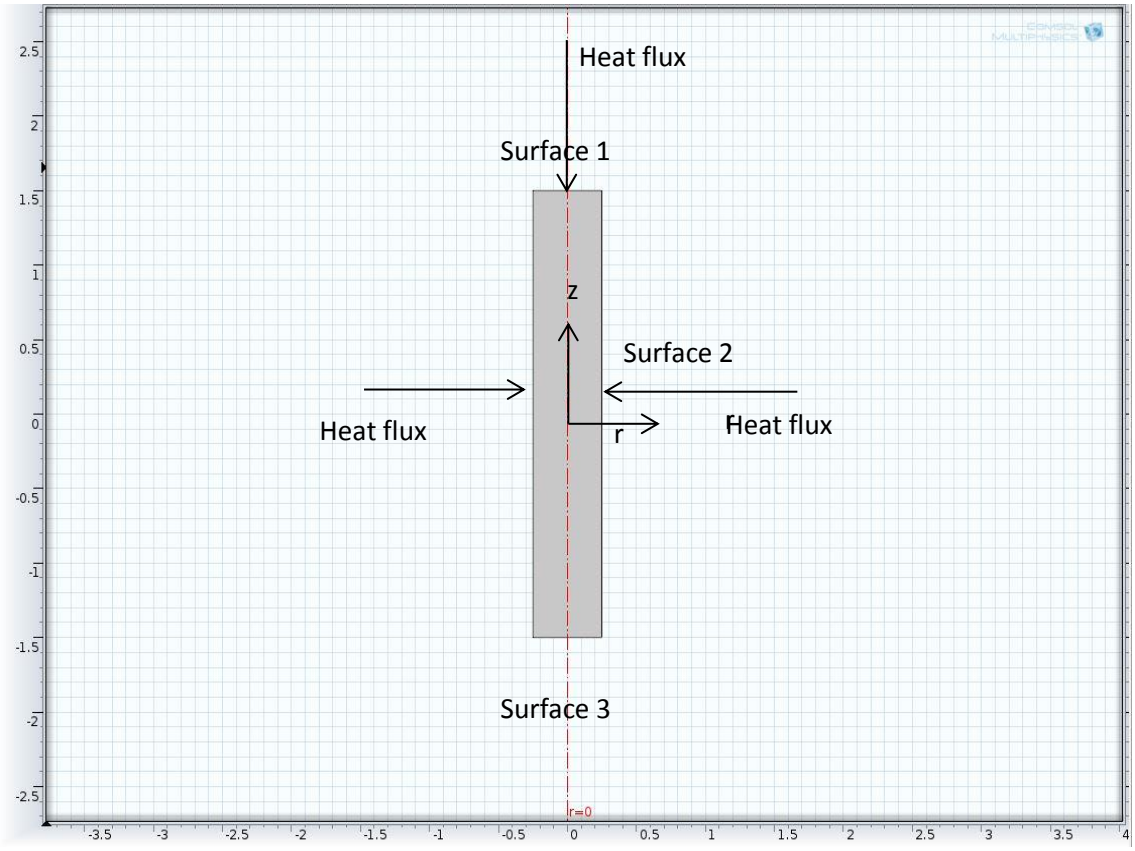

Figure 3.2: 2D axisymmetric domain for COMSOL simulation

$$q''(r, z = -0.015, t) = \beta(4.84 \times 10^4)(1 + \sin(2\pi ft)\ (W/m^2) \quad [\text{Surface 1}] \tag{3.10}$$

$$q''(r = 0.0025, z, t) = \beta(0.05)(4.84 \times 10^4)(1 + \sin(2\pi ft)\ (W/m^2) - h[T(r = 0.5, z, t) - T_\infty] - \varepsilon[T(r = 0.5, z, t)^4 - T_\infty{}^4] \quad [\text{Surface 2}] \tag{3.11}$$

$$q''(r, z = 0.015, t) = 0 \quad [\text{Surface 3}] \tag{3.12}$$

$$\text{Initial condition: } T(r, z, t = 0) = 293.15\ K \tag{3.13}$$

For case I, the periodic flux at surface 1 was approximately equal to 50% of the radiation flux absorbed by steel wool at 30% IR heater power level (with the remaining 50% accounting for heat loss to the surrounding). The periodic flux at surface 2 was assigned such that the radially inward flux had a magnitude of approximately 5% of the flux at surface 1. Because a low acoustic amplitude was obtained when there was no porous material inside the TA converter (as discussed in Chapter 5), the contribution of the radially inward flux was likely to be fairly small (later in this section, simulations assuming no radial flux are presented). It was also assumed that surface 2 lost energy by convection and radiation.

The following problem parameters were used for COMSOL simulation:

- Emissivity, $\varepsilon = 0.3$
- Absorptivity, $\beta = 0.3$
- $h = 20\ W/m^2\ K$
- $T\infty = 293.15\ K$

The emissivity and absorptivity values were selected considering that the total emissivity and absorptivity values and properties of steel wool (on which radiation was incident) are the same as those of low-carbon steel [69]. In the absence of bulk fluid motion inside the air column, a relatively low-value heat transfer coefficient (h) was selected. Simulation was performed for a chopping frequency, f = 100 Hz. The following simulation parameters were used for case I:

- Time step = 10^{-3} s
- Time domain = 1 s
- Scheme = Implicit

The following mesh parameters were used for this simulation:

- Maximum element size = 0.0113 cm
- Minimum element size = 5.0 x 10^{-4} cm
- Maximum element growth rate = 1.15
- Resolution of curvature = 0.3
- Resolution of narrow region = 1

Figure 3.3 shows the temperature distribution of the cylinder at t = 1 s. Figure 3.4 shows the temperature along the z-axis of the cylinder at various time intervals. Figure 3.5 presents temperature variations as a function of time at two "probe points." Two such probe points were defined: probe point 1 at (r = 0, z = 0.014) and probe point 2 at (r = 0, z = -0.01). The pressure within the domain is presented in Figure 3.6. Figures 3.3 and 3.04 show that the boundary layer was about 5 mm thick, and the time for the air column to reach "steady state" was about 1 s. Figure 3.5 shows that, at a

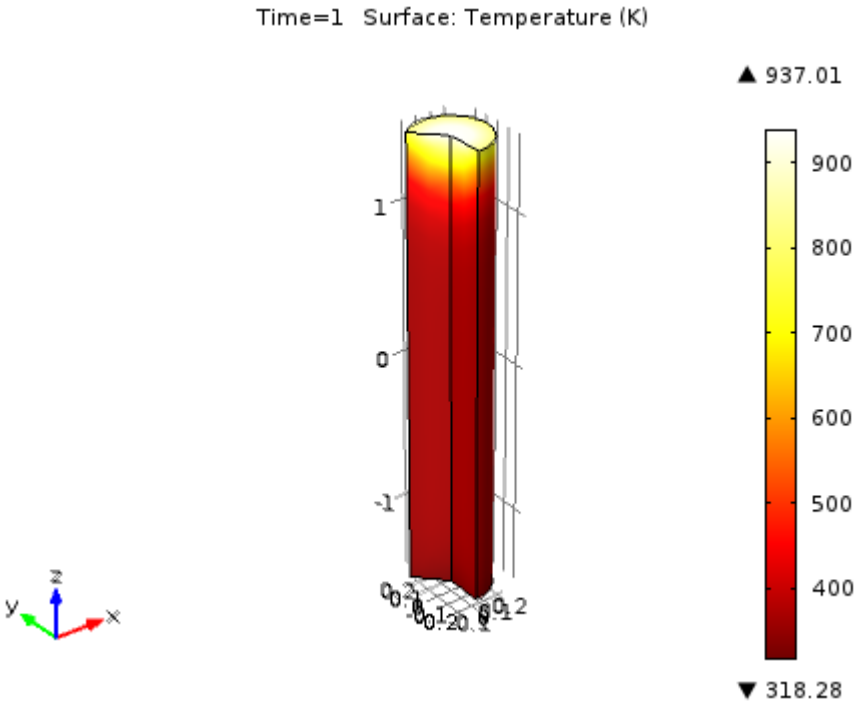

Figure 3.3: Temperature distribution for time = 1 s, frequency 100 Hz, with convective and radiative cooling and radial inflow from wall boundaries

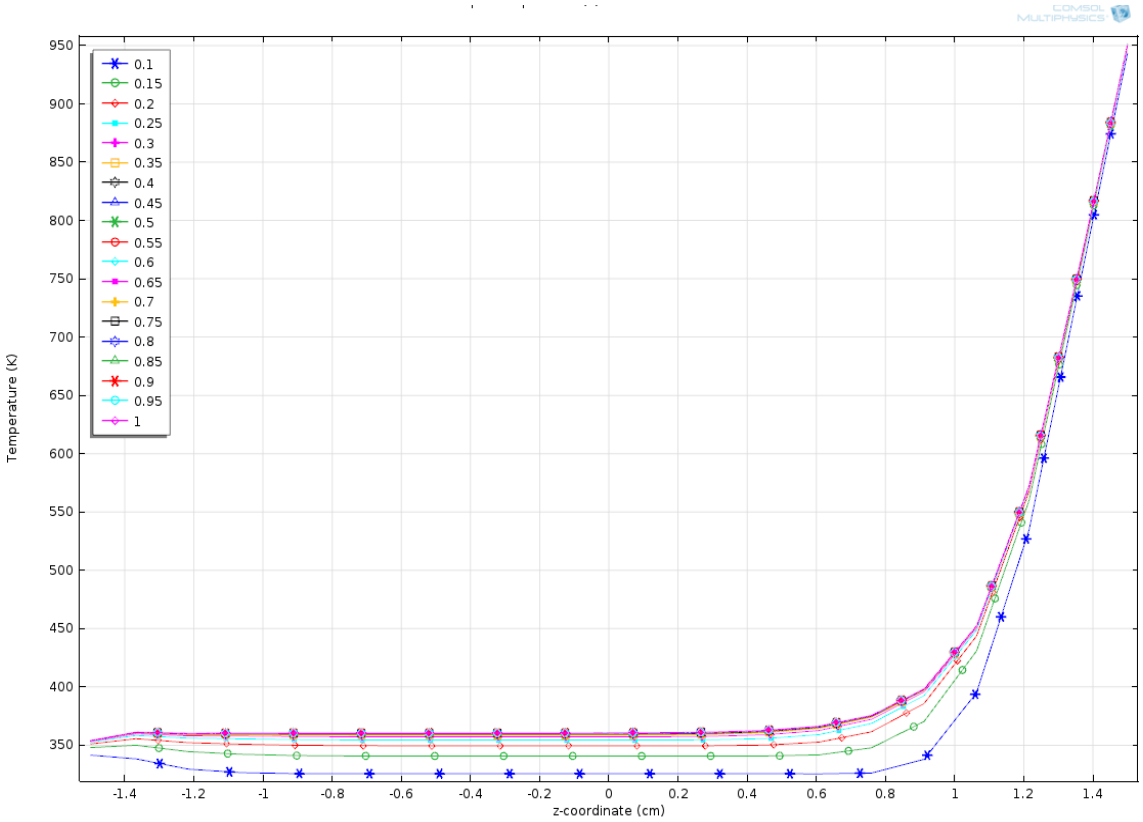

Figure 3.4: Temperature distribution along the axis of the cylinder at different time intervals

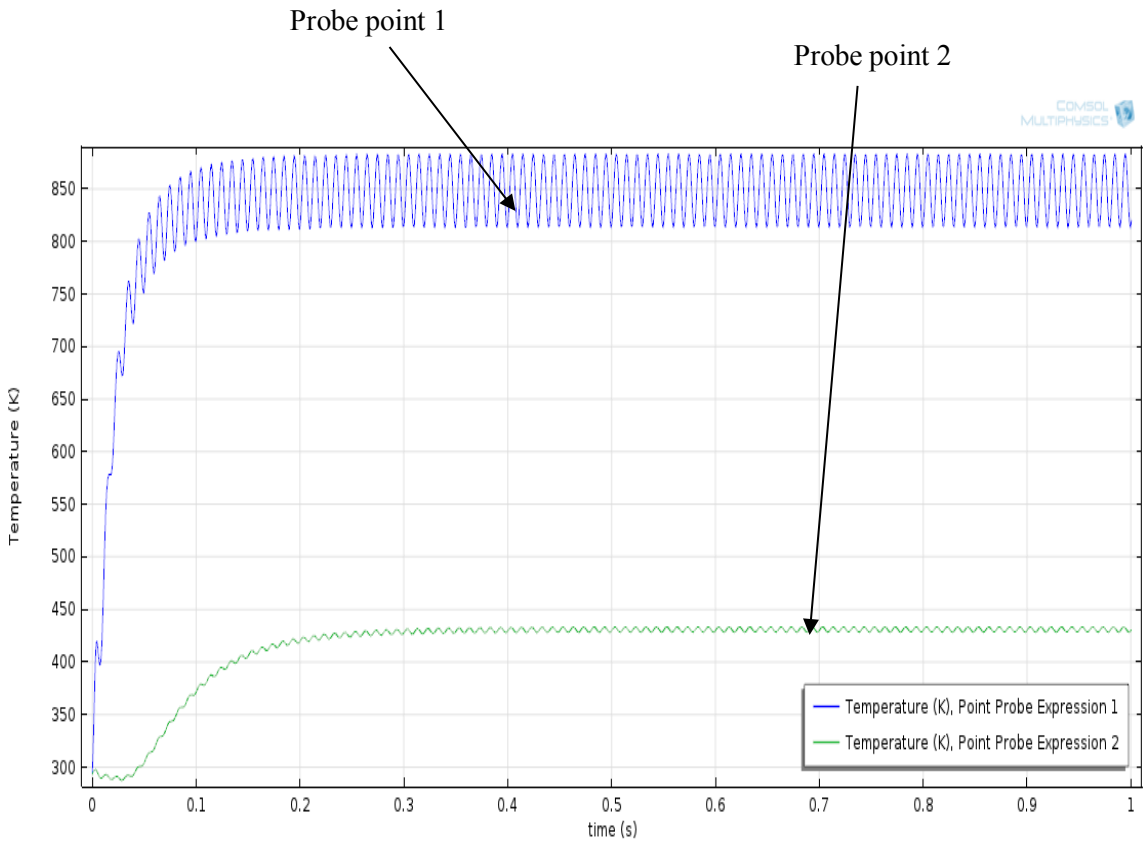

Figure 3.5: Time-dependent temperature profiles at probe 1 (r = 0, z = 0.014) and 2 (r = 0, z = -0.01)

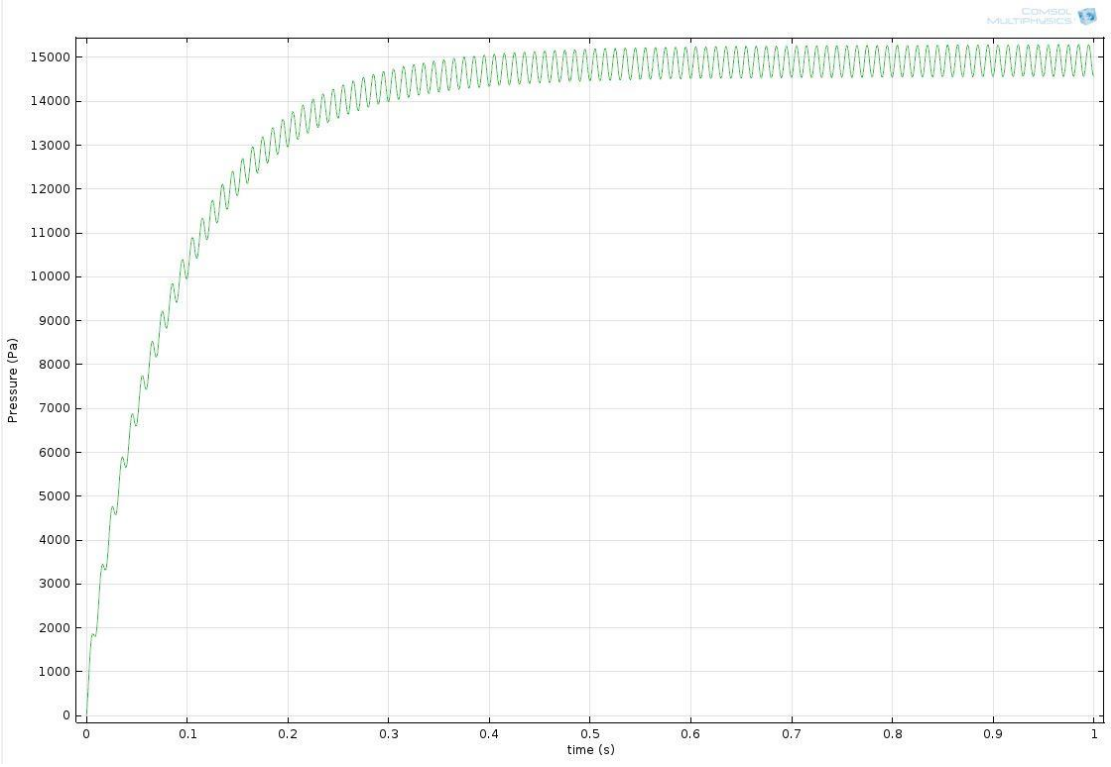

Figure 3.6: Time-dependent pressure within cylindrical domain at any z-location

distance of 2.5 cm from surface 1, the mean or "dc" temperature increased from 293 K to about 425 K in 1 s. As mentioned in Section 3.1, the RG model does not account for the mean or "dc" temperature because the complex combination method (as used in RG model) solves for "sustained solutions" only [25].

Figure 3.6 shows that at "steady state" pressure oscillations occurred with a peak to peak value of about 700 Pa (RMS of about 250 Pa), corresponding to a "steady state" peak-peak temperature fluctuation of about 60 K. The magnitude of pressure fluctuation was two orders of magnitude larger than the thermo-acoustic signals obtained in the experiments. (90 dB corresponds to about 1.125 Pa). This overestimation of pressure fluctuation from COMSOL could be due to the following factors:

- The boundary condition assumed that 50% of flux entering the TA converter was utilized to heat the air inside the air column. In our experiments, a lot of the energy was lost due to heat transfer from the heated steel wool to the surroundings. As a result, a very small percentage of incident radiation flux was available to heat the air inside the air column.
- The simulation in COMSOL assumed that surface 1 was a flat surface, when in our experiments, radiation was incident on a porous solid such as steel wool. As stated previously, the porosity of the solid increased the surface area for absorption of incident radiation and the contact area for heat transfer between the solid (i.e. steel wool filaments) and air. However, the friction between the oscillating air parcels and the porous medium was also unaccounted for in these COMSOL simulations.

Although temperature varied significantly in the axial direction, pressure was almost uniform within the air column (when f = 100 Hz), as seen in Figure 3.6. Temperature decreased with increasing axial distance from surface 1, as observed in Figures 3.4 and 3.5. Figure 3.5 shows that temperatures reached a "steady state" between 0.1 to 0.2 s (depending upon the axial location). (Here, "steady-state" indicates the time when the mean or "dc" temperature had reached almost reached a constant value). Figure 3.6 shows that the mean or "dc" pressure took about 0.4 seconds to reach a steady value.

Figure 3.4 shows temperature as a function of axial location at different time intervals. The temperatures were calculated at time intervals, which were exactly at the same point in their respective acoustic cycles (i.e., t = 0.1 s corresponds to completion

of exactly 10 acoustic cycles, t = 0.15 s corresponds to 15 cycles and so on). Therefore, the temperature values presented in Figure 3.4 were all "in phase" at the given time intervals. This means that the temperatures in Figure 3.4 can be considered changes in mean or "dc" temperatures over a period of 1 s. As temperature reached a steady "dc" value between 0.1 to 0.2 seconds within a distance of 0.1 cm of surface 1, there was very little "dc" temperature variation with time at that z-location after "steady state" had been reached. Surface 3 was assumed to be insulated, which is why at t = 0.1 s, there was a small rise in "dc" temperature near surface 3.The "steady state" pressure fluctuations in COMSOL simulations were much greater compared to acoustic signals obtained experimentally. A second COMSOL simulation (case II) was performed with reduced heat flux at surface 1 and surface 2.

$$q''(r, z = -0.015, t) = \beta(2.20 \times 10^3)(1 + \sin(2\pi ft)\ (W/m^2)\ \text{[Surface 1]} \qquad (3.14)$$

$$q''(r = 2.5 \times 10^{-4}, z, t) = \beta(0.05)(2.20 \times 10^3)(1 + \sin(2\pi ft)\ (W/m^2) - h[T(r = 0.5, z, t) - T_\infty] - \varepsilon[T(r = 0.5, z, t)^4 - T_\infty{}^4]\ \text{[Surface 2]} \qquad (3.15)$$

The time step was changed from 10^{-3} s to 10^{-4} s. All other parameters were the same as those in case I.

Figure 3.7 and 3.8 show the corresponding pressure and temperature plots for this simulation. The figures show that a peak-peak temperature fluctuation of 0.62 K at a location of (r = 0, z = 0.01) corresponding to a peak to peak pressure fluctuation of about 40 Pa (RMS amplitude of 14.1 Pa), which his was still significantly greater than

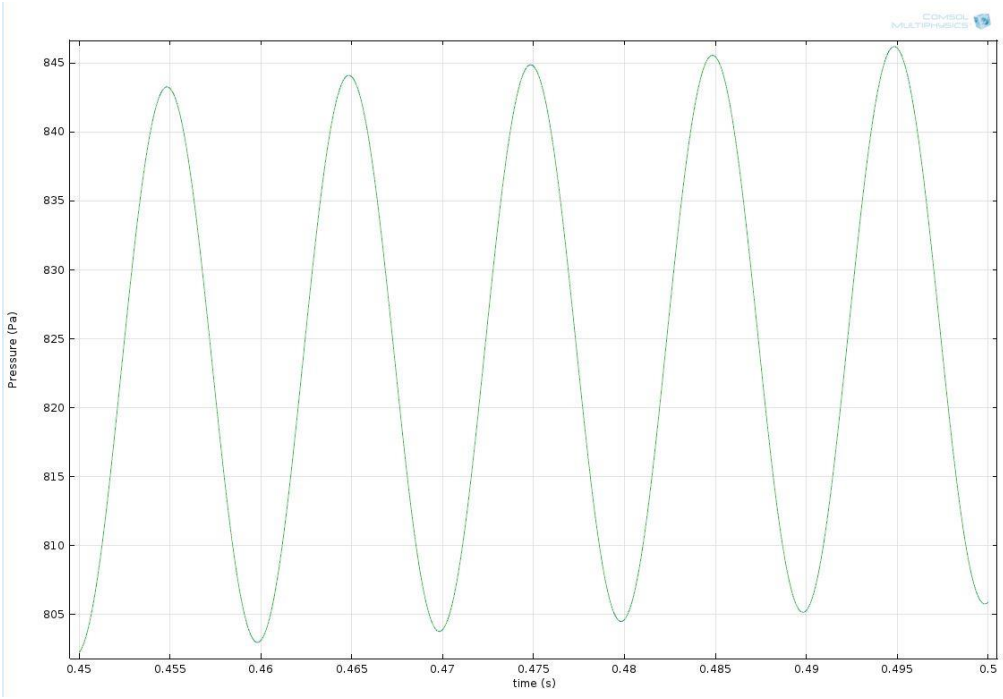

Figure 3.7: Fluctuating or "ac" pressure at steady state at any z-location (case II)

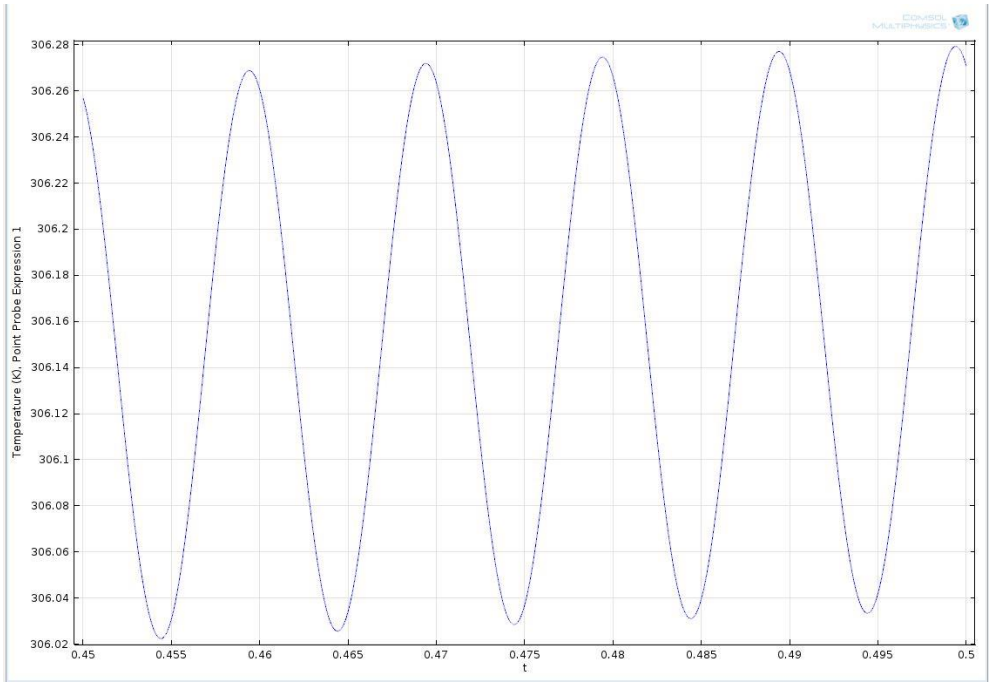

Figure 3.8: Fluctuating or "ac" temperature at steady state at (r = 0, z = 0.014) (case II)

the acoustic signals generated in experiments in this thesis. This proved that a very small fraction of thermal energy absorbed by the porous material was transferred to the air. As the conductivity of steel wool is much greater than air, most of the incident radiation energy was lost by conduction from the porous material to the aluminum body and then by convection and radiation to the surrounding. The pressure profile at location (r = 0, z = -0.01) is identical to that at location (r, z = 0.01), showing that at low frequencies, pressure is uniform in the domain. Thus, Figure 3.7 supports the conclusion made earlier—that the pressure is uniform in the air column and independent of z-location at low frequencies.

For case III, the incident heat flux on surface 1 was lowered to 880 W/m^2 (40% of the heat flux in case II), and the heat flux on surface 2 was completely removed (i.e., q''(r = 0.0025, z, t = 0). Figure 3.9 shows the corresponding pressure plot, indicating that with the reduced heat flux on surface 1 and zero heat flux on surface 2, the peak-peak amplitude was about 7 Pa, with an RMS of 1.87 Pa. This is of the same order of magnitude as experimentally obtained thermo-acoustic signals.

It is possible that the heat flux amplitudes used in case III underestimated the actual flux entering the TA converter. This possible discrepancy is due to the fact that the effect of "ac" pressure drop due to friction (explained earlier in this Section) was unaccounted for in my COMSOL simulations.

For the next simulation (case IV), the time step was reduced to 10^{-8} s, as a small time step would enable us to observe the propagation of a pressure wave in the air column.

Figure 3.10 shows the pressure as a function of axial location (z) for different

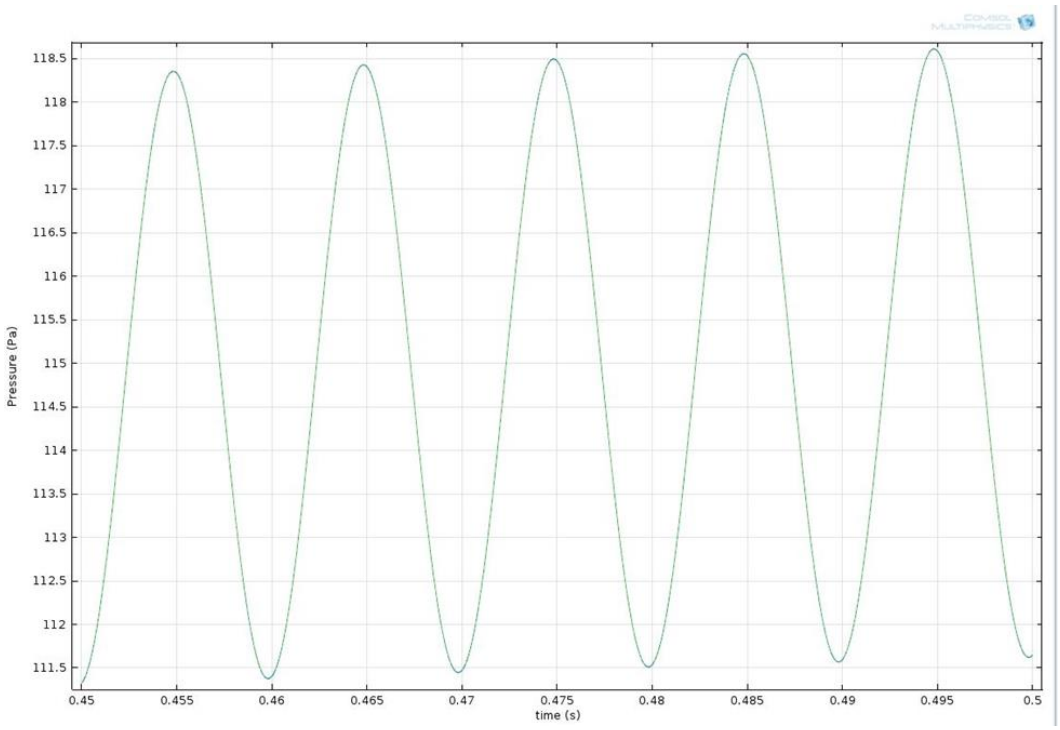

Figure 3.9: Fluctuating or "ac" temperature at steady state at (r = 0, z = 0.014) (case III)

time intervals. The plot shows that the pressure wave took about 10^{-4} s to travel through the length of the air column, which was close to the value of $t_{pressurewave}$ calculated in Section 3.1. The plot also shows that the "pressure gradient" became less steep and that the pressure started to become more "uniform" with increasing time. The boundary conditions for case IV were the same as those used in case III.

The simulation was performed for a chopping frequency of 1 kHz. The following computational parameters were used:

Mesh parameters:

Maximum element size = 0.007 cm

Minimum element size = 1.0e-4 cm

Maximum element growth rate = 1.13

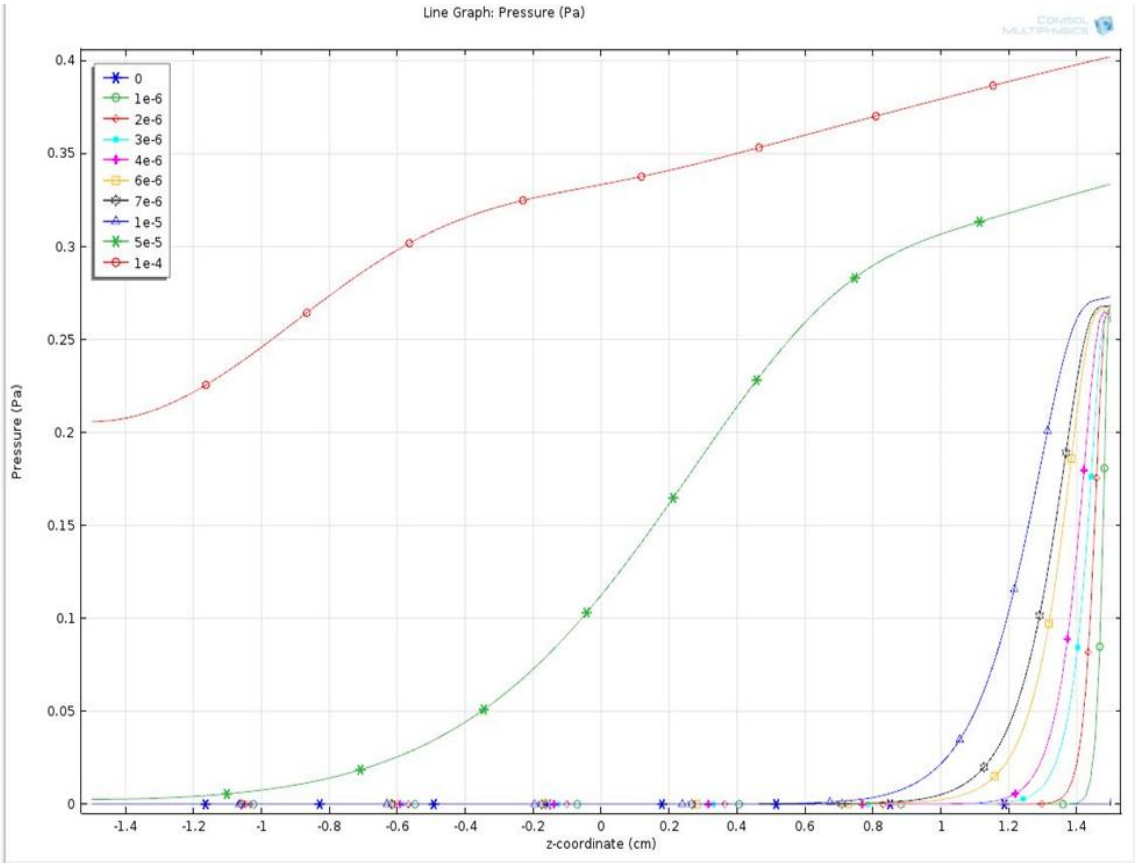

Figure 3.10: Pressure as a function of axial location at different time intervals (case IV)

Resolution of curvature = 0.3

3.3 Thermal relaxation time and thermal boundary layer

Thermal relaxation time (t_r) is a measure of thermal contact between the steel-wool filaments and the air in space between the filaments. It is an indicator of the time taken for the air between the filaments to be heated by the filaments and can be mathematically expressed as follows [70]:

$$t_r = r_c^2/2\alpha_g \tag{3.16}$$

Here, r_c is the characteristic length between two filaments (which will be defined shortly) and α_g is the thermal diffusivity of air. The characteristic length depends on the filament radius (r) and the average distance between the axes of two adjacent filaments (d). A rough estimate of the average filament spacing (d) can be determined from the packing density (ρ_{meas}) for a given grade of steel wool [70]:

$$V_{sw}/V_{meas} = A_{sw}/A_{fil+air} \tag{3.17}$$

Here, V_{sw} is the volume occupied only by the filaments (for a given volume of steel wool (V_{meas})) and A_{sw} is the cross sectional area of each filament. $A_{fil+air}$ is the total cross-sectional of the filament and the air surrounding the filament. For a given mass of steel wool contained within V_{meas}, equation (3.18) can be written as

$$\rho_{meas}/\rho_{sw} = r^2/r_{air}^2 \tag{3.18}$$

Here $r_{air} = d/2$ (Figure 3.11), ρ_{meas} is the packing density and ρ_{sw} is the material density of steel wool (which is assumed to be equal to the density of bulk low-carbon iron).

The packing density of grade 000 steel wool is approximately 400 kg/m^3 [71]. Most of the experiments in this thesis used steel wool of grade 0000. The "corrected" packing density for grade 0000 is given as

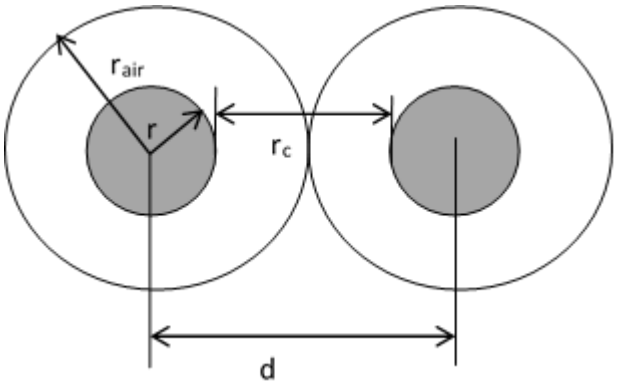

Figure 3.11: Schematic representation of d, r_c and r_{air}.

$$\rho_{meas,0000}/\rho_{meas,000} = r_{0000}^2/r_{000}^2 \quad (3.19)$$

Here, r_{0000} and r_{000} are the radii of steel wool filaments of grades 0000 and 000, respectively. Using r_{0000} = 12.5 μm and r_{000} = 17.5 μm [69], the packing density ($\rho_{meas,0000}$) for grade 0000 is equal to 784 kg/m^3. Using ρ_{sw} = 7850 kg/m^3 and r = r_{0000}, r_{air} was found to be equal to 39.5 μm. The characteristic length can then be determined as follows:

$$r_c = 2(r_{air} - r) \quad (3.20)$$

The calculated value for r_c is 54.10 μm, corresponding to an average filament spacing of 79 μm. The value for r_c is fairly close to that obtained by Rodriguez (r_c = 46.6 μm) [70]. Using equation (3.18), the thermal relaxation time (t_r) is calculated to be 7.7 x 10^{-5} s. When frequency f = 100 Hz, the thermal relaxation time is three orders of magnitude smaller than the time period of one acoustic cycle. The small value of t_r indicates good thermal contact between the filaments and the air surrounding the

filaments. For an angular frequency ω corresponding to f = 100 Hz, $\omega t_r << \pi$, indicating that the air between the filaments has been isothermally heated by the filaments during one acoustic cycle [70].

The RG model (Section 3.1) defines the thermal boundary layer as a hypothetical gas-layer near the periodically heated solid surface, which "responds thermally" to the temperature fluctuations on the solid surface [27]. According to the RG model, the fluctuations in temperature that are responsible for acoustic signals occur within this boundary layer only. The thickness of the boundary layer (δ) (as defined in the RG model) is given as

$$\delta = 2\pi/a_g \tag{3.21}$$

$$a_g = (\pi f/\alpha_g)^{1/2} \tag{3.22}$$

For f = 100 Hz, δ is approximately equal to 1.5 mm, which is significantly greater than the characteristic length. This ensures "more than 100% overlap" of r_c by δ.

For coarse grade steel wool (grade 3, filament radius = 90 μm), the corresponding estimates for d and t_r are 1.02 mm and 0.023 s, respectively. The thermal relaxation time for coarse steel wool (grade 3) is of the same order of magnitude as the time period of an acoustic cycle, indicating comparatively poor thermal contact between the heated filaments and the surrounding air. This is likely to result in a decrease of heat transfer between the filaments and air (compared to fine steel wool), resulting in decreased acoustic amplitudes. (These estimated results agree with the experimental

results in Chapter 5). For coarse steel wool (grade 3), ωt_r is slightly greater than π for f = 100 Hz, indicating that the heat transfer from the filament to air has "both adiabatic and isothermal characteristics" [70]. This means that while the air parcels within the boundary layer and close to the filament surface respond to changes in filament temperature, the air parcels further from the filament surface do not respond as effectively.

Brass has a thermal diffusivity of $\alpha = 1.8 \times 10^{-5}$ m^2/s and a material density of 8400 kg/m^3 similar to low-carbon iron and therefore, the thermal relaxation time and boundary layer thickness would be close to those for steel wool for a given filament radius and packing density. However, the absorptivity of brass wool is lower than that of steel wool [69], so when periodic radiation is incident on the brass-wool surface, the temperature fluctuations of the heated brass-wool filaments would be lower compared to those of steel wool filaments.

The absorptivity of metallic wools increases significantly when they are oxidized [69]. As a result, the temperature fluctuations within the boundary layer would be higher in case of oxidized metallic filaments, which would probably encourage higher acoustic amplitudes. Although the formation of an oxide layer would also increase the filament diameter, the corresponding decrease in thermal relaxation time is likely to be small. Consequently, oxidation of metallic wools due to incident radiation would probably increase the amplitude of acoustic waves.

CHAPTER 4

EXPERIMENTAL SETUP AND PROCEDURES

4.1 TA laser using IR heater as heat source

4.1.1 Construction of TA laser powered by IR radiation

The list of equipment used in the "indoor" experiments (using the IR heater as heat source) is given as follows:

- Research Inc Control IR heater Model 5420: The IR heater model 5420 used in this experiment is rated at 120 V, 750 W. It has a manual turn on-off switch and a manual potentiometer that regulates IR power level from 0 to 97% (a maximum IR power level of 65% is recommended by the manufacturer).
- Spot IR lamp model 4065: The lamp contains a tungsten filament with an inert gas added to increase longevity. The lamp is rated at 750 W, and the maximum temperature is limited to 350°C.
- IR heater cooling system: Compressed air was delivered to the IR heater to prevent overheating. The compressed air system was designed and built by Dr. NJ Kim (a visiting professor from Korea). The pressure range of the compressed air system is between 0 to 1030 kPa (0 to 150 psi).
- Electric motor with speed control (Type NSH-34RH): This is a 115 V (DC),

0.75 amp motor with a speed control (Motor: SL32, Minarik Electric Company). The speed of the motor is between 0 to 360 RPM. The motor shaft was connected to a chopper with 20 holes (2 cm in diameter).

- Microphone: Two microphones were used during the experiments conducted in this thesis:

  Microphone 1 (VideoSecu Spy Microphone): The microphone is 5 mm in diameter and has a preamplifier of 12 V that increases the output voltage from the microphone to a useable level. The microphone has a built-in filter to remove electronic noise and is highly sensitive; however, it reaches saturation at high amplitudes. Microphone 1 has a peak-peak saturation voltage of 12 V, which corresponds to an SPL of about 96 dB. When acoustic signals exceeded this peak-peak saturation, the time-dependent amplitude profiles showed "truncated peaks," indicating the microphone did not accurately measure amplitudes beyond this saturation value. When acoustic amplitudes higher than the saturation voltage were detected, a second microphone (microphone 2) had to be used.

  Microphone 2 (CE Mini Tie Clip Microphone Model 06A10): The microphone is 9 mm in diameter and its saturation level 2 is well above the working SPL range for this thesis.

  As discussed in Chapter 3, both microphones detected the fluctuating or "ac" component of pressure fluctuations, which were observed as acoustic signals. Any "steady" or "dc" increase in pressure was filtered by the microphones and was not observed in the time-domain amplitude data.

- TA Converters: Three TA-converter designs were used during the experiments (designs 1, 2, and 3). The purpose of using multiple designs of TA converters was to investigate the effect of different TA converter designs on acoustic amplitude. TA converters 2 and 3 are almost identical in design; the only difference is the dimension of the opening in TA converter cover (the opening diameter in TA converter 2 is 1.3 cm, compared to 1.6 cm in TA converter 3). The construction of TA converter 1 differs significantly from TA converters 2 and 3. The diameter of TA converter 1's air column is about 3.2 times the diameter of TA converter 2's air column, whereas the length of TA converter 1's column is higher by about 80% compared to the length of air column in TA converter 2. The other key difference in the arrangements of TA converters is that for TA converters 2 and 3, the silicon O-ring was not used. CAD diagrams showing the design of TA converters 2 and 3 are provided in Appendix B. Steel wool (grade 0000 and grade 3) (Figure 4.1) and brass wool (grade 0000) were used as porous materials. The TA converters were aligned with the axis of the IR lamp using a TA converter holder, which allowed for adjustments to the elevation of the TA converter (Figure 4.2).
- Data Acquisition Card: National instrument data acquisition card NI-DAQ 6009 was used to acquire data, which was then fed to LabVIEW Signal Express 2009 running on a computer with Windows XP OS. NI-DAQ 6009 has eight analog input ports at 12–14 bits and a maximum sampling rate of 48 KHz, two analog outputs (12 bit, max rate 150 KHz), twelve digital output and one 32-bit 5 MHz counter. LabVIEW Signal Express allows the user to set up and configure

Figure 4.1: Steel wool (grade 0000)

"steps" that allow the user to analyze the acquired data. The steps that were used in this analysis were

Acquire voltage (analog): This step takes data from DAQ and allows the user to adjust the sampling configurations. In this analysis, 5000 samples were collected at a rate of 20 KHz (over a time period of 0.25 s) for most experiments. For analysis of "transient" behavior of thermo-acoustic waves (explained in chapter 5), 48000 samples were collected at a rate of 5 kHz. The sampling rates were selected such that the Nyquist frequency criterion was met.

Amplitude and levels (Time-domain measurements): This step measures the RMS, peak to peak voltage for both raw and filtered data.

Distortion (Frequency-domain measurements): This step measures the frequency and total harmonic distortion of the data.

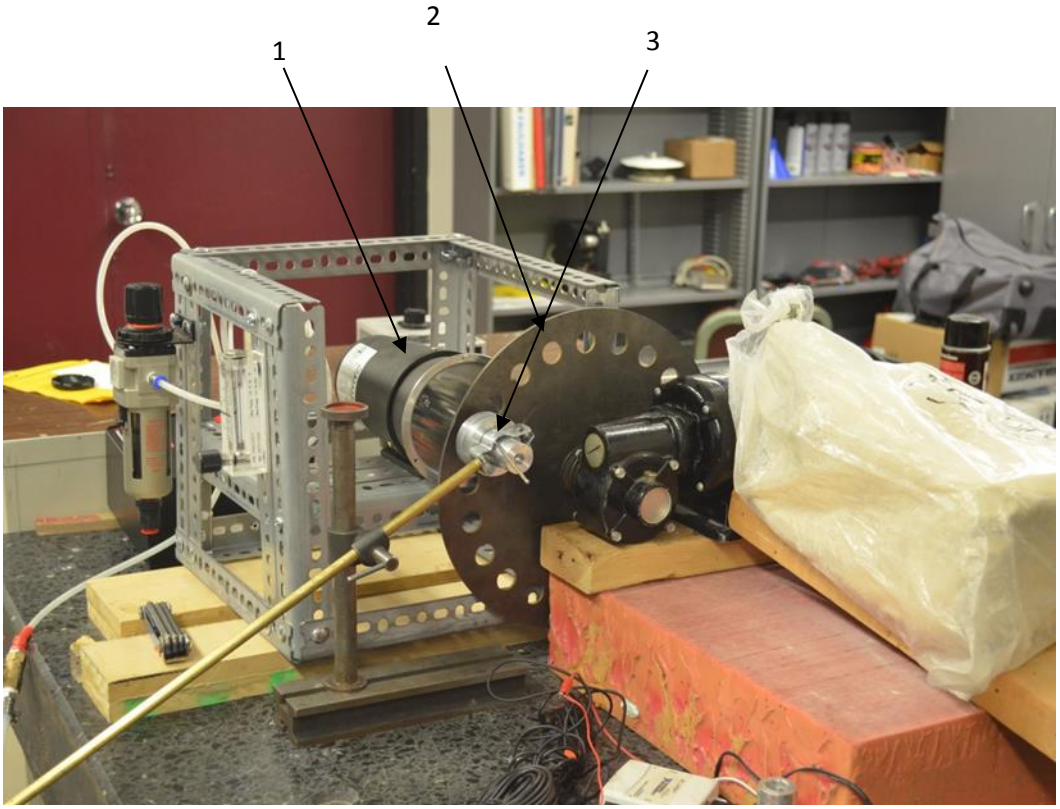

Figure 4.2: Experimental setup of prototype IR experiment. Microphone 1 or 2 is mounted at the back of the TA converter during experiments (not shown in this diagram). (1. IR heater 2. Chopper 3. TA converter without microphone).

4.1.2 Experimental procedures

Figure 4.2 shows the experimental setup of the "indoor" experiments. (Figure 4.3 shows a schematic representation of the experimental setup).

The operating procedures for the prototype IR experiment are given as follows:

1. A combination of porous material and TA converter was selected.
2. The TA converter cover was opened using a hex key and the porous material was inserted into the sample housing.
3. A suitable microphone was selected.

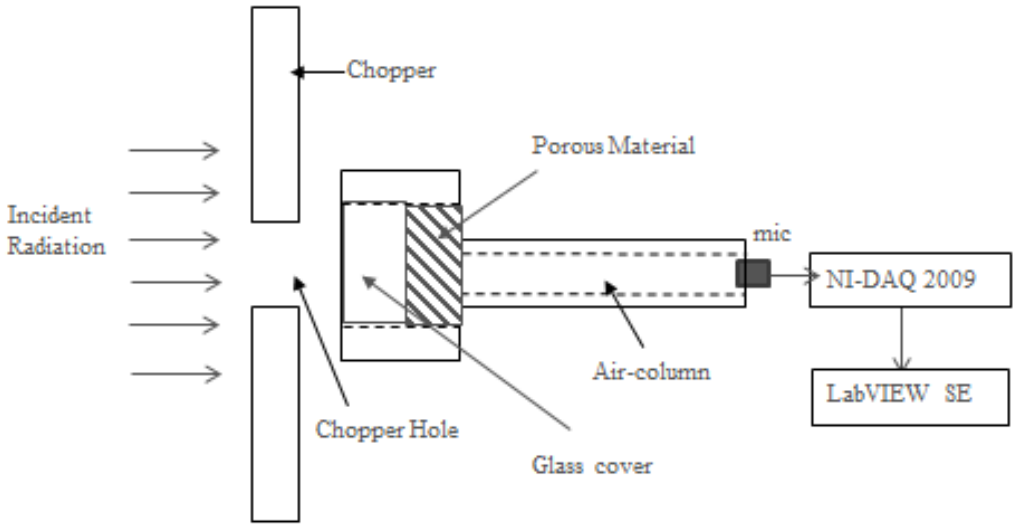

Figure 4.3: Schematic diagram of experimental setup

4. The location at which the microphonerophone wiring was to be glued to the TA converter was wrapped with electric tape.

5. A hot-glue gun was used to seal the microphone wiring to the TA converter such that the seal was air-tight.

6. The TA converter was secured inside the TA converter holder. The TA converter was placed at a distance of 1 cm from the chopper, such that the axes of the IR lamp and the TA converter opening were aligned. The screw in the TA converter stand was used to adjust the height of the TA converter.

7. The following steps were performed in LabVIEW Signal Express 2009:

(a) Open LabVIEW Signal Express 2009 > Project View > Add step > Acquire Signal > Analog > Voltage

(b) Add Step > Time Domain Measurements > Amplitude and Levels (RMS, +peak, -peak)

(c) Add Step > Frequency Domain Measurements > Distortion (frequency, THD)

(d) Click Run to start recording signals

8. The motor was switched on and the motor speed control was set to a desired motor speed. The cooling system was also turned on. The IR heater was set at a desired power level and then switched on.

9. After about 60 s, recording of acoustic signal was paused. Amplitude (in RMS), total harmonic distortion (THD), and frequency values were noted.

10. The time-domain amplitude data was exported to a spreadsheet application (Excel) and saved for later analysis.

11. A delay of 3–4 minutes was maintained before collecting the next set of data. This allowed the TA converter and the porous material to cool down so that each set of data would be independent and not affected by the previous set.

4.2 Solar to acoustic energy converter

4.2.1 Construction of solar-powered TA laser

The solar to acoustic energy converter uses solar radiation as heat source. The list of equipment used for the outdoor tests is given as follows:

- Chicago Electric Generator: The generator (model 67650) is rated at 3050 W. The engine runs on unleaded gasoline and supplies power to the motor.
- Dayton Electric Motor: The motor (model 2nKY4 model) is rated at 1.118 KW (1.5 HP) and has a maximum rotational speed of 3490 RPM, which is mounted on the solar cart as shown, and it is used to drive the chopper wheel.

- Power Inverter and Speed Control: Freenic-Mini power inverter (model FRN002) has a manual knob to control the rotational speed of the motor.
- Variac (Genral Radio Company): The Variac (type W5HM) is rated 240 V and can take load up to a load of 280 V. For the outdoor experiments, the load was kept constant at 220–230 V.
- Chopper Wheel: The chopper wheel (material: steel) has a diameter of 42 cm and has 60 holes (1 cm each) at a radius of 19 cm.
- Solar pyrometer: Apogee model SP-110 has silicon-cell sensor and gives the output in mV. The output in mV was converted to KW/m^2 by using the following equation:

$$\text{Radiation flux } (KW/m^2) = \text{Radiation flux (mV)} \times 5\ (KW/m^2)/mV \qquad (4.1)$$

- Solar flux alignment surface: The solar pyrometer was screwed to an inclined wooden surface, which allowed restricted motion in two directions (Figure 4.4). The axis of the flux meter was carefully aligned with the axis of the alignment nail.
- TA converter: The TA converter was mounted on the movable part of the cart and placed behind the chopper hole.
- Microphone: Both microphones 1 and 2 (as described in Section 4.2.1) were used for the outdoor tests.
- Lens: A plastic Frensel lens with diameter of 73 cm (28.5 inches) and focal length of 89 cm (35 inches) was mounted on the cart.

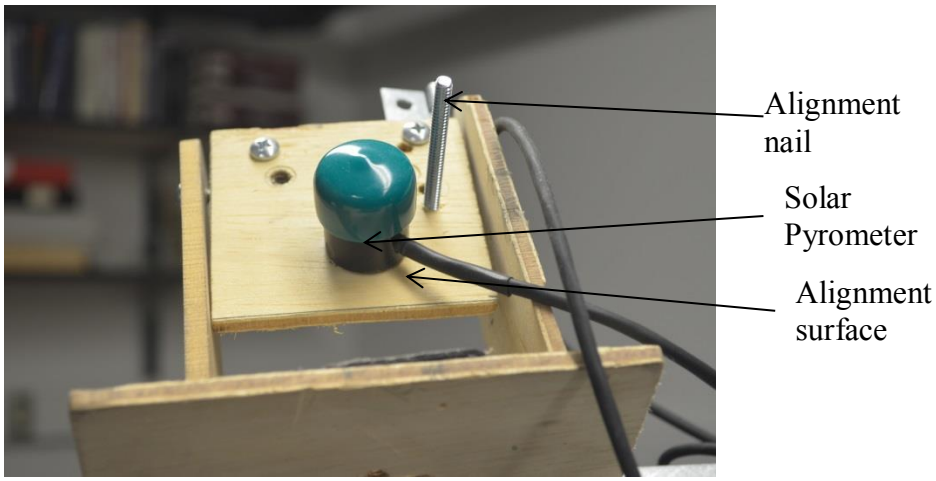

Figure 4.4: Solar pyrometer with alignment surface

- Cart: This is the experimental rig that contains the TA converter (with holder), chopper wheel, solar pyrometer (with alignment surface), and the lens. The TA converter, chopper wheel, and the lens were mounted on the same "inclined plane." This plane was inclined manually and aimed at the sun, so as to maximize the flux entering the TA converter (Figure 4.5).

4.2.2 Experimental procedures

The operating procedures for the "outdoor" experiment are given as follows:

1. All equipments were taken outdoors.
2. The transformer and the multiplug were connected to the generator.

   (a) The microphone power and laptop charger were connected to the multiplug.

   (b) The microphone cords were connected to the microphone.

   (c) The microphone amplifier was connected to the multiplug and the microphone.

Figure 4.5: Cart used for solar to acoustic energy converter

(d) The data acquisition card (NI-DAQ 2009) was connected to a computer through a USB port.

3. The generator was turned on.
   (a) The fuel switch was set to on.
   (b) The throttle was set to "Cold Choke."
   (c) The generator was started using the manual starter "pull."
   (d) The throttle was set to "Warm Start."
4. The transformer knob was set to 220V.
5. The red and black ports were connected from the solar flux meter to data acquisition card.
6. LabVIEW Signal Express 2009 was opened to log the time-domain amplitude data.
7. The solar alignment surface and lens-chopper-TA converter were aligned to the sun. (This step is explained in greater detail in Section 4.2.3).
8. TA converter was placed at an optimum distance (~2 cm) from the chopper hole.
9. The motor speed was set using the knob in the motor controls, and the motor controls were set to "RUN."
10. The time-domain data were exported to a spreadsheet application (Excel). These data were later imported to MATLAB for postprocessing (i.e., determining RMS, obtaining FFT plot and applying filter).
11. When the experiment was completed, the chopper speed was reduced and the generator was turned off. All the generator switches were turned off (fuel switch was set to "OFF" and generator main switch was turned off.)

4.2.3 Alignment of pyrometer and lens-chopper-TA converter module

To ensure that the radiation flux recorded by the solar pyrometer was the same as the radiation flux incident on the lens, it was important to align the solar pyrometer, alignment nail, and lens-chopper-TA converter module. To start with, it was ensured that the alignment nail and the solar pyrometer were both perpendicular to the alignment surface. The nail was aligned to the sun such that nail shadow was minimum on the alignment surface. The solar pyrometer was aligned parallel to the axis of the nail, such that when it was rotated away from its "alignment position," the pyrometer reading dropped from its maximum value.

Next, the lens-chopper-TA converter module was then adjusted by manually inclining the module until sharpest solar focus was observed on the chopper disc. At that instant, the alignment surface was adjusted so that the nail shadow was minimum on the alignment surface. Thus, it was ensured that maximum radiation incident on the chopper disc was simultaneous with the point of minimum nail shadow on the alignment surface when the solar pyrometer reading was taken.

4.3 Conversion of microphone outputs to decibels

The outputs from microphones (as obtained in LABVIEW) were measured in the voltage scale. Therefore, to convert acoustic amplitudes to decibels, it was necessary to obtain reference calibration plots.

To generate sound waves of known frequency and amplitude, a "tone generator software" along with a speaker system (Logitech speaker system Z313) was used. The output from the tone generator was a sine wave (TA waves in our experiments closely

resembled sinusoidal waves), which was connected to a set of two speakers. The microphone was placed at a distance of 7.6 cm from each speaker, such that each speaker was about 30° from the microphone axis (Figure 4.6). (The number of speakers and angle between the speakers were arbitrarily chosen). The sound output from the speakers was varied using the "volume knob" in the tone generator software, and the corresponding voltage readings were obtained in LabVIEW Signal Express 2009. The sound level (in dBA) for each output was then measured using a sound level meter kept at the same distance (7.6 cm) from the speakers. The sound meter used was a Tenma 72-942 meter, which conforms to IEC651 type 2, ANSI S1.4 type 2 for sound level meters [59]. For readings using the sound-level meter, a "Fast response, A-Weighting, Hi-level" configuration was used. Calibration plots (dBA vs voltage reading) obtained at frequencies of 100 Hz, 200 Hz, 400 Hz, 600 Hz, 1 kHz, 2 kHz, and 3 kHz are presented in Appendix A.

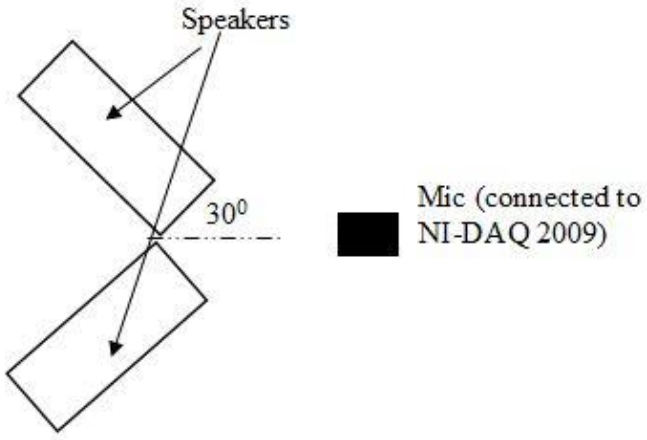

Figure 4.6: Schematic diagram of experimental setup for calibration tests

The outputs in all of the calibration tests were obtained in dBA (dB with A-weighting). To convert from dBA to the "universal" decibel scale (dB) at a given frequency, a correction factor (CF) had to be added. This correction factor was obtained from the A-weighting curve (Appendix A) [72].

A sample calculation to convert from microphone voltage to dB is given as follows:

- For 200 Hz, a voltage of 1 V obtained using microphone 1 corresponds to 74.13 dBA (Figure A.3).
- CF for 200 Hz = 8 dB (as obtained from A-weighting curve in Figure A.10)
- Reading in dB = Reading in dBA + CF = 74.13 + 8 = 82.13 dB
- So, a voltage of 1 V using microphone 1 at 200 Hz corresponds to 82.13 dB.

CHAPTER 5

RESULTS AND DISCUSSIONS

5.1 Analysis of acoustic signal obtained

The acoustic signal detected by the microphone was subsequently analyzed using LabVIEW Signal Express 2009. Figure 5.1 shows the time-domain data for a sample signal obtained at an acoustic frequency of 127.5 Hz (as detected by the microphone).

FFT analysis for the signal in Figure 5.1 was performed in MATLAB with a frequency range of 0–130 Hz and a sampling rate of 1000 samples/second. The

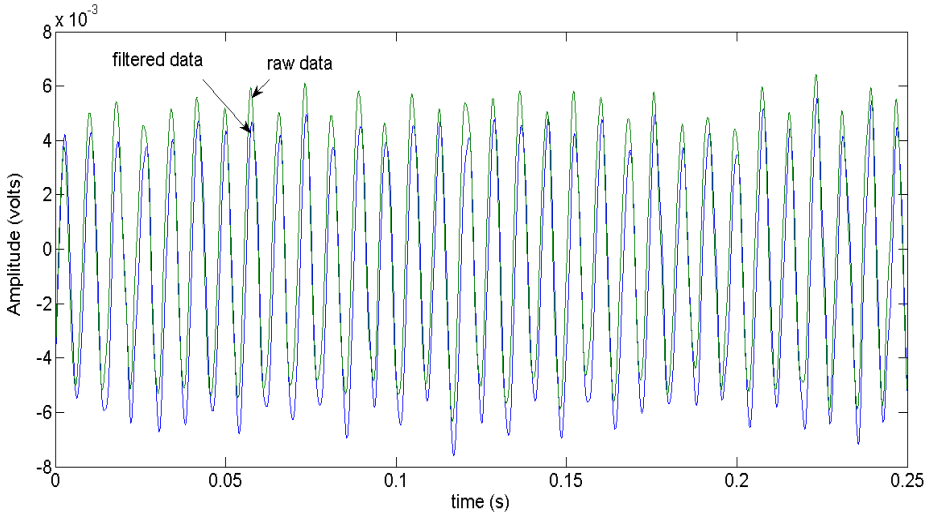

Figure 5.1: Acoustic signal (unfiltered and filtered) obtained at 127.5 Hz. Configurations: TA converter 2, fine steel wool (grade 0000), length of steel wool = 0.8 cm, microphone 2, IR power level at 65%.

corresponding plot (Figure 5.2) shows a prominent peak at 127.5 Hz. The rotational speed of the motor for the acoustic signal in Figure 5.1 was 360 RPM, measured using a tachometer, which corresponded to a chopping frequency of 126Hz (6 RPS x 21 holes). The chopping frequency (i.e., the frequency at which the incident radiation was interrupted by the chopper) was close to the acoustic frequency of 127.5 Hz (about 1% error taking 127.5 Hz as the base value), so the acoustic frequency, as detected by the microphone, can be considered equal to the chopping frequency. This is because the number of interceptions of incident radiation corresponds to the frequency of heat transfer between the porous material and the surrounding air and thereby, it also corresponds to the frequency of the periodic expansion of air inside the air column.

The small difference between the chopping frequency and the acoustic frequency could have been due to the uncertainties in readings for the acoustic frequency and the rotational speed. The figure also shows a short peak at around 60 Hz, which represents the inherent electronic noise that was present even when the IR heater was turned off.

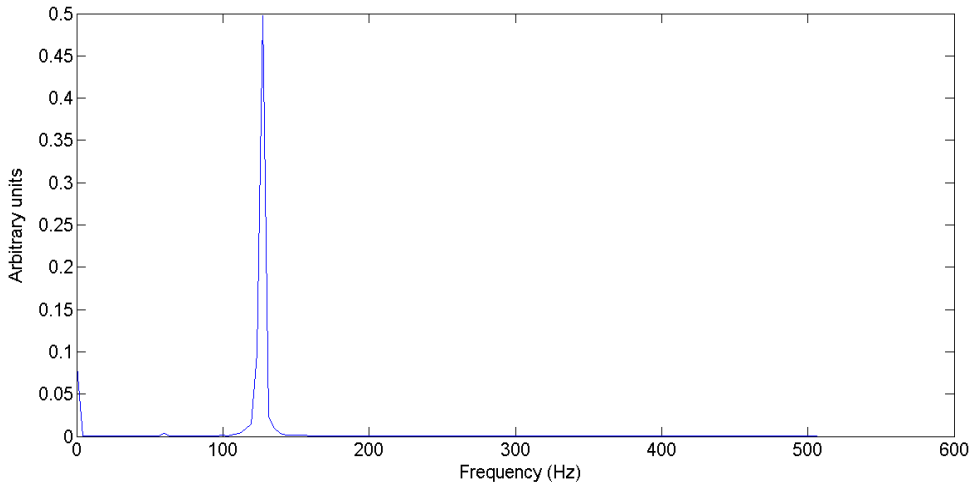

Figure 5.2: Analysis of unfiltered acoustic signal in Figure 5.1. Sampling rate: 1000 samples/second. Number of samples for FFT analysis: 256.

The effect of the superposition of 60 Hz noise was removed using a second-order, high-pass Butterworth filter (details of filter type will be elaborated in Section 5.5.1). By increasing the sampling rate and number of samples for the FFT analysis, it was observed that relatively smaller peaks were present at frequencies higher than 130 Hz (Figure 5.3). These were harmonics that were present due to the fact that the acoustic signal was not a perfect sine/cosine wave, although the deviation of the acoustic signal from a sinusoidal signal was small.

The time-dependent profile of temperature inside the air column had a fluctuating (or "ac") component and a mean (or "dc") component. As explained in Chapter 3, the time-dependent air temperature profile at a given axial location at "steady state" was found to be periodic with respect to the mean air temperature. Differences between the "steady-state" and "transient state," as applicable to this thesis, will be elaborated in Section 5.4.4. The fluctuating or "ac" component of temperature was responsible for the generation of thermo-acoustic signals, which, in our experiments, were periodic but not

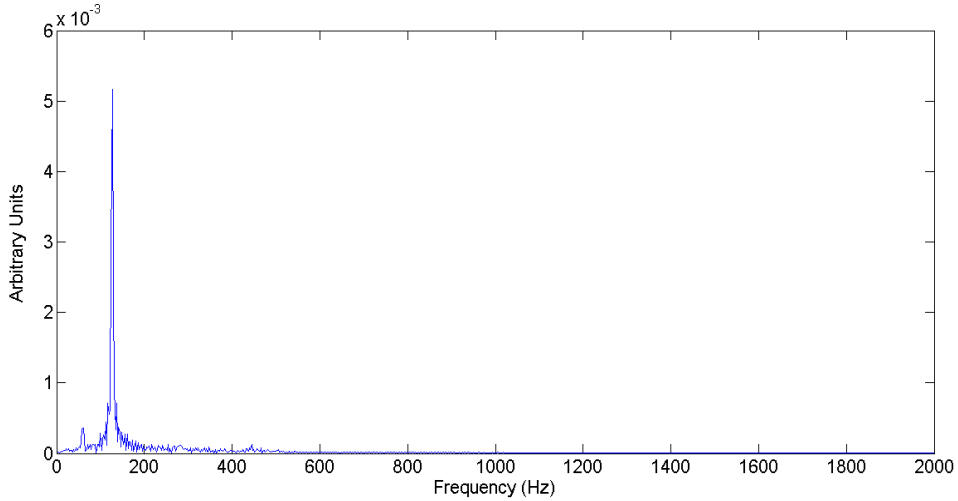

Figure 5.3: FFT analysis for raw acoustic signal in Figure 5.1. Sampling rate: 20,000 samples/second, number of samples for FFT analysis: 2^{32}

perfectly sinusoidal. The deviation of these signals from a perfectly sinusoidal profile could have been due to the nature of the pulsed radiation flux entering the TA converter (as explored in Section 5.2) and changes in relevant thermal properties, such as the absorptivity and emissivity of steel-wool filament and the convective heat transfer coefficient, with temperature.

5.2 Thermal radiation entering the TA converter

Section 5.1 discusses the observation that the acoustic signals obtained were not perfect sinusoidal functions. One of the factors that influenced the nature of the time-dependent acoustic amplitude profile was the rate of radiation energy entering the TA converter.

Figure 5.4 shows a schematic diagram to investigate the overlapped area between the chopper hole and TA converter opening, which dictates the rate of radiation energy entering the TA converter opening. Let circles 1 and 2 represent the TA converter opening and chopper hole, respectively. Circle 1 is stationary with center O_1, whereas circle 2 with center O_2 moves with a chopping frequency f (i.e., the frequency of interceptions of the radiation beam by chopper hole) at a radius R from the center of the chopper wheel C. At t = 0, O_1 is aligned with O_2. The following nomenclature is used for the mathematical analysis of radiation energy entering the TA converter:

Radius of circle 1 = $O_1A = r_1$

Radius of circle 2 = $O_2A = r_2$

Distance between the centers O_1 and O_2 = L

The nomenclature for the angles is: angle $AO_1O_2 = \theta_1$, angle $AO_2O_1 = \alpha_1$, angle AO_1B

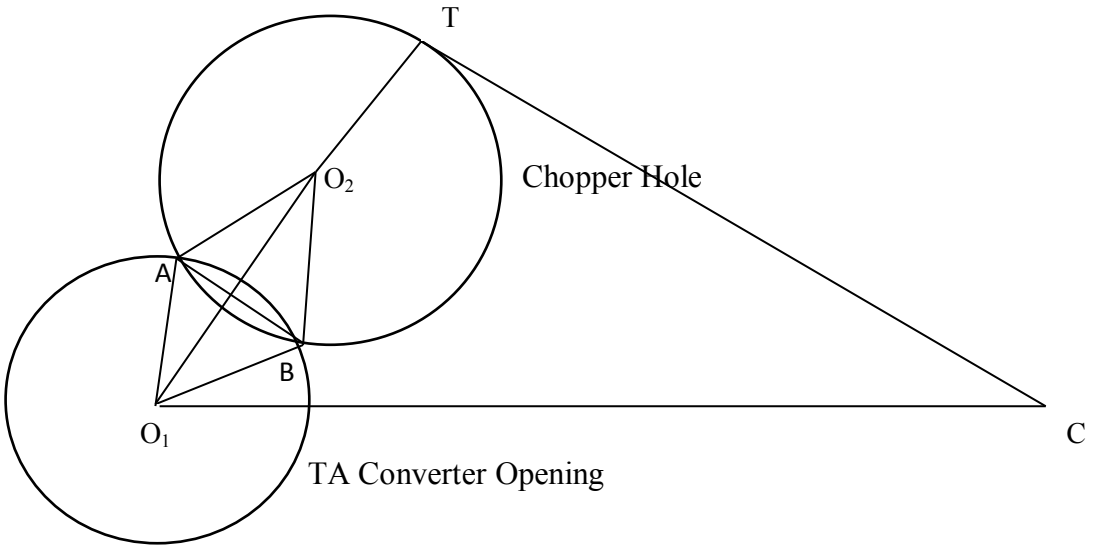

Figure 5.4: Schematic diagram showing relative positions of TA converter opening and chopper hole.

= θ , angle $AO_2B = \alpha$, $O_1CT = \Phi$.

For "indoor" experiments using the IR heater as heat source, the radius of chopper hole (r_2) and the distance between the chopper hole and center of the chopper (L) are 1 cm and 22 cm, respectively. Radius of circle 1 (r_1) is taken as the radius of the TA converter opening (0.8 cm). At time t = 0, the centers of circles O_1 and O_2 are aligned. At a time $t = \tau$, the angle Φ can be expressed as

$$\Phi = (\tau/T)*(0.299) \text{ radians for } \tau < T/2 \quad (5.1)$$

$$\Phi = 0.299 - (\tau/T)*(0.299) \text{ radians for } T/2 < \tau < T \quad (5.2)$$

Here, T is the period of the radiation flux cycle and 0.299 radians (2π radians/21 holes) is the angle covered by Φ during the entire time period T. The distance between the centers

O_1 and O_2 at any given time is

$$O_1O_2 = L = R\sin\Phi - r_2 \tag{5.3}$$

Angle θ_1 and α_1 can be calculated using the cosine rule. By observing symmetry, it can be deduced that $\theta = 2\theta_1$ and $\alpha = 2\alpha_1$.

For $r_2 - r_1 < x < r_2 + r_1$:

Overlapped area between two circles, $A = 0.5(r_1^2)(\theta - \sin\theta) + 0.5(r_2^2)(\alpha - \sin\alpha)$ (5.4)

For $x < r_2 - r_1$:

$$A = \pi r_1^2 \tag{5.5}$$

It should be noted that this expression for the overlapped area (A) only holds true when $L < (r_1 + r_2)$. When L exceeds $(r_1 + r_2)$, $A = 0$ and no radiation enters the TA laser. Energy from thermal radiation absorbed by the TA converter is proportional to the overlapped area at any given time. Figure 5.5 shows a plot of overlapped area (normalized by the area of the TA converter opening) versus time for a complete cycle.

However, there are two other factors besides the overlapped area that could possibly influence the profile of radiation flux entering the TA converter:

- It was assumed so far that all of the radiation contributing to thermo-acoustic generation enters the TA converter only through the TA converter opening. In

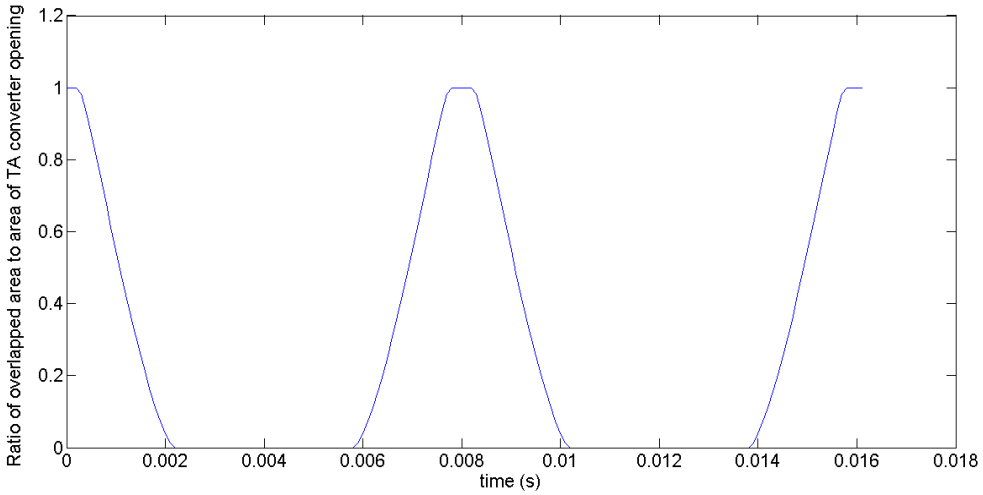

Figure 5.5: Time-dependent profile of overlapped area at an acoustic frequency of 125 Hz

reality, part of the incident radiation was absorbed by the aluminum body of the TA converter, due to the divergence of the radiation beam.

- The radiation flux was not uniform as assumed, but varied in the radial direction. Figure 5.6 shows the radial flux distribution, as specified by the IR heater manufacturer. For TA converter 2 (TA converter opening diameter 1.3 cm), the reduction in flux from the center to the circumference of the opening is about 25% (for the IR heater with a circular cut shield configuration), whereas for the TA converters 1 and 3 (TA converter opening diameter = 1.6 cm), the difference is as much as about 50%. This radial variation in radiation flux could be the reason as to why there were no “squared-peaks” (Figure 5.5) in the measured acoustic signal (Figure 5.1).

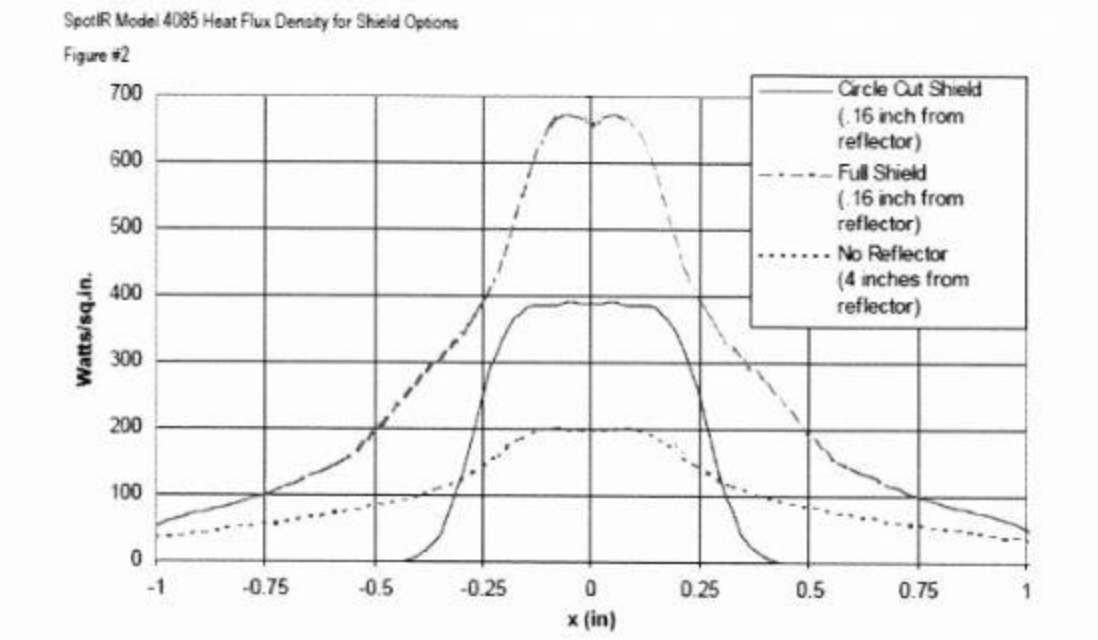

Figure 5.6: Radiation distribution in the radial direction (as specified by SpotIR) [73]

5.3 Absence of acoustic waves when the air column was open to ambient air

The plot in Figure 5.7 shows the signal obtained when the air column was open to ambient air. This was done by drilling a hole in the cylindrical body of TA converter 1, meaning that the air column was open to the ambient. The plot shows that there was no acoustic signal obtained when the air column in the TA converter was open to ambient air. This showed that acoustic waves were generated only within a confined air column.

5.4 Factors affecting amplitude of thermo-acoustic waves

5.4.1 Chopping frequency

Increasing the chopping frequency was found to have an adverse effect on the amplitude of acoustic waves, as observed in Figure 5.8. Increasing the chopper speed

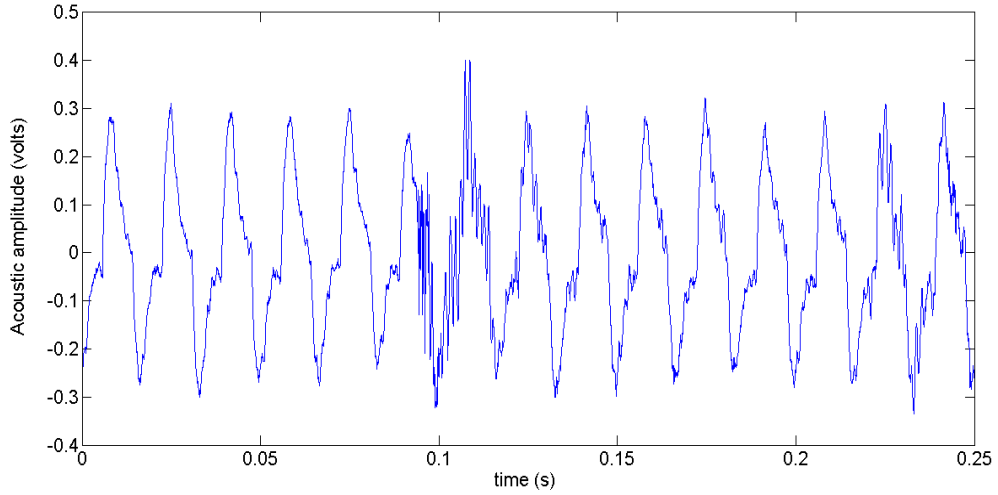

Figure 5.7: Absence of thermo-acoustic signals when air column is open to ambient. Configurations: TA converter 3, fine-steel wool (grade 0000), length of steel wool = 0.8 cm, microphone 1.

decreased the exposure time for which the porous material was exposed to IR radiation. This meant that the radiation energy absorbed per cycle would be lower, resulting in a decrease in the temperature of the heated steel-wool filaments. Due to a decrease in temperature difference between the steel-wool filaments and the temperature of the air surrounding the heated steel-wool filaments, the amplitude of acoustic waves would decrease. For this experiment IR power was kept at 30%. (100% IR power level corresponds to about 400 W/in^2 or 6.2 x 10^5 W/m^2 at the focusing point, as shown in Figure 5.6).

The other factor that could have encouraged an increase in acoustic amplitudes with decreasing frequency was that during the "chopped" half-cycle, the time for cooling the heated steel wool was longer.

Total harmonic distortion (THD) is a parameter that indicates the extent to

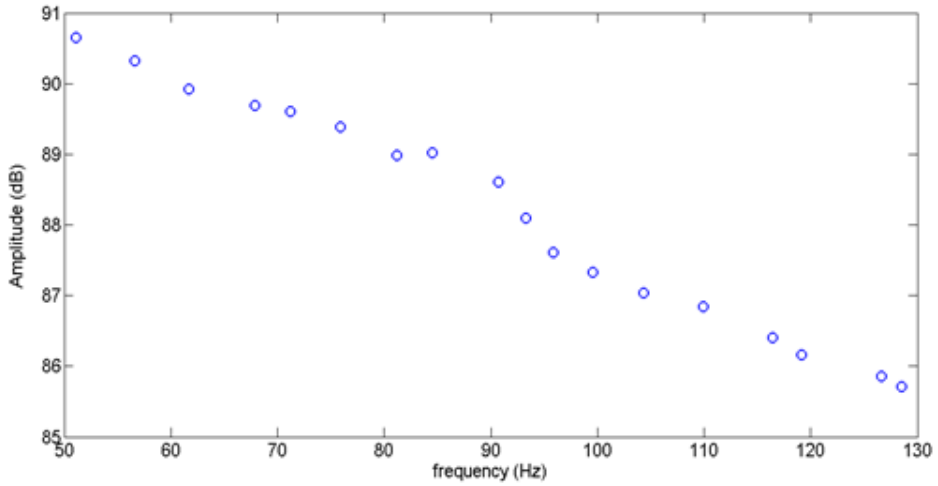

Figure 5.8: Amplitude vs. Chopping frequency for steel wool. Configurations: TA converter 2, fine steel wool (grade 0000), length of steel wool = 0.8 cm, microphone 1.

which the signal deviates from a perfectly periodic signal. Figure 5.9 shows that the signals obtained in Figure 5.8 had small distortion values.

It will be discussed in Section 5.4.9 that only the surface of the porous material and a small thickness beneath the surface of the porous material (steel wool in this case) were heated by incident radiation. In Section 5.4.8, it will be discussed that volume changes of air parcels due to thermo-acoustic effects were the highest near this surface. Consequently, effective cooling of this heated surface during chopped half-cycles encouraged higher "ac" or fluctuating air temperature ($T_{f,ac}$) and thereby encouraged higher acoustic amplitudes. The amplitude-frequency relation, however, was also affected by the geometry of the TA converter, which will be discussed in Section 5.4.6.

5.4.2 Presence of acoustic signal without any porous solid

It was observed that even with no steel wool or other porous materials placed within the TA converter, the microphone measured acoustic signals that were relatively

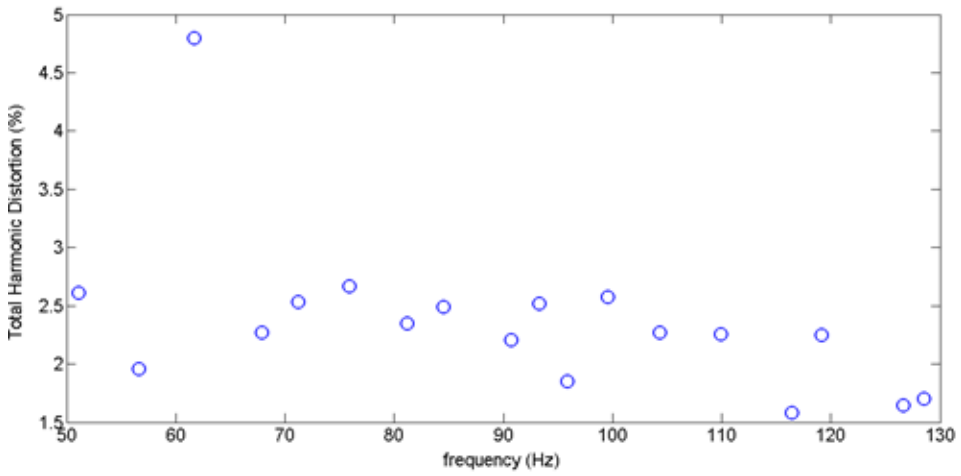

Figure 5.9: Total Harmonic Distortion (%) vs. Chopping Frequency (Hz) (corresponding to data in Figure 5.8).

lower in amplitude, but still detectable. Figure 5.10 shows the acoustic amplitudes obtained with no porous material housed inside the TA converter. The amplitudes in this test were comparable in magnitude to those presented in Figure 5.8, even though a much higher IR power level was applied in this case (IR power level was 65% here compared to 30% in Figure 5.8). This result confirmed the hypothesis that the heat transfer from the inner walls to the air inside the air column was responsible for a fraction of the acoustic amplitudes generated.

However, at 30% IR power level and 127.2 Hz, the recorded amplitude without any porous material was 0.254 V or 52.1 dB, which was about 10.5% of the acoustic amplitude (in voltage scale) obtained using steel wool as porous material (with the configurations same as that for Figure 5.8). The decrease in amplitude without any porous material could have been due to a couple of reasons. Without any porous media, the available surface area for heat transfer to air inside of the air column decreased. The only heat transfer occurred between the inner walls of the aluminum housing and the air

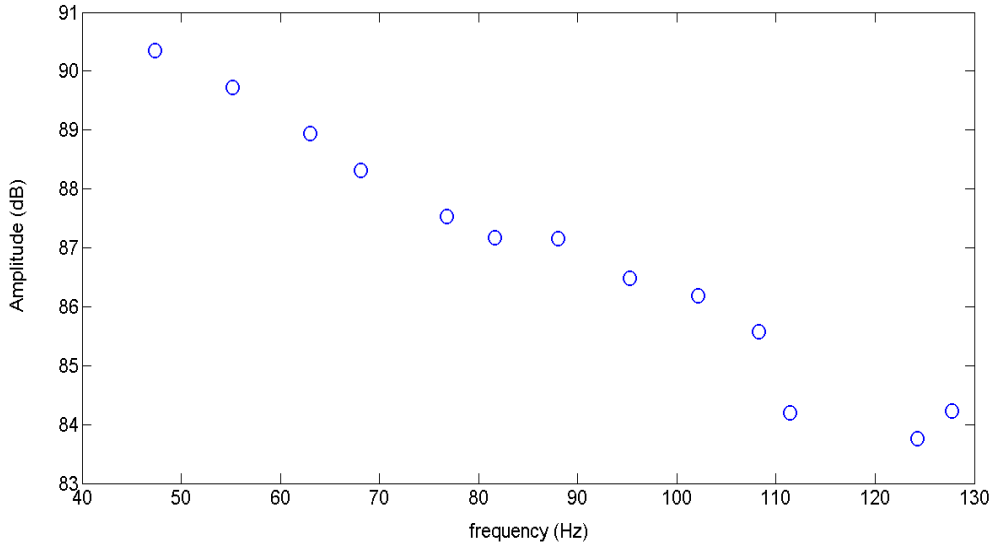

Figure 5.10: Amplitude v frequency with no porous material in the TA converter. Configurations: TA converter 2, microphone 1, IR power level at 65%.

close to the walls. Secondly, aluminum has a much greater thermal conductivity than steel wool, so there was greater heat loss to the surroundings. As a result, the surface temperature fluctuations of the inner walls of the aluminum housing were relatively lower.

5.4.3 IR power level

Figure 5.11 shows that the amplitude of acoustic waves (in logarithms of the decibel scale) varied linearly with the magnitude of incident radiation flux. This agreed with the analysis by Rosencwaig and Gercsho [25], who observed the same linear relation between the two parameters for monochromatic radiation.

Increasing the power level of IR heater increased the magnitude of the radiation flux. The linear relation between acoustic amplitude (in volts or ln (dB)) and IR power level proved that the increase in energy absorbed increased the fluctuating or “ac”

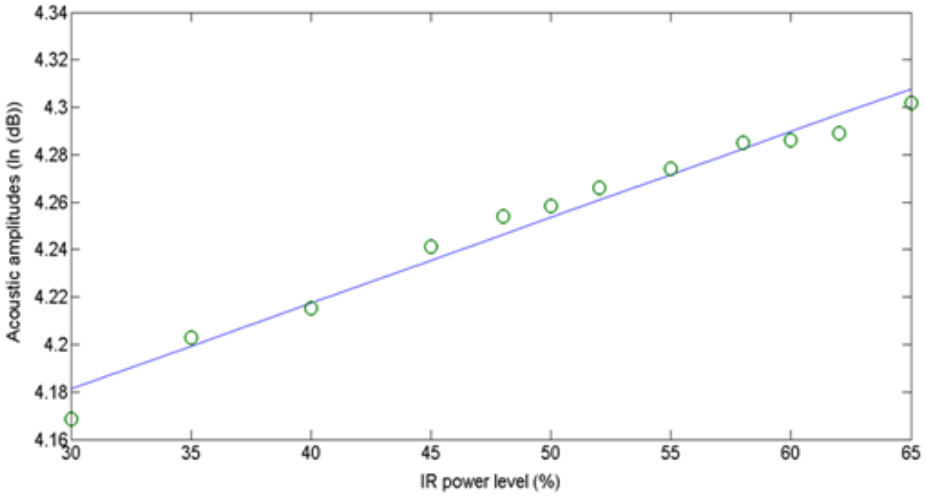

Figure 5.11: Amplitude vs. IR power level. Configurations: TA converter 1, fine steel wool (grade 0000), length of steel wool = 4.6 cm, microphone 1. IR power level was increased from 30% to 65%. Acoustic speed was maintained at 127.5 Hz.

component of temperature ($T_{f,ac}$), significantly more than it increased the mean temperature of air ($T_{f,mean}$) near the steel-wool surface.

5.4.4 Properties of the porous material

Amplitudes of TA waves were observed to depend upon the properties of the porous material. Figure 5.12 shows acoustic amplitudes for coarse (grade 3) and fine (grade 0000) steel wool as functions of the IR power level, showing that higher amplitudes were obtained for fine steel wool (grade 0000). In Section 3.2, it was shown that the thermal relaxation time for fine steel wool is several orders of magnitude lower than that for coarse steel wool. Therefore, fine steel wool filaments had better "thermal contact" with the air surrounding the filaments. Fine steel wool also had a larger surface area in contact with air between the filaments compared to coarse steel wool, which resulted in increased heat transfer from the filaments to the surrounding air.

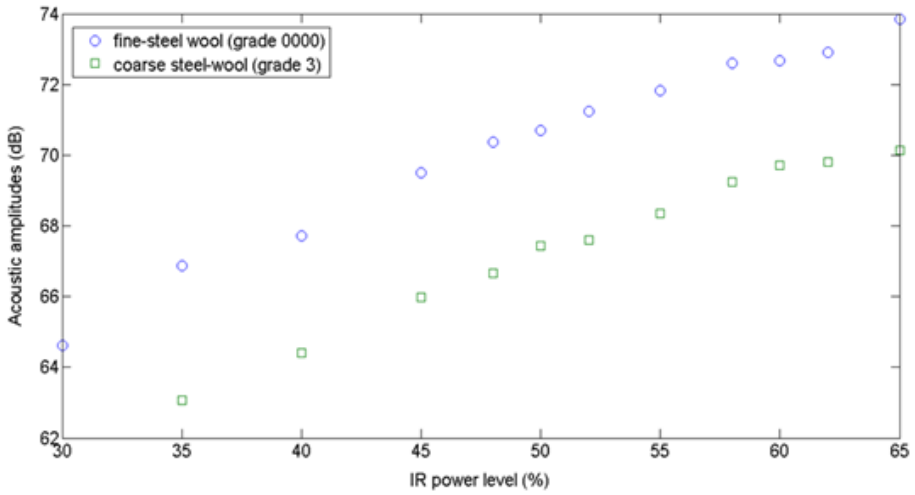

Figure 5.12: Acoustic amplitudes for coarse and fine steel wool at different IR power levels. Configurations: TA converter 1, fine (grade 0000) and coarse (grade 3) steel wool, length of steel wool = 4.5 cm, microphone 1. Acoustic frequency was maintained at 127 Hz.

Consequently, the acoustic amplitudes obtained for fine steel wool were higher.

Figure 5.13 compares the results obtained using brass wool and steel wool of the same grade and shows that steel wool produced higher acoustic signal, possibly due to its higher absorptivity to thermal radiation. The physical properties of bulk steel and brass are given in Table 5.1 [69]. It was assumed that the properties of steel-wool filament are identical to those of low-carbon iron and that the absorptivity values for iron and brass are "total absorptivity values."

The combined conductivities of both steel wool and brass wool are expected to be much lower than those for bulk iron and brass. The combined conductivity (k_m) of the porous material was bounded by the upper and lower limits (k_h and k_l) for a given porosity (φ), which could be calculated assuming all heat transfer by conduction

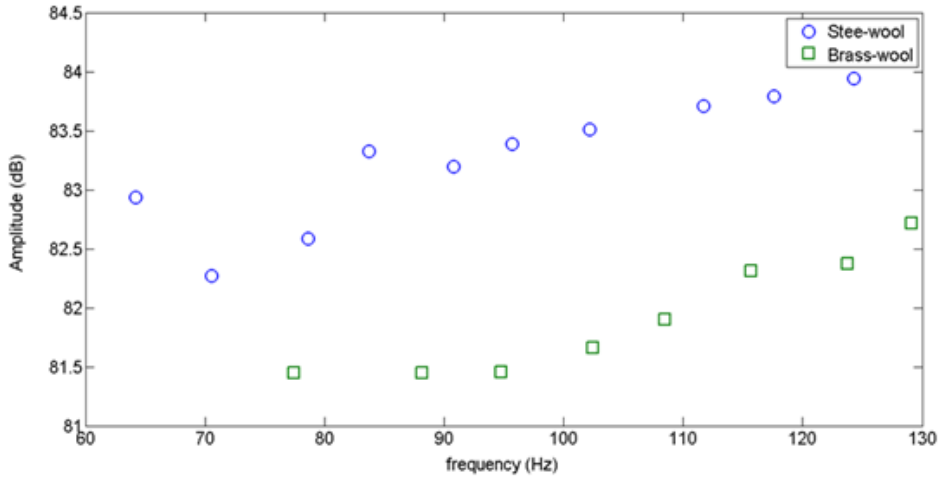

Figure 5.13: Acoustic behavior for steel wool and brass wool. Configurations: TA converter 3, fine steel wool and brass wool (grade 0000), length of porous medium = 0.4 cm, IR power level at 65%.

between the solid and air occurred in parallel and in series, respectively [74]:

$$k_h = (1 - \varphi)k_s + \varphi k_f \tag{5.6}$$

$$1/k_l = (1 - \varphi)/k_s + \varphi/k_f \tag{5.7}$$

Here φ is the ratio of the volume of air within the porous medium to the total volume contained within the porous medium. In reality, the combined conductivity lies between these two bounds. A rough estimate could be obtained by calculating the geometric mean of the conductivities of the bulk solid and air:

$$k_m = k_s^{(1-\varphi)} kf_\varphi \tag{5.8}$$

Table 5.1: Physical properties of bulk brass and iron

	Thermal conductivity (W/mK)	Absorptivity
Iron	80	0.31
Brass	109	0.06

For $\varphi = 0.5$ and $k_f = 0.024$ W/mK (for air), the combined conductivities of steel wool/air and brass wool/air media were calculated as 1.38 W/mK and 1.61 W/mK, respectively, in which case the brass wool/air medium only has a 16% higher conductivity compared to steel wool/air medium. This partly negated the increased conductivity of brass (36%) compared to steel (Table 5.1). The actual porosity of steel wool is likely to be much lower [75] and it can be shown that at lower porosities, the difference in combined conductivity between brass wool/air and steel wool/air would be even lower.

It should be pointed out that the amplitude-frequency variation for steel wool in Figure 5.13 was found to be different from those presented and discussed in Section 5.4.1 because different TA converters were used.

5.4.5 Transient behavior of thermo-acoustic signals

In this thesis, the term “transient” will be used to refer to the change in RMS amplitude of acoustic waves over an interval much greater than the period of the acoustic oscillations. Figure 5.14 shows the amplitude of acoustic oscillations over 9.6 s interval.

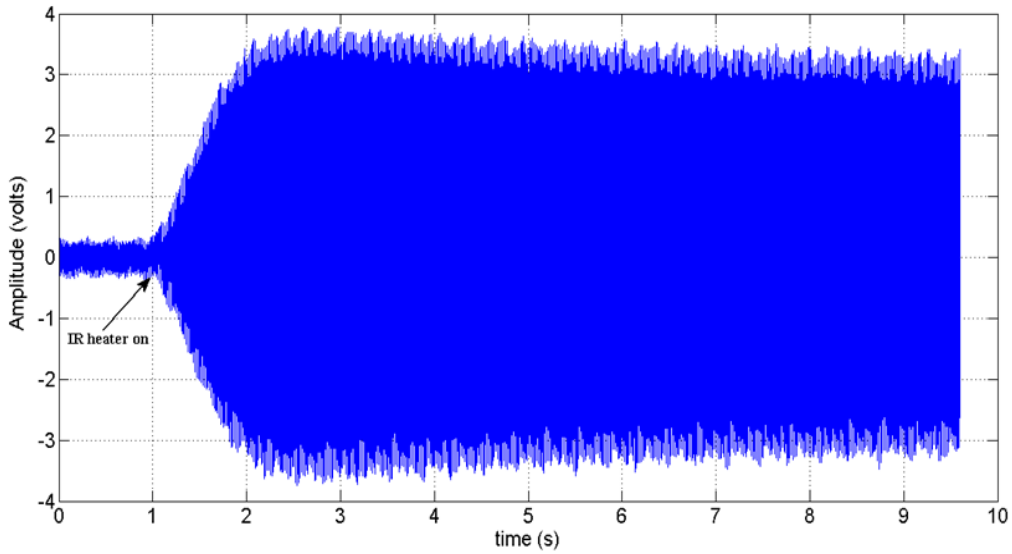

Figure 5.14: Time-domain data for 116 Hz. Configurations for this experiment: TA converter 3, fine steel wool (grade 0000), length of steel wool = 0.8 cm, microphone 1, IR power level at 30%. Sampling configurations were 48000 samples at a sampling frequency of 5 kHz.

To investigate the change in amplitude (RMS), the amplitude data collected from t = 0 to 8.6 s was divided into 24 intervals, where the time t = 0 s was set at the instant when IR heater was turned on. Root mean square (RMS) amplitudes for each of these intervals were calculated and the corresponding variation of RMS amplitudes versus "t" was then plotted (Figure 5.15).

Both Figures 5.14 and 5.15 show that the acoustic amplitude steeply increased from t = 0 s to t = 1 s, after which it slowly decreased to a "steady" value (although "steady-state" was not achieved within the 8.6 interval).

During the first 1 to 2 s after turning on the IR heater, the mean temperature of the steel-wool filaments ($T_{s,mean}$) was greater than the mean temperature of air between the filaments ($T_{f,mean}$). Thus, the temperature difference between the mean temperature of the

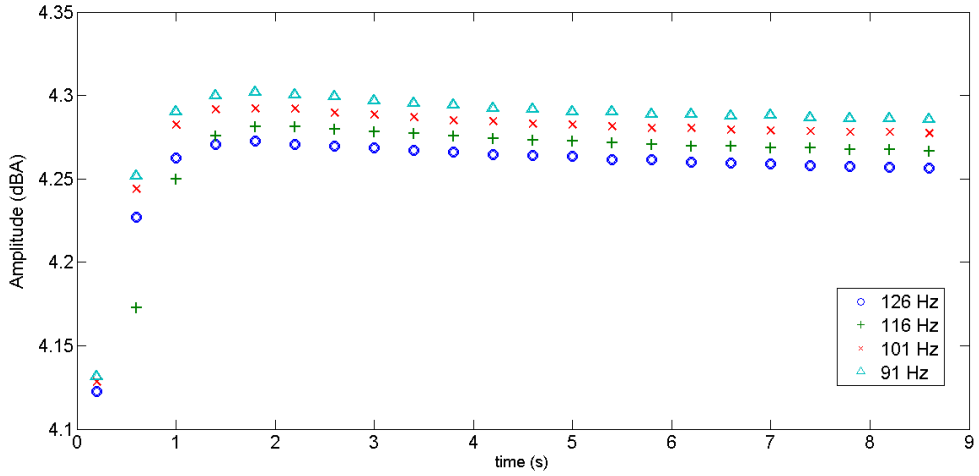

Figure 5.15: RMS amplitudes vs. "t" at different frequencies.

filament and the mean air temperature was high, resulting in a high rate of heat transfer and a steep increase in sound amplitude. After $T_{s,mean}$ reached a steady value within 1 to 2 s, $T_{f,mean}$ continued to increase, and so the temperature difference $(T_{s,mean} - T_{f,mean})$ decreased.

It was observed that at higher frequencies, the amplitude had a slightly steeper decline compared to lower frequencies after the maximum amplitude had been reached. This observation is illustrated in Figure 5.16. "$t_{95\%}$" was calculated as the time taken for the amplitude to drop to 95% of its maximum value, which decreased with increasing frequency. This can be explained by considering the fact that at lower frequencies, the energy absorbed per cycle by the steel wool was higher compared to that absorbed at higher frequencies, resulting in an increase in $T_{s,mean,}$ as well as the temperature difference $(T_{s,mean} - T_{f,mean})$. Although $T_{f,mean}$ also increased over time intervals much greater than the acoustic time period, the increase in the temperature difference was substantial due to the additional "instantaneous" adsorption of energy at lower frequencies.

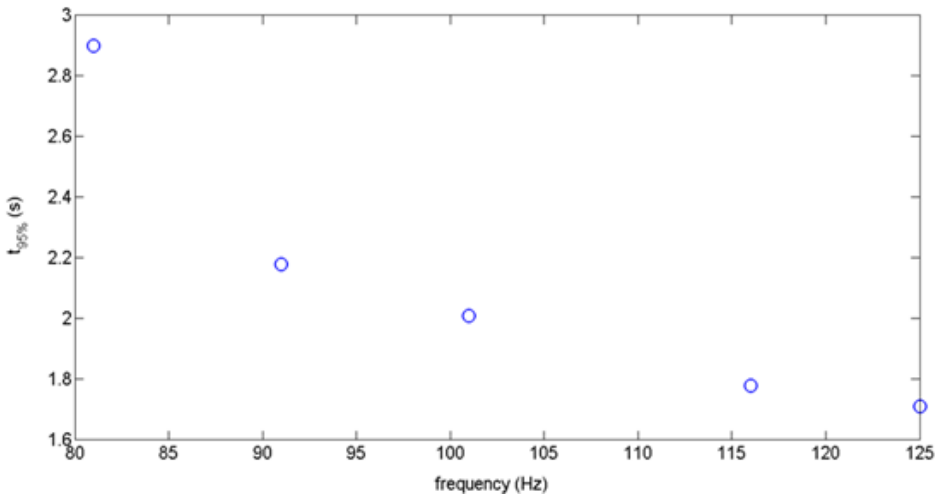

Figure 5.16: Variation of t_{95}% with frequency. t_{95}% was determined with respect to voltage scale.

Figure 5.17 further illustrates the transient effect on acoustic amplitude. The "transient" data was collected after the first 2 seconds of generation of acoustic waves and was taken in four runs: two runs in decreasing order of frequency and two runs in increasing order of frequency. Figure 5.15 shows that maximum "transient" amplitude was reached after 1.5 seconds of generation of acoustic waves, so the amplitudes obtained at each of these four runs were close to maximum. The time interval between two successive transient experimental runs was 1 minute. The "steady-state" data, on the other hand, was taken 60 s after the IR heater was turned on (i.e., t = 60 s), when there was almost no drop in amplitude with time.

The plot shows that the "steady state" amplitude was lower than the maximum transient amplitude over the 50–130 Hz frequency range. It further re-iterates the fact that the maximum transient amplitude was reached at a short time interval (about 1 to 2 s) after the heating started.

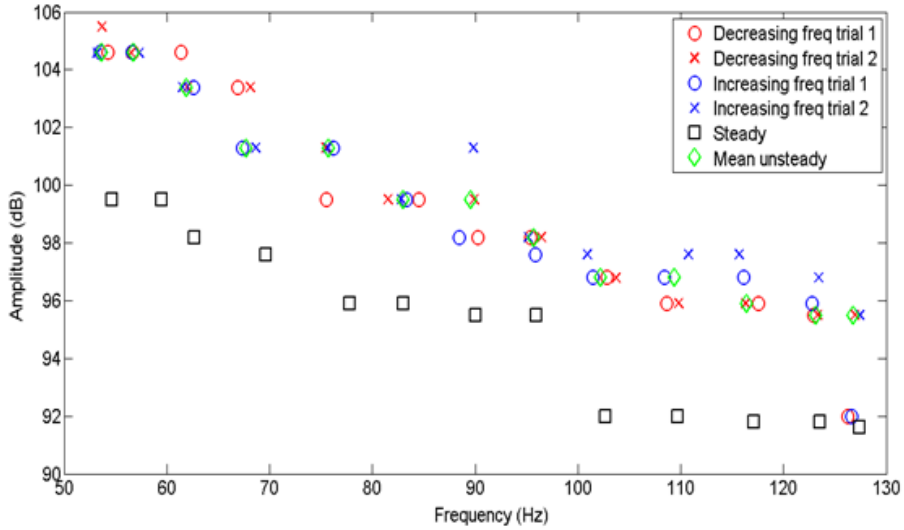

Figure 5.17: Transient effect on acoustic amplitude – transient and steady state data. Configurations: TA converter 1, fine steel wool (grade 0000), microphone 2 located at 0.6 cm from the steel wool, IR power level at 65%.

5.4.6 Effect of preheating the TA converter

Externally preheating the TA converter decreased the magnitude acoustic amplitudes as it increased the temperature of the aluminum body as well as the initial temperature of air inside the air column. To test this effect, the TA converter was first heated with a heat gun (250 W) for 5 minutes. The amplitudes were observed to reduce by 20% in the voltage scale (93.2 dB with no heating compared to 90.6 dB with external heating at an acoustic frequency of 125 Hz.). Figure 5.18 shows the time-domain data for 125 Hz with external heating. Figure 5.19 shows the effect of external heating on sound amplitude at different acoustic frequencies. Heating the aluminum body inhibited the cooling of air in space between the filaments during the "chopped" half-cycles (i.e., half-cycles when the radiation beam was interrupted by the chopper). As a result, there was a smaller temperature difference between the steel-wool filament temperature and the mean air temperature, which resulted in a decrease in acoustic amplitude.

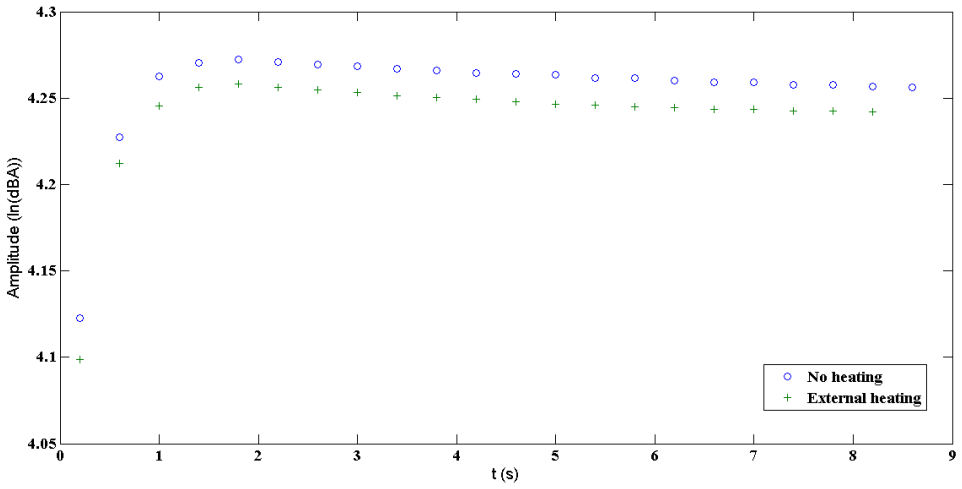

Figure 5.18: Effect of external heating (125 Hz). Configurations for this experiment: TA converter 3, microphone 1, fine steel wool (grade 0000), length of steel wool = 0.8 cm, IR power level at 30%.

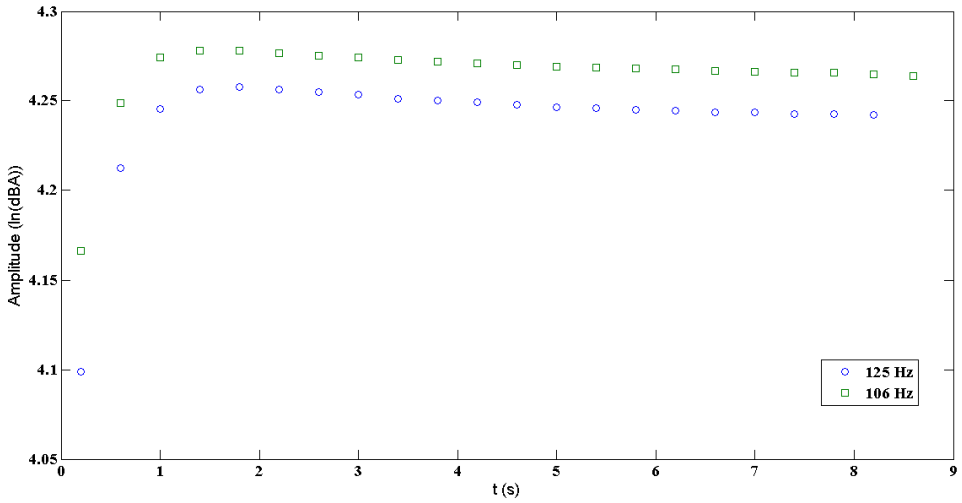

Figure 5.19: Effect of External heating on sound waves at 125 Hz and 109 Hz. Configurations same as those presented for Figure 5.18.

5.4.7 TA converter design

5.4.7.1 The diameter of the TA converter opening. The diameter of the TA converter influenced the magnitude of acoustic amplitudes, as well as the pattern of amplitude variation with frequency. Higher amplitudes were obtained for TA converter 3 compared to those for TA converter 2 (TA converters 2 and 3 have identical design, except that TA converter 3 has a larger diameter of TA converter opening).

Figure 5.20 shows the overlapped area between the chopper hole and the TA converter opening as a function of time (as derived in Section 5.2), for TA converter 2 (diameter of opening = 1.3 cm) and TA converter 3 (diameter of opening = 1.6 cm). The area under curve (AUC) in the plot of overlapped area versus time for TA converter 3 is 51% greater than AUC for TA converter 2. Thus, significantly higher radiation energy was incident on porous steel wool inside TA converter 3 compared to TA converter 2.

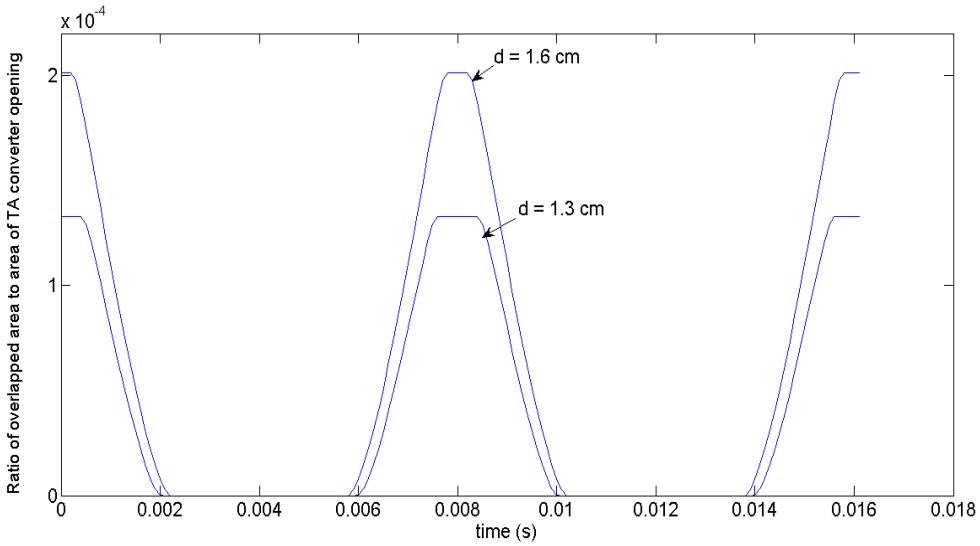

Figure 5.20: Overlapped area as a function of time for TA converter 2 (diameter of opening = 1.3 cm) and TA converter 3 (diameter of opening = 1.6 cm) at 125 Hz.

Figure 5.21 shows that when the diameter of the opening was 1.6 cm (as was the case in TA converter 3), the acoustic amplitudes were found to be constant with respect to frequency. This observation does not conform to the trends observed in previous test results using TA converters 1 and 2, which showed that amplitudes increased with decreasing frequency. One possible explanation for this observation could be that when the diameter of the opening increased from 1.3 cm to 1.6 cm, the radius of the heated area on the steel-wool surface (on which radiation was incident) became significantly greater than the radius of the air column, such that when chopping frequency was decreased (and thereby exposure time for radiation was increased), the additional radiation energy per cycle increased the mean air temperature ($T_{f,\ mean}$), without significantly increasing the fluctuating or "ac" air temperature ($T_{f,ac}$). (This hypothesis is further illustrated in Figure 5.22).

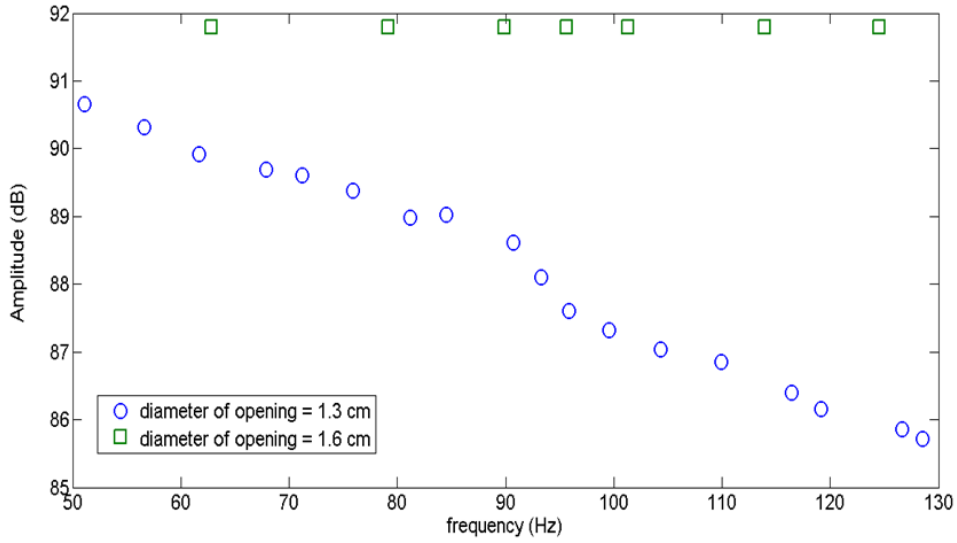

Figure 5.21: Effect of TA converter opening diameter. Configurations: TA converters 2 and 3, fine steel wool (grade 0000), length of steel wool = 0.8 cm, IR power level at 30%.

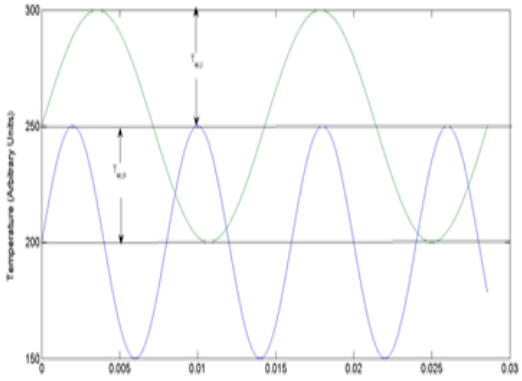

Large opening diameter (TA converter 3)

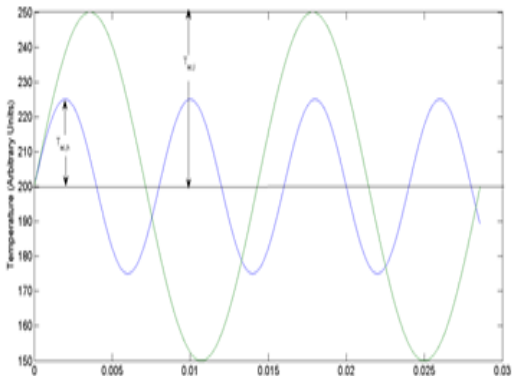

Small opening diameter (TA converters 1 and 2)

Figure 5.22: Conceptual representation of the effect of size of TA converter opening on temperature of air in contact with heated filaments. (The temperatures are given in arbitrary units and do not represent the actual temperatures in the experiments.)

The higher heating area in case of TA converter 3 inhibited the cooling effect during chopped half-cycles. As a result, the amplitudes did not increase with decreasing frequency.

This amplitude-frequency pattern was not observed for TA converters 1 and 2, as with a smaller diameter of opening and a smaller heating area, the radial temperature gradient was much greater than it was in the case of TA converter 3. This resulted in a more effective cooling of the heated steel-wool filaments and the air surrounding the filaments during the chopped half-cycles and so the incident radiation during the unchopped half-cycles increased the "ac" temperature ($T_{f,ac}$) significantly more than the mean or "dc" temperature ($T_{f,\,mean}$), when frequency was decreased.

5.4.7.2 Diameter of air column. Increasing the diameter of the air column increased the volume of air inside the air column, which reduced the amplitude of acoustic waves. (It will be explained in Section 5.4.8 that increasing the volume of air had an adverse effect on the amplitude of acoustic waves.) The radius of the air column

in TA converter 1 is 3.72 times the radius of the air column in TA converter 2, with the diameters of both converter openings being equal. TA converter 1 produced an acoustic signal of magnitude 89.40 dB at 127.90 Hz, compared to 100.27 dB produced by TA converter 2 at the same frequency, both at 65% IR power level. The acoustic signals were measured at a distance of 3.2 cm for both TA converters. This showed that an increase in diameter of the air column reduced the amplitude of acoustic waves.

5.4.8 Location of microphone

Figure 5.23 shows the acoustic amplitude diminished with increasing distance (and thereby increasing volume of air) between the porous solid and the microphone. Pressure fluctuations in air, which are a function of volume and temperature fluctuations, decreased with an increase in the volume of air. The amplitude of pressure fluctuations (which are responsible for sound generation) is proportional to the ratio of the change in air volume due to thermal displacement of an "imaginary" gas piston near the irradiated surface (ΔV) responding to the periodic heating, to the overall air volume (V). It could be hypothesized that with increasing distance between the porous material and the microphone, the air volume increased whereas the volume change of the "gas-piston" remained the same (i.e., $\Delta V1 = \Delta V2$ but $V1 < V2$ in Figure 5.24.). As $\Delta V2/V2 < \Delta V1/V1$, lower acoustic amplitudes were obtained for increasing volume of air (Figure 5.24).

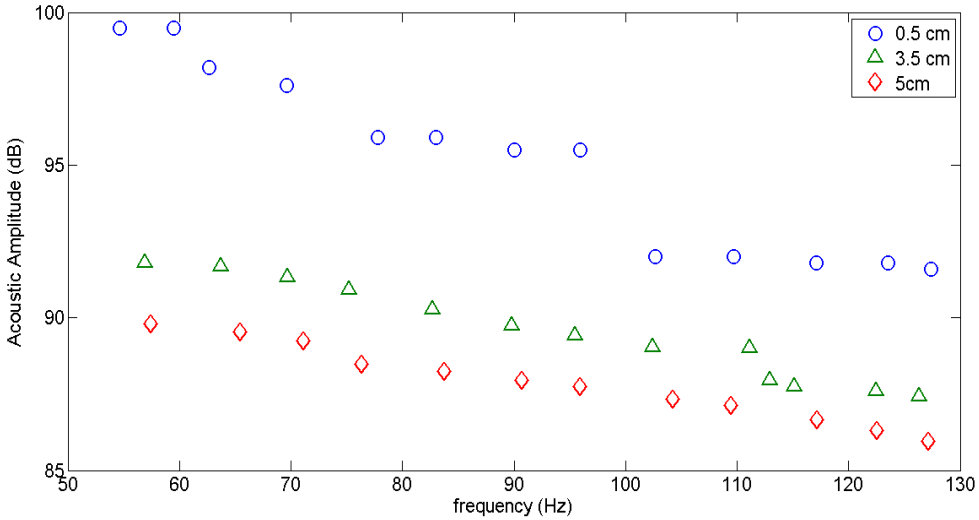

Figure 5.23: Amplitude vs. frequency at various microphone locations. Configurations: TA converter 1, fine steel wool (grade 0000), length of porous material = 0.8 cm, IR power level at 65%.

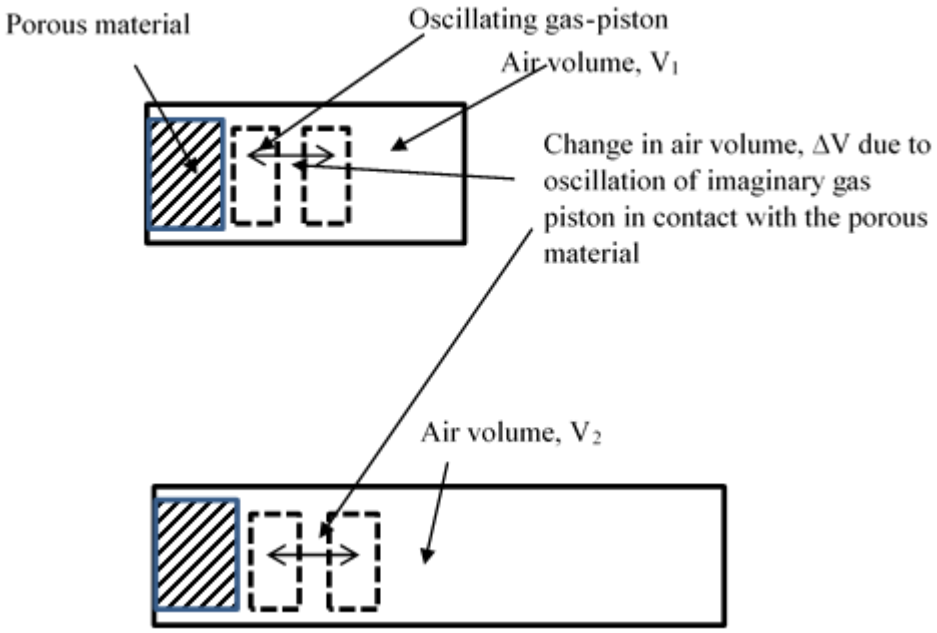

Figure 5.24: Conceptual representation of thermal expansion of air volume due to thermo-acoustic effects.

5.4.9 Length of porous material

Acoustic amplitudes increased with increasing length of the porous material, up to an optimal length of about 0.75 cm. Above this optimal length, increasing the length of the steel wool reduced acoustic amplitudes, particularly at low frequencies (Figure 5.25).

Temperature fluctuations took place on the surface and within a small depth into the surface of the steel wool. According to the Beer–Lambert's law, the radiation flux decays exponentially with increasing axial distance from the surface of the porous solid (as presented below):

$$q'' = q''_{(abs,\, z=0)}[\exp(-\alpha' z)] \tag{5.9}$$

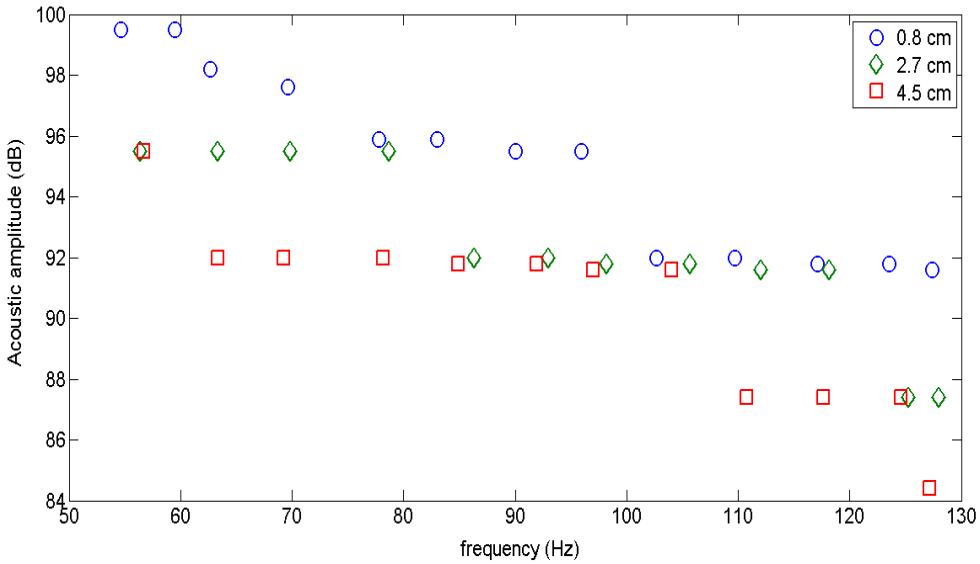

Figure 5.25: Effect of length of steel wool on acoustic amplitude. Configurations: TA converter 1, fine steel wool (grade 0000), location of 0.5 cm from the steel wool, IR power level at 65%.

Here, α' is the extinction coefficient and $q''_{(abs\ z\ =\ 0)}$ is the amount of incident radiation on the steel wool surface. "z" presents the axial distance measured from the surface of the porous solid on which IR radiation is incident. For the given diameter of steel-wool filaments, the extinction coefficient can be estimated as α' = 600 m – 1 [76]. Using the Beer–Lambert's law, it can be calculated that the radiation flux at a length of 0.8 cm from the surface of the porous medium reduces to 8.2% of the radiation flux at the surface. As temperature fluctuations occurred on and near the surface of the porous steel wool, increasing in length of porous steel wool beyond a certain optimum length did not increase the effective surface area for heat transfer.

Two other factors might also have contributed to the decrease in acoustic amplitude with an increase in porous material length (beyond the optimum length). The first was the increase in air volume due to an increase in the length of the porous material. For tests in Figure 5.25, the distance between the microphone and the porous steel wool was kept constant at 0.5 cm. However, the air volume inside the porous steel wool also increased with increasing length. In Section 5.4.8, it was explained how an increase in air volume decreased the amplitude of acoustic waves. The "total air volume," which includes the air volume between the porous material (i.e., steel wool in this case) and the microphone as well as the air contained inside the steel wool, increased with increasing length. Thus, the "total air volume" was the greatest for a steel wool length of 4.5 cm (Figure 5.26). The other factor that might have caused a decrease in acoustic amplitude with increasing length of porous material is viscous dissipation. Increasing the length of the porous material increased the friction between the air flow and the porous medium.

However, too short a porous plug (i.e., decreasing the length below the optimal

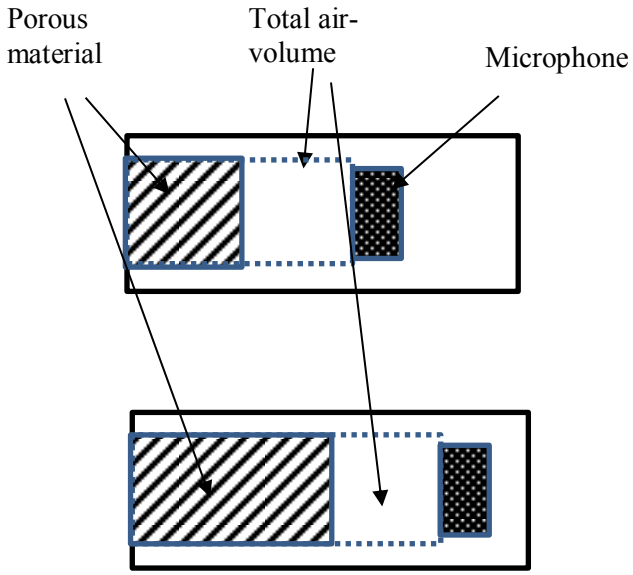

Figure 5.26: Schematic diagram showing the increase in air volume due to an increase in length of porous material.

length) could decrease the amplitude of acoustic waves, as observed in Figure 5.27. When the length of steel wool was below the optimum length, incident radiation was not fully absorbed by the porous steel wool. As a result, the surface area for heat transfer from the heated filaments to the air in space between the filaments was also lower. Secondly, reducing the length too much decreased the contact area between the steel wool and the aluminum body, thereby inhibiting the cooling effect during the "chopped" half-cycles.

5.5 Solar to acoustic energy conversion

Figure 5.28 shows how the RMS amplitude varied with chopping frequency. Below 1 kHz, the acoustic amplitudes decreased with increasing frequency. However, above 1 kHz, there was very little change in amplitude with increasing frequency. The

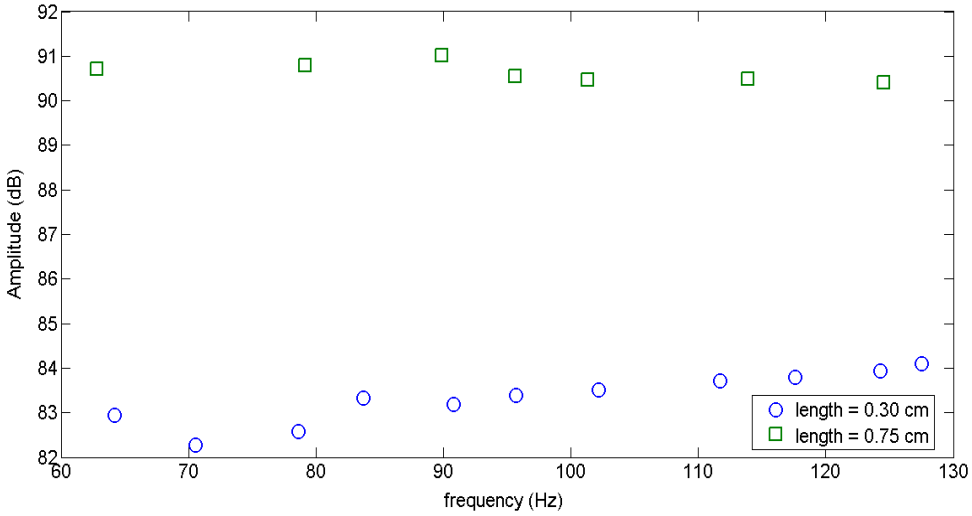

Figure 5.27: Effect of length of steel wool on acoustic amplitude. Configurations: TA converter 3, fine steel wool (grade 0000), microphone 2, location of 3.2 cm from the steel wool.IR power level kept at 30%.

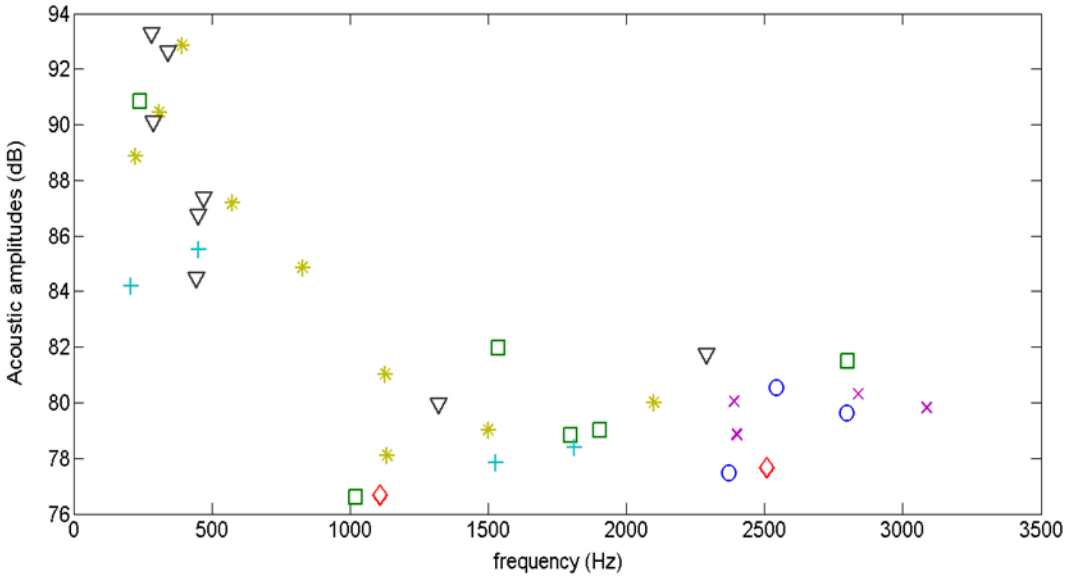

Figure 5.28: Amplitudes of acoustic waves generated from solar radiation – variation with acoustic frequency (Different marker types indicate different data sets). Configurations: TA converter 1, fine steel wool (grade 0000), length of porous material = 4.5 cm, microphone 1.

amplitudes in volts were converted to dBA and subsequently to dB using the calibration plots (Appendix A).

The data presented in Figures 5.28 and 5.29 were all taken between 12 PM–3 PM during the period of May to September. The solar radiation flux corresponding to the frequency-dependent amplitudes in Figure 5.28 are presented in Figure 5.29. All sets of data were taken on sunny days. The radiation flux recorded (Figure 5.29) had a mean value of 1.02 KW/m^2 and a standard deviation of 0.02 KW/m^2. The actual solar flux entering through the TA converter opening was much higher than this mean flux (which was obtained using a solar pyrometer aligned to the sun) as a plastic Frensel lens was used to concentrate the incident solar radiation. The magnitude of radiation flux entering the TA converter will be discussed in greater detail in Section 5.5.3.

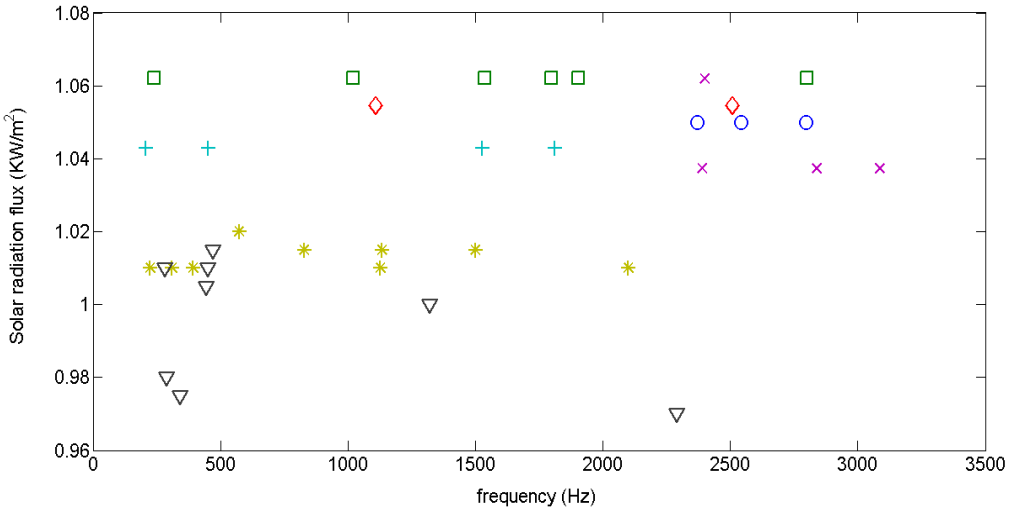

Figure 5.29: Solar flux data corresponding to data in Figure 5.28

5.5.1 Filter configurations

In this analysis, a second-order Butterworth filter was used to remove noise, primarily because of signals arising due to vibration of cart. (This will be explored in detail later in this section.) Butterworth filters require two parameters: the cutoff frequency and the filter order, the latter of which determines the "sharpness of transition from pass-band to stop-band" [77].

The transfer function for a second-order high-pass Butterworth filter can be expressed as [76]

$$H(\mathrm{s}) = \frac{1}{\left(\frac{w_c}{s}\right)^2 + \sqrt{2}\left(\frac{w_c}{s}\right) + 1} \tag{5.10}$$

Here, H(s) is the transfer function, w_c is the cutoff frequency, and s is a Butterworth polynomial. In this thesis, high-pass filters were used to remove low-frequency noise. The cutoff frequency for these filters was 70 Hz for all acoustic signals below 500 Hz and 500 Hz for acoustic signals above 500 Hz. Built-in MATLAB functions were used to generate the Butterworth polynomials.

5.5.2 Analysis of signal obtained

Figures 5.30 and 5.31 show sample acoustic signals (unfiltered and filtered) at an acoustic frequency of 244 Hz. (The acoustic frequency was found to be almost equal to the chopping frequency, as explained in Section 5.1). The RMS amplitude of the signal dropped from 1.38 V or 87.577 dB to 1.36 V or 87.430 dB after passing through a high-pass Butterworth filter with a cutoff frequency of 70 Hz. The drop in RMS amplitude was

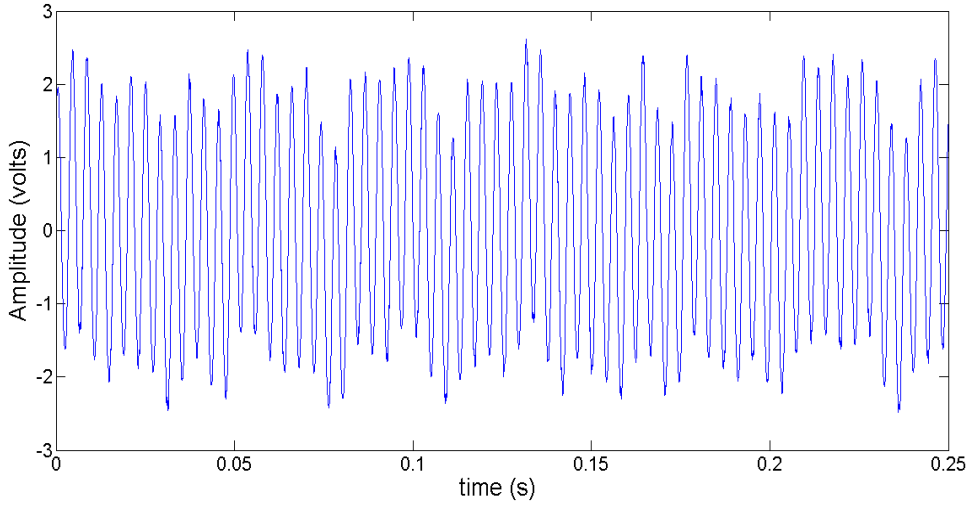

Figure 5.30: Unfiltered signal at acoustic frequency of 244 Hz

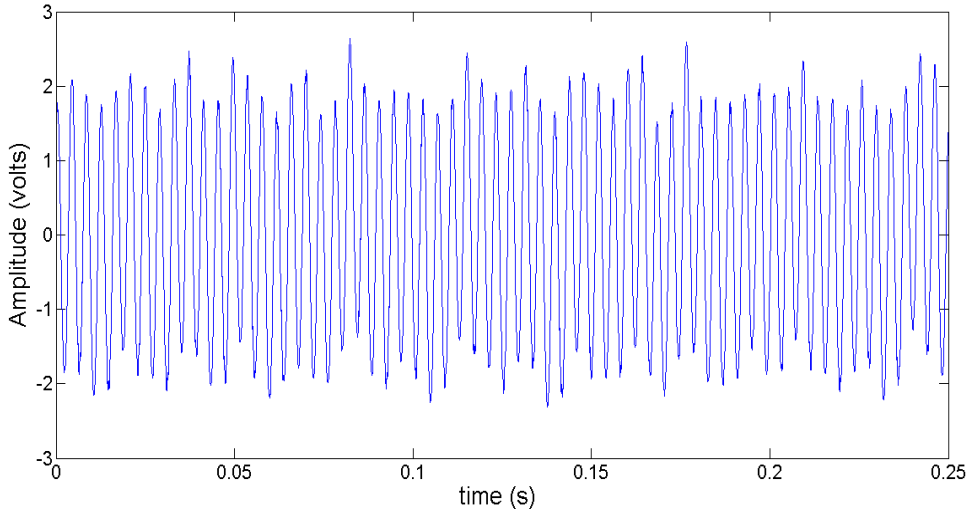

Figure 5.31: Filtered signal at 244 Hz (cutoff frequency = 70 Hz)

almost negligible, about 0.7% in the voltage scale.

FFT plots of the unfiltered and filtered signals in Figures 5.30 and 5.31 are presented in Figures 5.32 and 5.33, respectively. Both plots show a significant peak at 244 Hz, which corresponds to the frequency of the acoustic signal. Much shorter peaks were observed in frequencies below 100 Hz, which were present possibly due to internal microphone noise and vibration of the cart arising from rotation of chopper wheel. Figure 5.33 shows that after applying the filter, signals with frequencies below 70 Hz were removed.

Figures 5.34 and 5.35 show the unfiltered and filtered acoustic signals obtained at an acoustic frequency of 451 Hz. Comparisons between the unfiltered and filtered signals showed a similar observation to those obtained for signals at 244 Hz. The RMS acoustic amplitude dropped from 1.09 V or 85.700 dB to 1.076 V or 85.42 dB. The drop in amplitude was small (almost 1%) showing that the background noise had little effect on unfiltered signals for frequencies below 500 Hz.

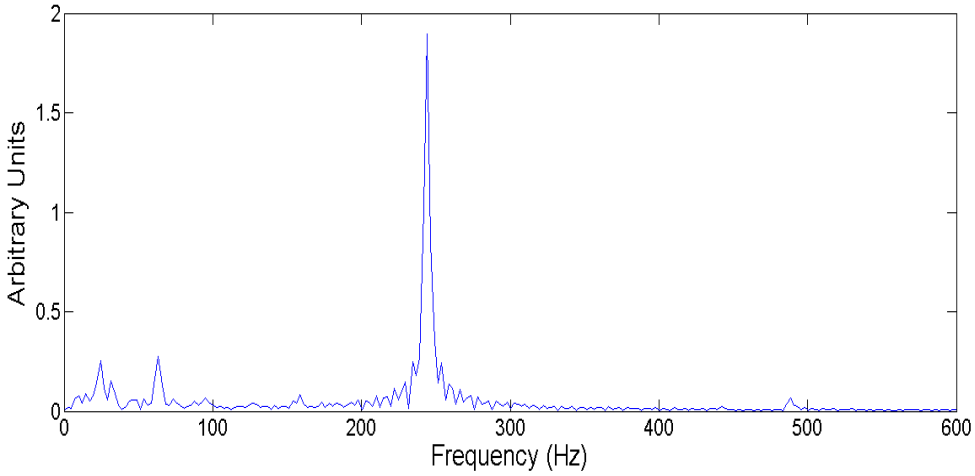

Figure 5.32: FFT analysis—unfiltered signal at an acoustic frequency of 244 Hz

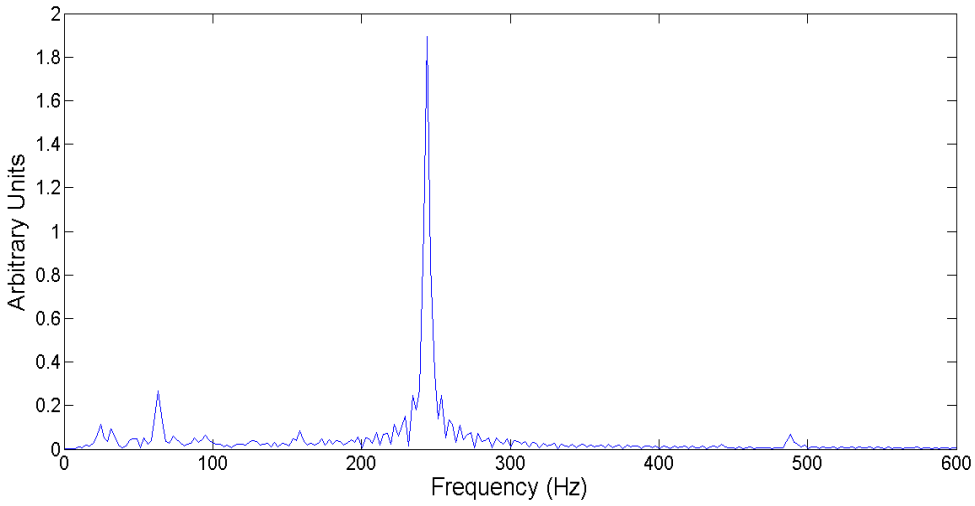

Figure 5.33: FFT analysis—filtered signal at 244 Hz (cutoff frequency = 70 Hz)

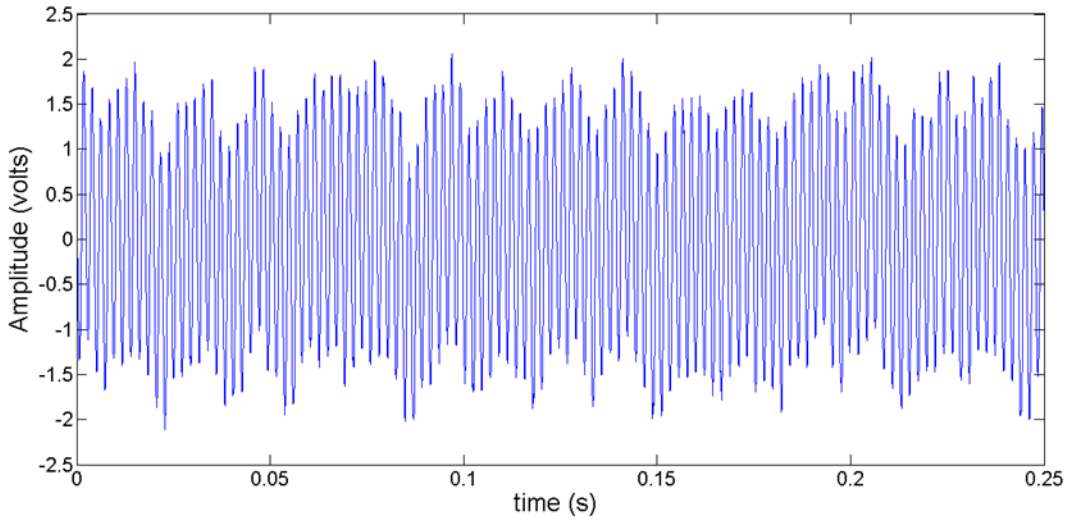

Figure 5.34: Unfiltered signal at an acoustic frequency of 451 Hz

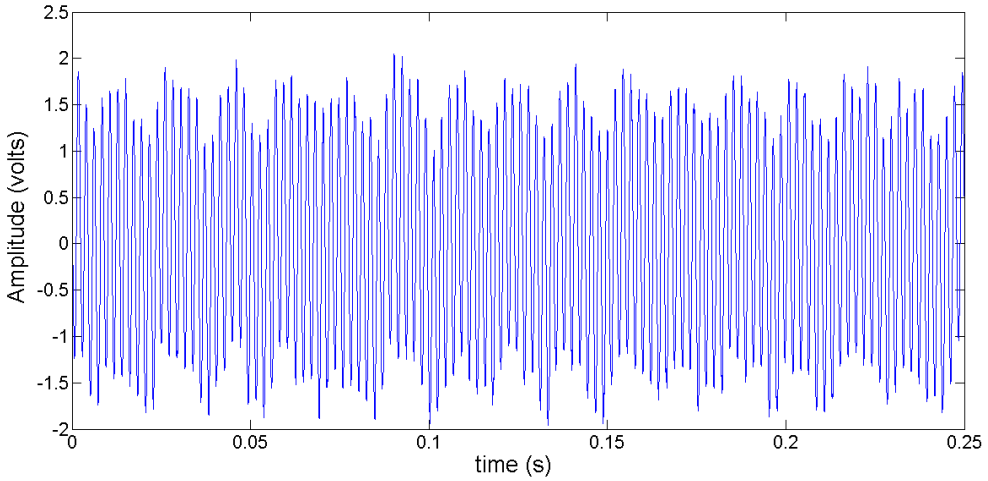

Figure 5.35: Filtered signal at 451 Hz (cutoff frequency = 70 Hz)

The amplitude decreased significantly when the acoustic frequency was increased from 244 Hz to 451 Hz. For unfiltered signal, the amplitude drop due to an increase in frequency was almost 29% (taking the amplitude at 244 Hz as the base value). As explained previously in Section 5.4.1, this was due to the fact the total radiation energy absorbed per cycle decreased that with increasing frequency.

Figures 5.36 and 5.37 show the corresponding FFT plots for unfiltered and filtered signals at a frequency of 451 Hz. There is little difference between the two plots as the effect of noise was low for comparatively lower frequencies. The unfiltered FFT plot shows the presence of "noise" frequencies, but the magnitude of the peaks was small, with the most significant peak being at 63.5 Hz. Figure 5.38 shows that when the unfiltered signal is passed through a filter with a higher cutoff frequency (300 Hz), the raw or unfiltered signal was further "smoothed," as noise frequencies over a wider range were removed.

Figures 5.39 and 5.40 show unfiltered and filtered signals obtained at an acoustic

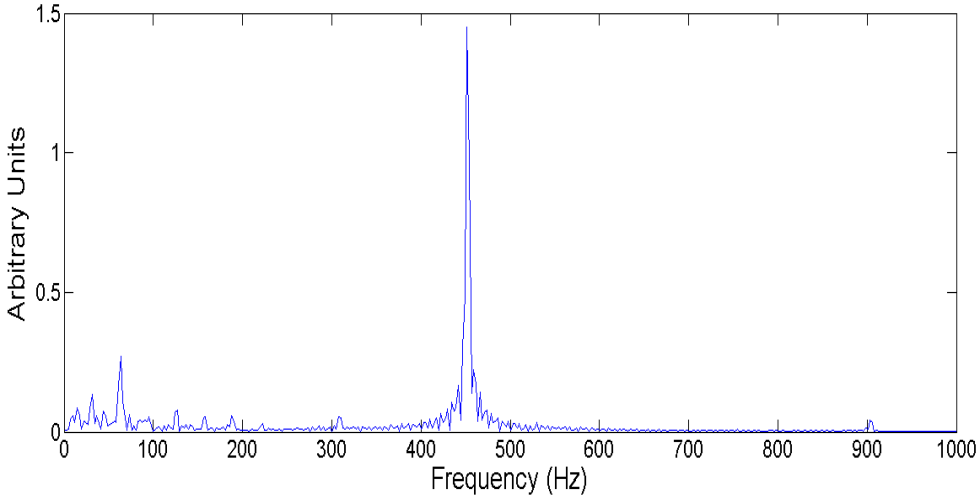

Figure 5.36: FFT analysis—unfiltered signal at an acoustic frequency of 451 Hz

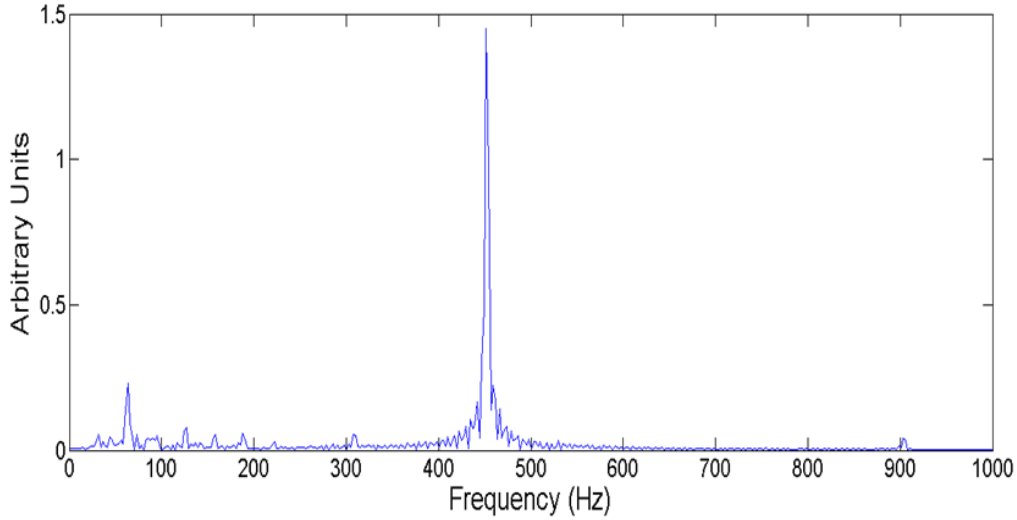

Figure 5.37: FFT analysis—filtered signal at 451 Hz (cutoff frequency = 70Hz)

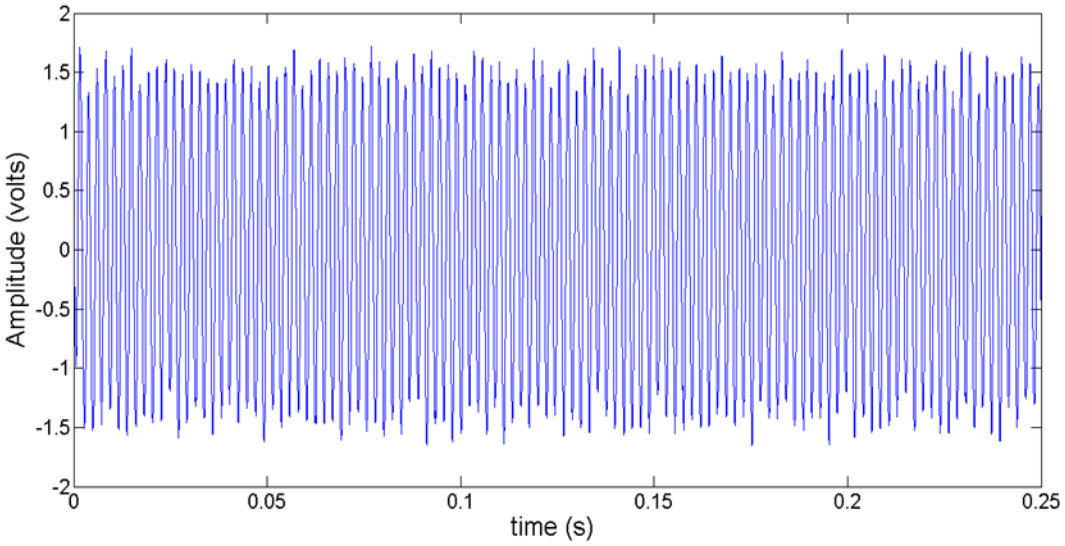

Figure 5.38: Filtered signal at 451 Hz (cutoff frequency = 300 Hz)

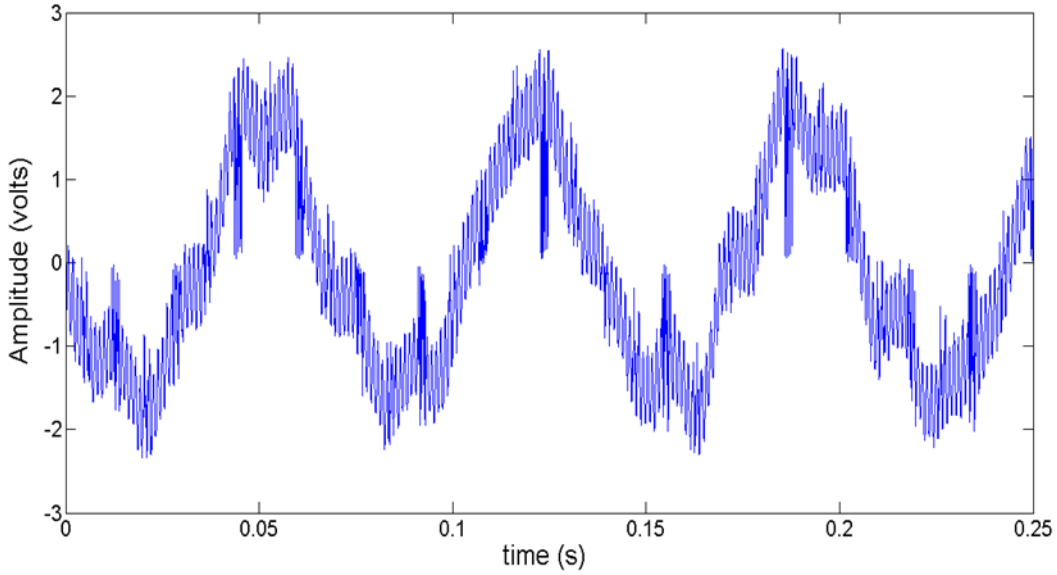

Figure 5.39: Unfiltered signal at an acoustic frequency of 860 Hz

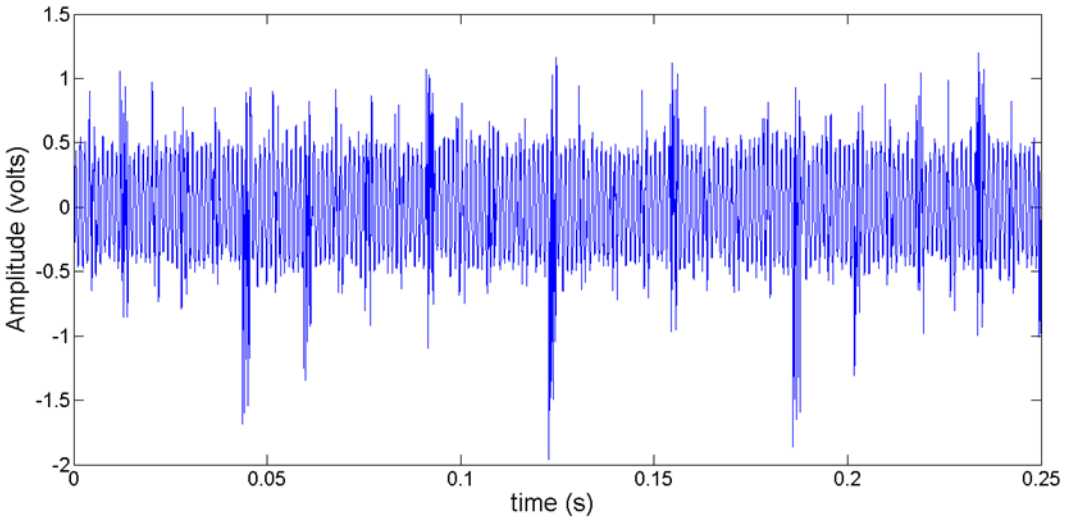

Figure 5.40: Filtered signal at 860 Hz (cutoff frequency = 500 Hz)

frequency of 860 Hz. As the acoustic frequency was much higher than the previous two cases (244 and 451 Hz), it was possible to use a filter with a higher cutoff frequency (500 Hz). The drop in RMS amplitude after filtering the raw signal was 34.2% in the voltage scale (0.51 V or 82.23 dB to 0.38 V 82.012 dB). The reduction in amplitude from unfiltered filtered signal was significantly higher compared to that at low frequency (244 Hz), primarily due to the higher cutoff frequency of the filter. FFT analyses of the two time-domain signals are presented in Figures 5.41 and 5.42. The FFT plot of the unfiltered signal (Figure 5.41) shows a stronger presence of noises at frequencies below 100 Hz (compared to that obtained at 244 Hz and 451 Hz). For unfiltered signal, the peaks observed at 14.5 Hz and 65 Hz are comparable in magnitude to the peak at the acoustic frequency of 860 Hz.

Figures 5.43 and 5.44 show the plots of unfiltered and filtered signals at an acoustic frequency of 2.8 kHz. After filtering, the RMS amplitude dropped from 0.9103

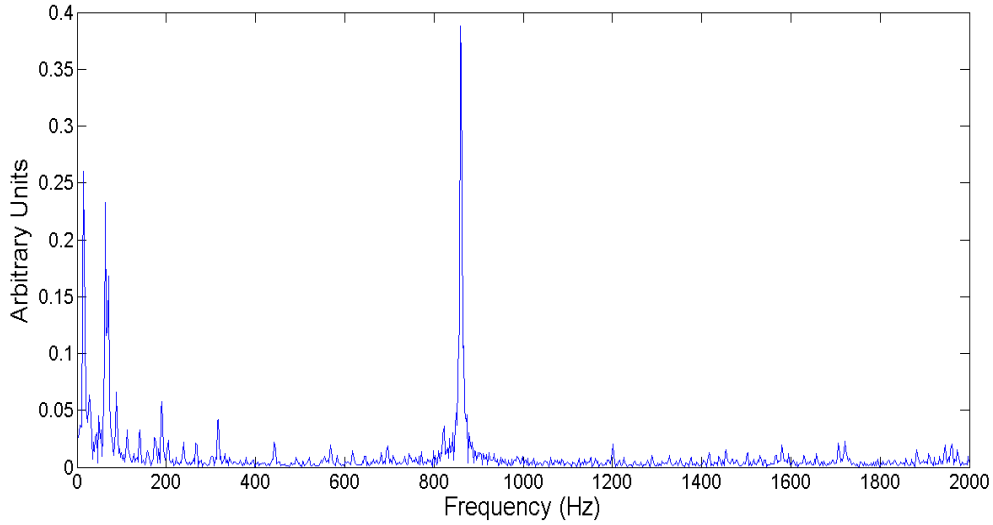

Figure 5.41: FFT analysis—unfiltered signal at an acoustic frequency of 860 Hz

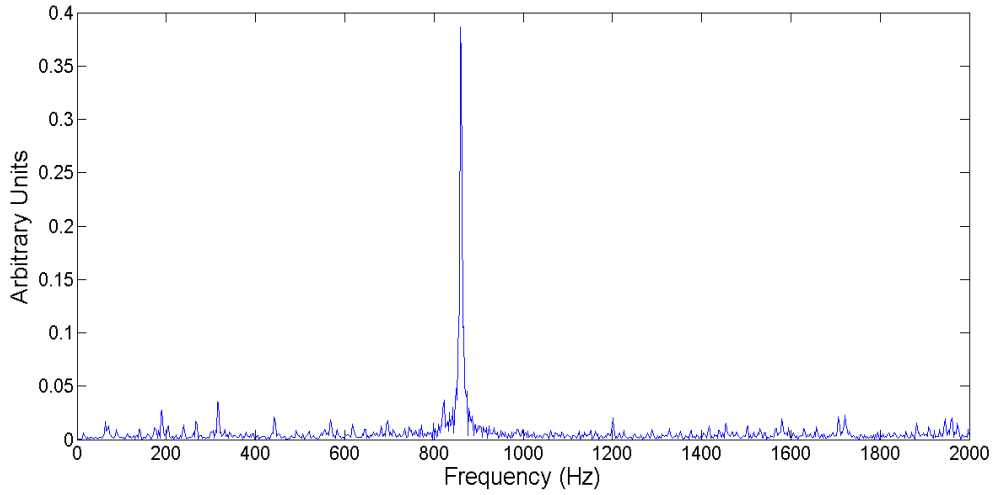

Figure 5.42: FFT analysis—filtered signal at 860 Hz (cutoff frequency = 500 Hz)

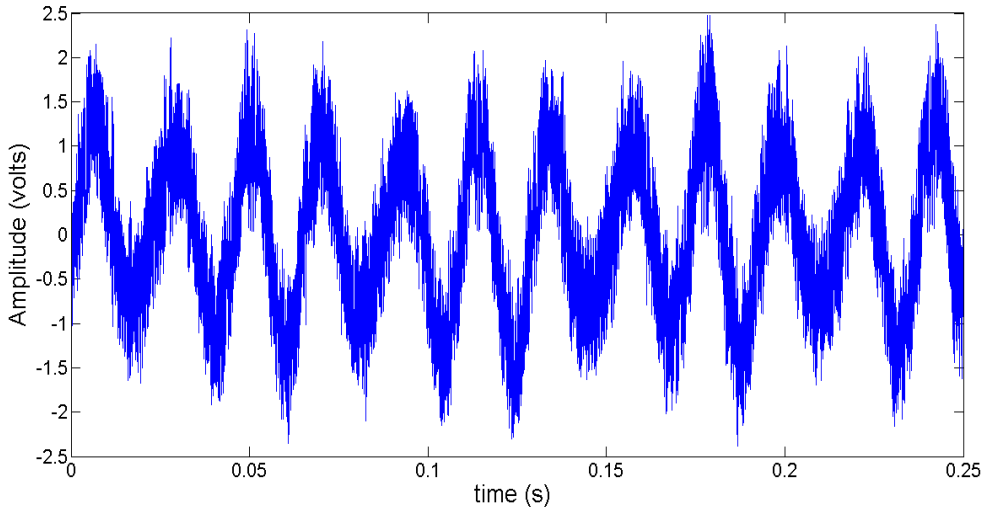

Figure 5.43: Unfiltered signal at an acoustic frequency of 2.8 kHz

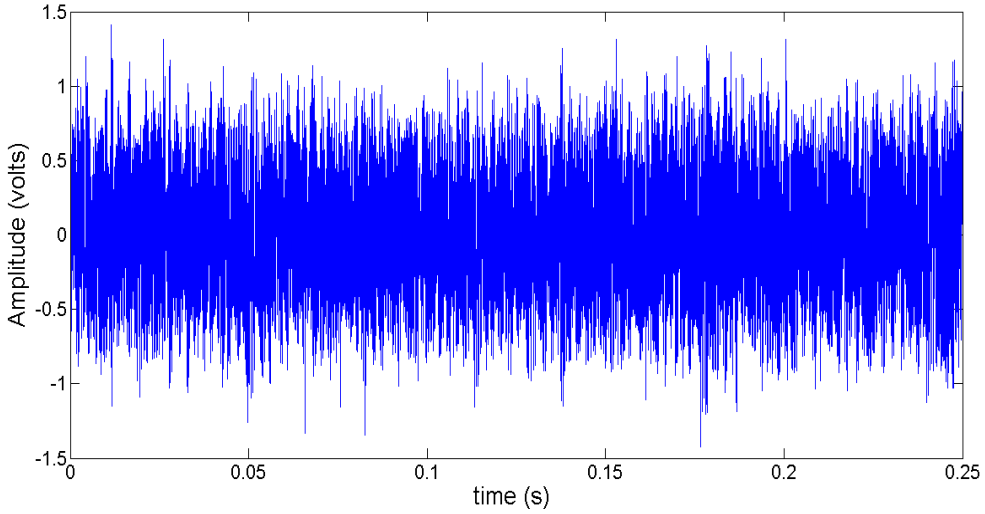

Figure 5.44: Filtered signal at 2.8 kHz (cutoff frequency = 500 Hz)

V or 83.90 dB to 0.5602 V or 80.33 dB. The drop in RMS amplitude was 62.5% in the voltage scale, considerably greater than those obtained at lower acoustic frequencies. Figures 5.45 and 5.46 show the corresponding FFT plots.

The plots for unfiltered and filtered acoustic signals at an acoustic frequency of 3.08 KHz are presented in Figures 5.47 and 5.48. The unfiltered and filtered RMS amplitudes were 0.711 V or 81.58 dB and 0.598 V or 79.95 dB, respectively, with a drop of 18.9% in the voltage scale after filtering. Figures 5.49 and 5.50 show the corresponding FFT plots. Aside from a peak at 3.08 kHz, the FFT plot in Figure 5.50 also shows a peak at 3.30 kHz. This could be due to the instability of the motor while driving the choppers at a very high rotational speed. The FFT analyses for unfiltered signals at high frequencies (above 1 kHz) also reveal that the peak frequencies of the "noise" components did not change with the chopping speed and were primarily present below 70 Hz.

Figure 5.51 shows the plot of "noise signal" due to electrical noises of the microphone and the data acquisition system, as well as mechanical vibrations of the cart arising from the rotating motion of the chopper. This signal was obtained when the lens was covered, so the signal obtained was not due to any thermo-acoustic effects. Figure 5.52 shows the corresponding FFT plot, showing a significant peak at 60 Hz, as well as several peaks below 300 Hz.

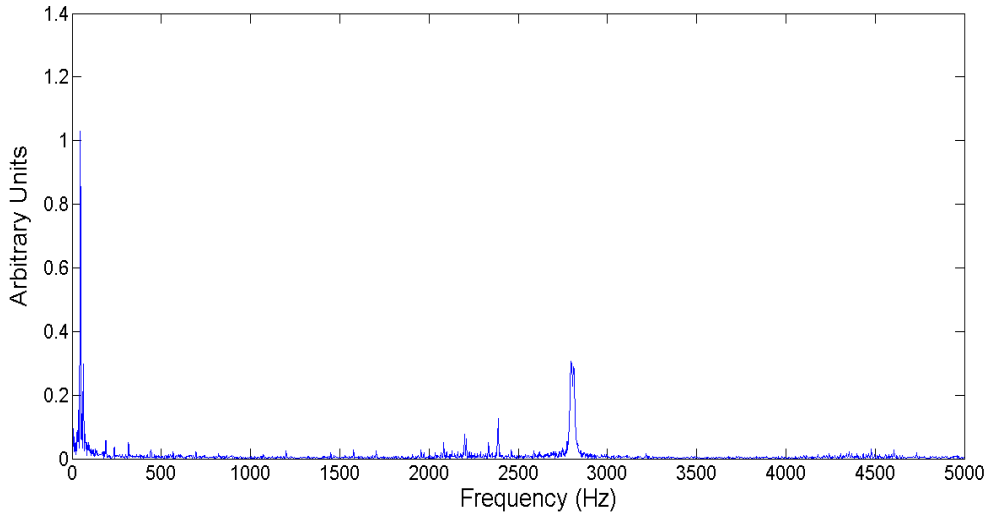

Figure 5.45: FFT analysis—unfiltered signal at an acoustic frequency of 2.8 kHz

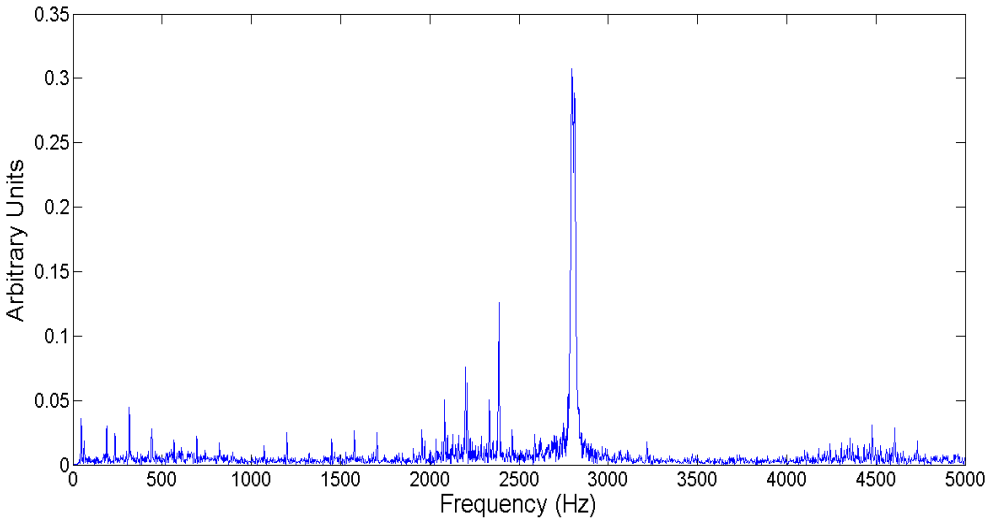

Figure 5.46: FFT analysis—filtered signal at 2.8 kHz. (filter cutoff frequency = 500 Hz)

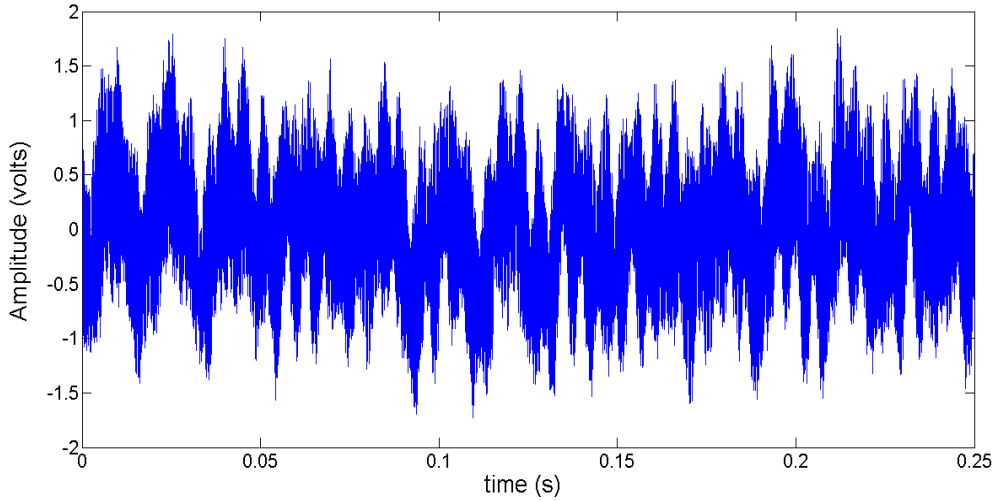

Figure 5.47: Unfiltered signal at an acoustic frequency of 3.08 kHz

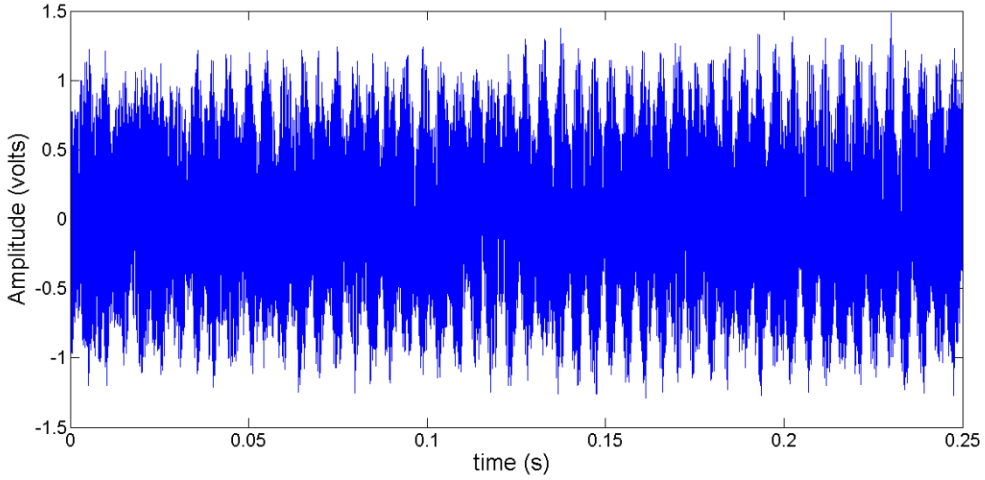

Figure 5.48: Filtered signal at 3.08 kHz (filter cutoff frequency = 500 Hz)

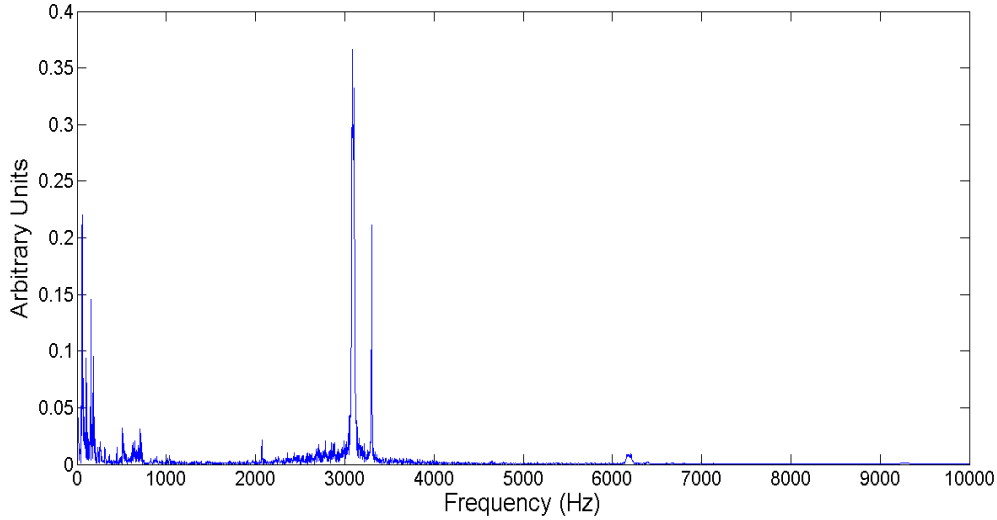

Figure 5.49: FFT analysis—unfiltered signal at of 3.08 kHz

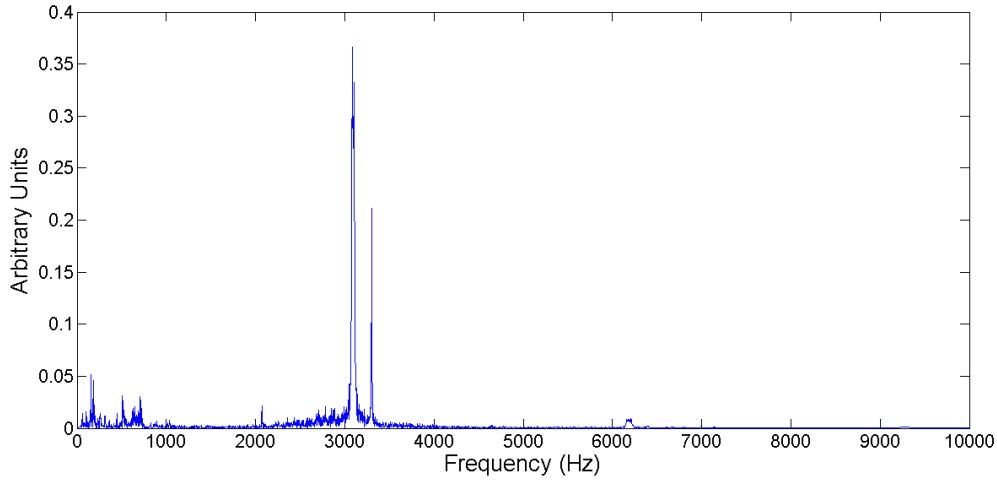

Figure 5.50: FFT analysis—filtered signal at 3.08 kHz (cutoff frequency = 500 Hz)

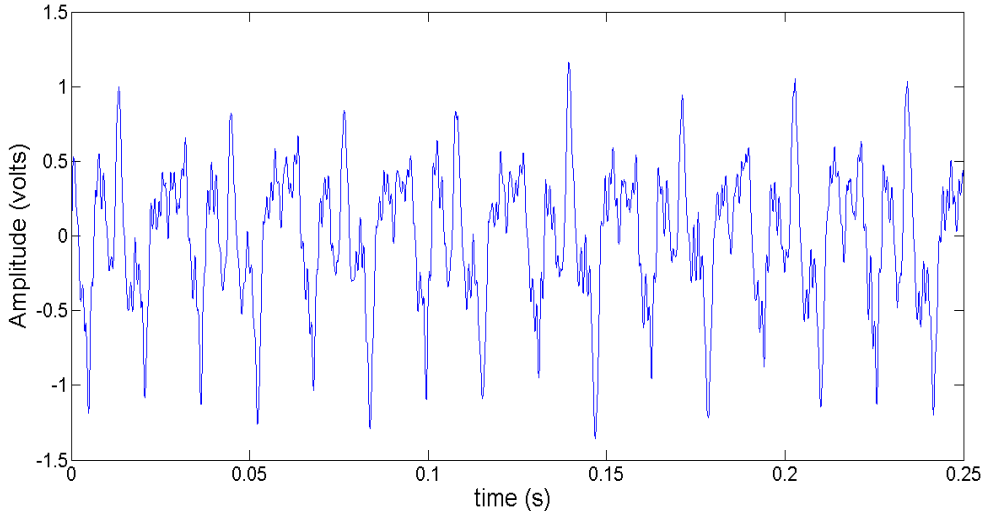

Figure 5.51: Noise due due to structural vibration

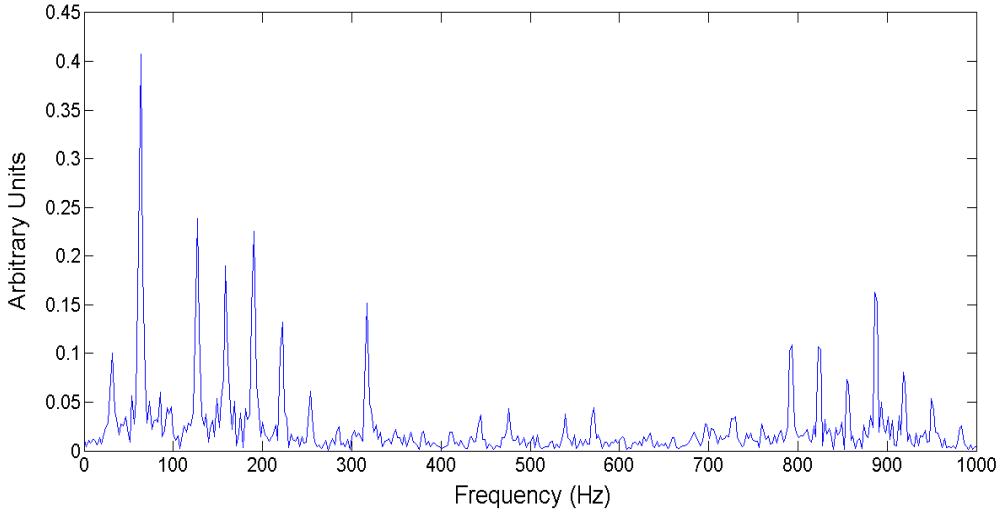

Figure 5.52: FFT analysis of the noise signal

5.5.3 Magnitude of solar radiation flux in comparison to radiation flux in IR experiments

In order to estimate the radiation flux entering through the TA converter opening, the solar to acoustic energy converter used in "outdoor experiments" was run at 92 Hz. The RMS amplitude of the signal obtained was compared to the corresponding amplitude obtained in "indoor" IR experiments at the same frequency (with the same TA converter and material configurations). The RMS amplitude of this signal was 3.85 mV (using microphone 2) or 95.90 dB (using TA converter 3, fine steel wool (grade 0000), length of steel wool = 0.8 cm). Using IR heater calibration results as presented by Chen et al. [73], the solar radiation flux entering through the TA converter opening was found to be equivalent to 67.3% IR power level (approximately 2.25×10^5 W/m^2).

The diameter of the chopper holes in the outdoor experiments (1 cm) was smaller than that used in the indoor IR experiments (2 cm). It has been mentioned in Section 5.2 that the total radiation energy entering the TA converter opening is a function of the overlapped area and the magnitude of radiation flux at a given radial location. The overlapped area (as derived in section 5.2) for indoor experiments was greater by 59.6%, compared to that in the outdoor tests.

However, the increase in overlapped area was offset by the reduced magnitude of radiation flux in indoor experiments. In addition, due to the smaller diameter of chopper holes in outdoor experiments, the heated area on the steel wool surface during the unchopped half-cycles was smaller compared to that in the indoor experiments. Consequently, in case of the outdoor experiments, the cooling of steel wool was more effective during the chopped half-cycles (as explained in Section 5.4.7.).

5.5.4 Transient behavior of thermo-acoustic signals (outdoor tests)

Compared to the "indoor" experiments, there appeared to be little "transient effect" in outdoor tests within the same time interval of 9.6 seconds. A possible explanation for this could be deduced from the discussions in Section 5.4.5. As the magnitude of solar radiation flux was greater compared to the IR radiation flux used for experiments in Section 5.4.5, there was greater difference between the temperature of steel wool and the mean temperature of air in the air column. The higher radiation flux per cycle in outdoor experiments ensured that this temperature difference remained high. As a result, amplitudes (which depend on the fluctuating or "ac" component of air) did not decrease within the given time interval (as seen in Figure 5.53).

Furthermore, the chopper holes were smaller in outdoor experiments, and so the amplitudes (which depend on the fluctuating or "ac" component of air) did not decrease within the given time interval (as seen in Figure 5.53).

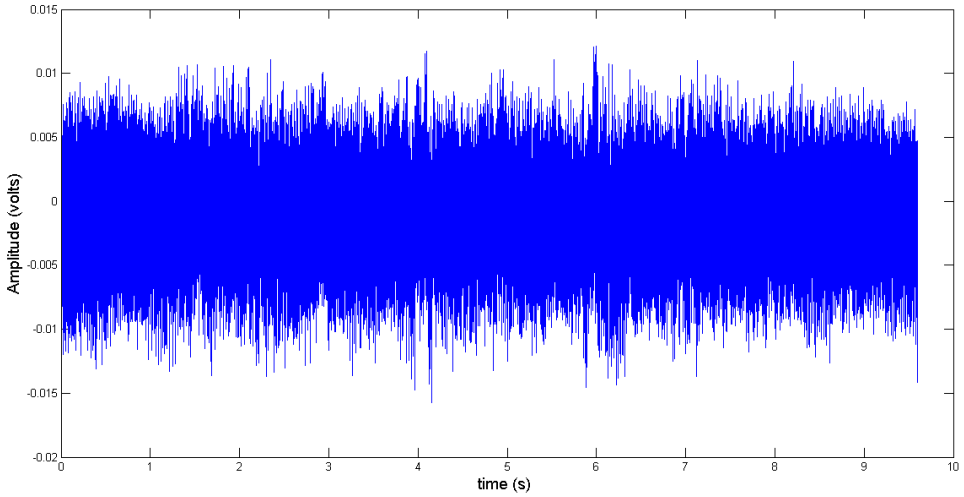

Figure 5.53: Time-domain data for 466 Hz, outdoor experiment. Configurations: TA converter 3, fine steel wool (grade 0000), length of porous material = 0.8 cm. Sampling configurations were 48000 samples at a sampling frequency of 5 kHz.

Furthermore, the chopper holes were smaller in outdoor experiments, and so the heated area on steel wool surface was also smaller. This enhanced cooling during the "chopped" half-cycles (explained in Sections 5.4.7 and 5.5.3).

5.6 Uncertainty Analysis

To verify that the experiments performed in this thesis were repeatable, the experiments were run multiple times using the same configuration. Mohammed Abidali Albonaeem, a graduate student at the University of Utah, performed "indoor" runs at an acoustic frequency of about 130 Hz using the following configuration: TA converter 2, fine steel wool (grade 0000), length of porous material = 0.8 cm, microphone 2. The microphone was located at a distance of 3.2 cm from the porous steel wool. Table 5.2 presents the results of Albonaeem's experiment for 11 samples at steady-state.

Taking Mohammed's results as the base, my experiment had a percentage difference of 2.16% and 2.106% with respect to amplitude (RMS). The uncertainty estimates for frequency and RMS voltage, based on 95% confidence levels were ± 0.405 Hz and ± 0.036 V, respectively. The uncertainty estimate for length measurements (based on 95% confidence level) was ± 0.10 cm. The uncertainties for SPL readings and IR power level measurements (as specified by the manufacturers) were 1.5 dB and 0.5%, respectively.

Table 5.2: Mean and standard deviation obtained for multiple readings

	Mean	Standard Deviation
Frequency (Hz)	130.32	0.658
THD (%)	1.898	0.4479
amplitude (millivolts)	2.31	0.0440

CHAPTER 6

CONCLUSIONS

The following conclusions can be deduced from the experimental observations:

(1) Pulsed polychromatic radiation that was incident upon a porous material inside a confined medium generated acoustic waves. The acoustic waves were generated by periodic heating of air in contact with the porous material. The frequency of the thermo-acoustic waves corresponded to the frequency at which incident IR/solar radiation was pulsed.

(2) The acoustic signals were periodic, but not perfectly sinusoidal. The sound amplitudes depended on the total radiation energy incident upon the porous material per acoustic cycle.

(3) The temperature in the confined air column varied with time and axial location. The pressure was nearly uniform at any instant of time at low frequencies.

(4) Acoustic amplitude decreased with increasing frequency within the range of 50–125 Hz for TA converter opening diameter of 1.3 cm. The frequency-amplitude relationship was affected by the dimensions of diameter of TA converter opening. When the TA converter opening was increased to 1.6 cm, the acoustic amplitudes were almost constant with respect to frequency.

(5) Acoustic signals were detected even if there was no porous material in the TA converter; however, the acoustic amplitudes generated without any porous material were comparatively much lower. This proved that periodic heat transfer between the aluminum body and air inside the air column partly contributed to the generation of thermo-acoustic signals.

(6) Acoustic amplitudes varied linearly with magnitude of incident radiation flux

(7) Porous metallic wools with high absorptivity, low filament diameter, and low interfilament spacing encouraged high acoustic waves.

(8) In the case of indoor experiments, RMS amplitudes of acoustic signals reached a peak value within the first 2 seconds of generation of TA signals. After reaching this maximum value, the amplitudes (in RMS) were observed to decrease to a steady value over a time interval much greater than the time period of the acoustic cycle.

(9) External heating of the TA-converter reduced the amplitudes of TA signals.

(10) Amplitude of acoustic signals decreased with an increase in the volume of air inside the TA-converter.

(11) The amplitude of acoustic signals increased with increasing the length of porous material up to an optimum length of about 0.75 cm. Beyond this optimum length, the amplitudes decreased with increasing length.

(12) For outdoor experiments, acoustic signals between 200 Hz and 3 kHz were generated using pulsed solar radiation (with magnitude of solar flux about 1 KW/m^2). The amplitudes of generated sound waves (in dB) decreased with frequency between 200 Hz and 1 kHz. Beyond 1 kHz, amplitudes showed little variation with frequency. The

magnitude of solar flux entering the TA converter opening corresponded to about 67.4% power level of the IR heater used in indoor experiments.

APPENDIX A

MICROPHONE CALIBRATION PLOTS

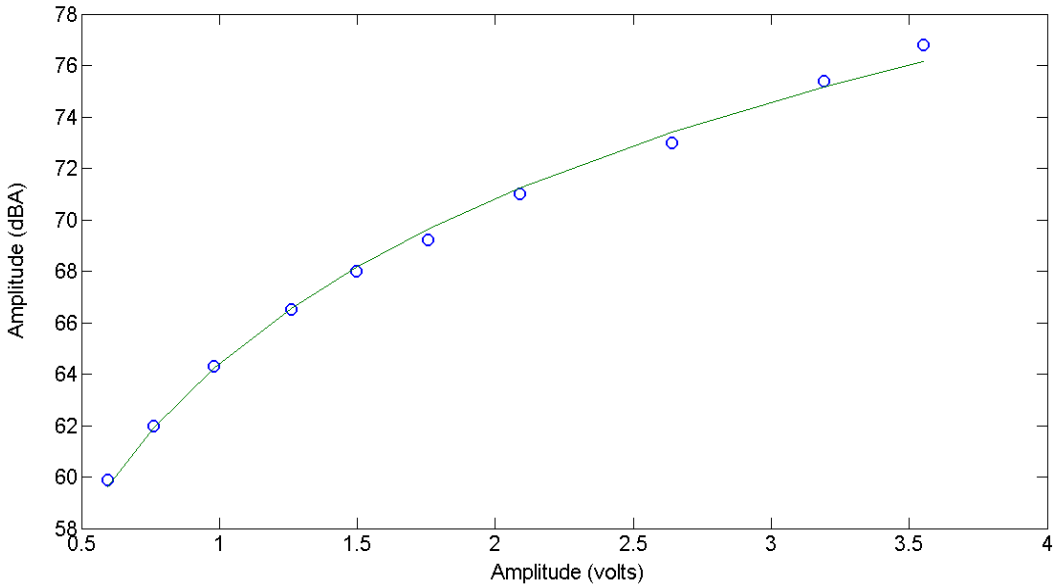

Figure A.1: Calibration plot for 100 Hz—microphone.

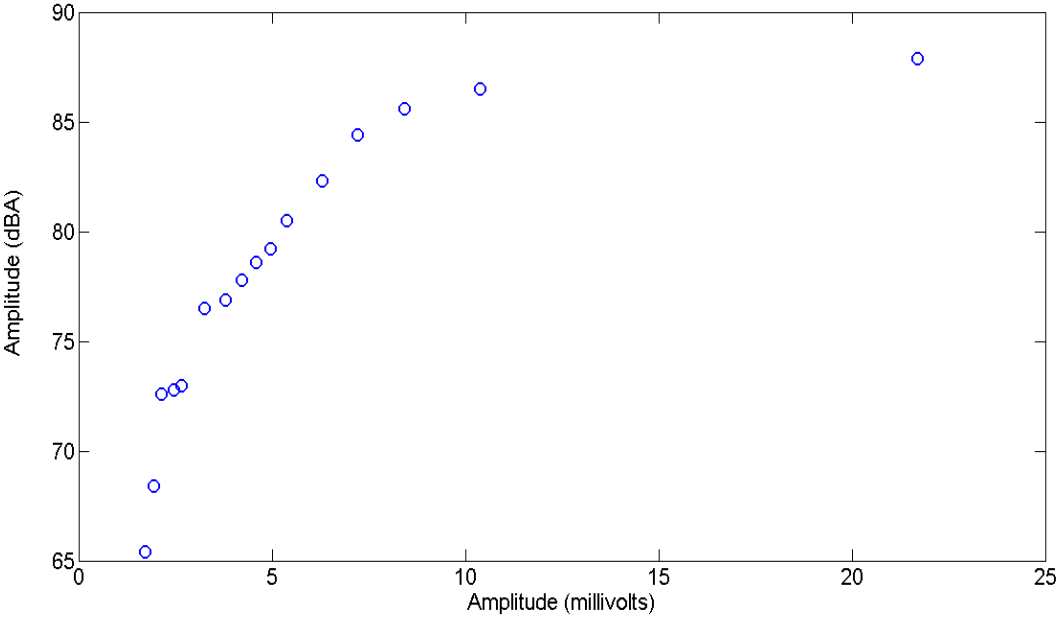

Figure A.2: Calibration plot for 100 Hz—microphone 2

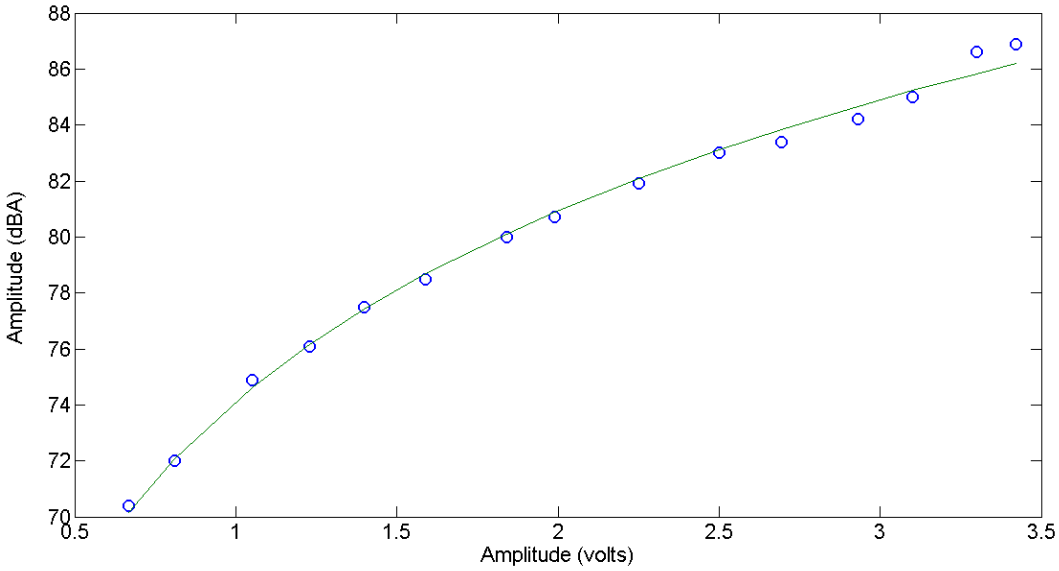

Figure A.3: Calibration plot for 200 Hz—microphone 1

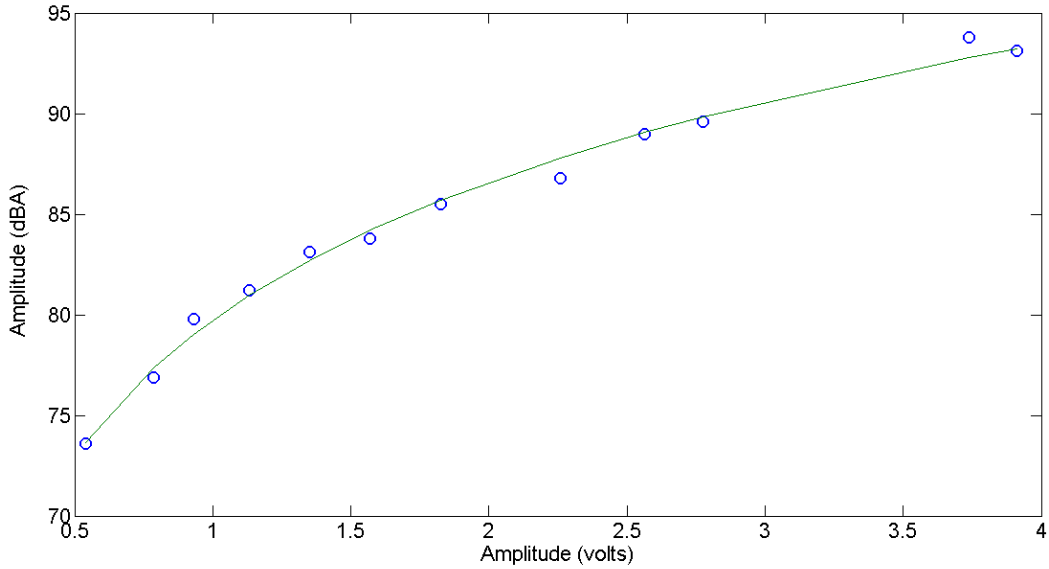

Figure A.4: Calibration plot for 400 Hz—microphone 1

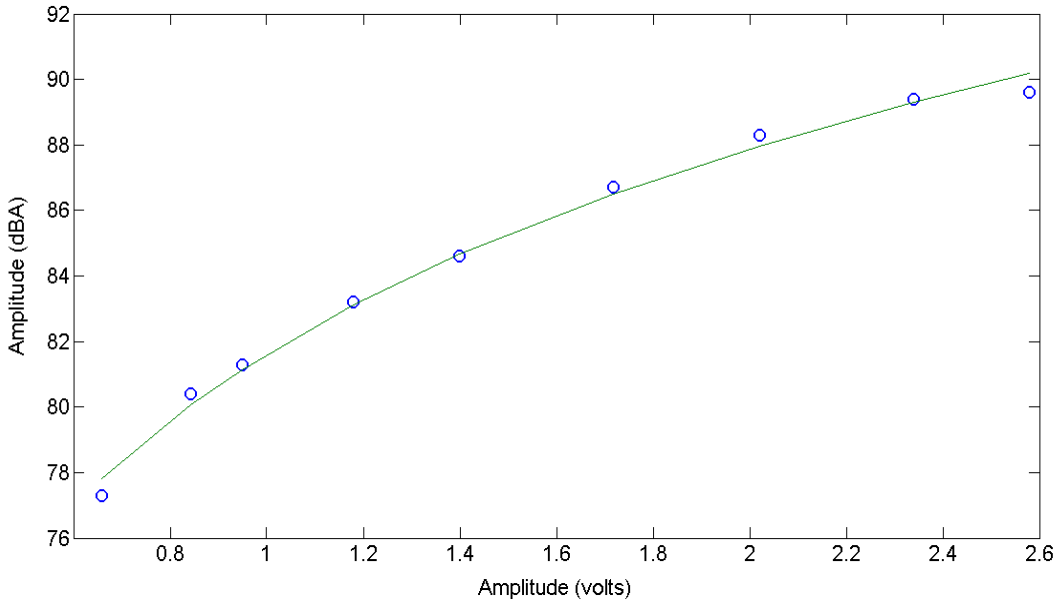

Figure A.5: Calibration plot for 600 Hz—microphone 1.

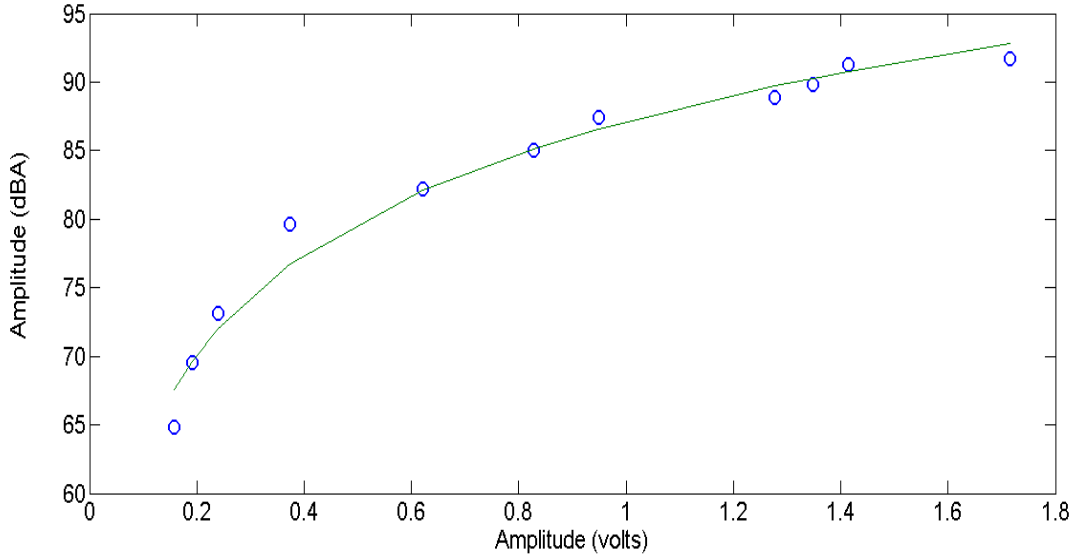

Figure A.6**:** Calibration plot for 1 kHz—microphone 1

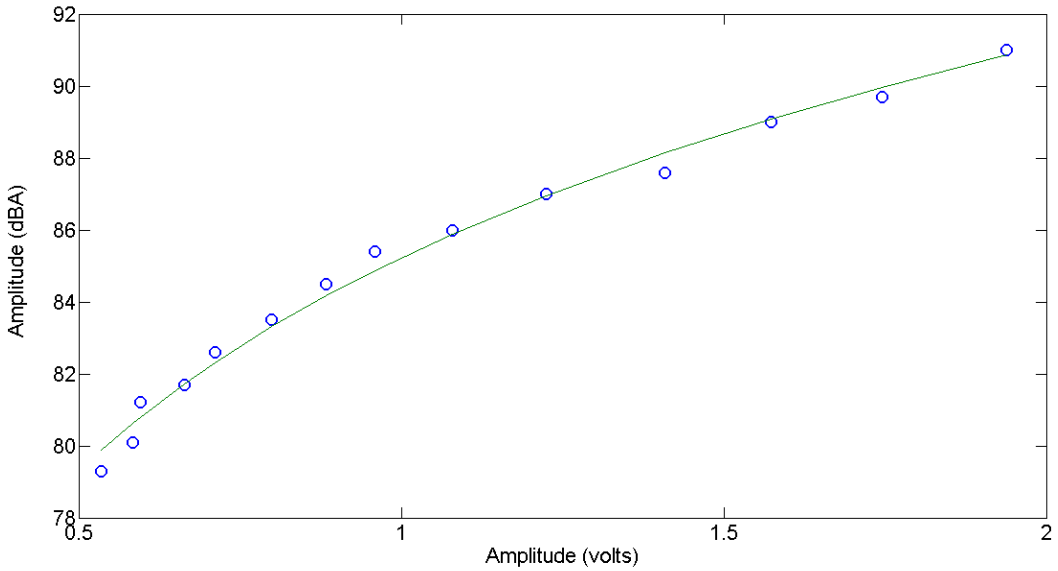

Figure A.7: Calibration plot for 2 kHz—microphone 1

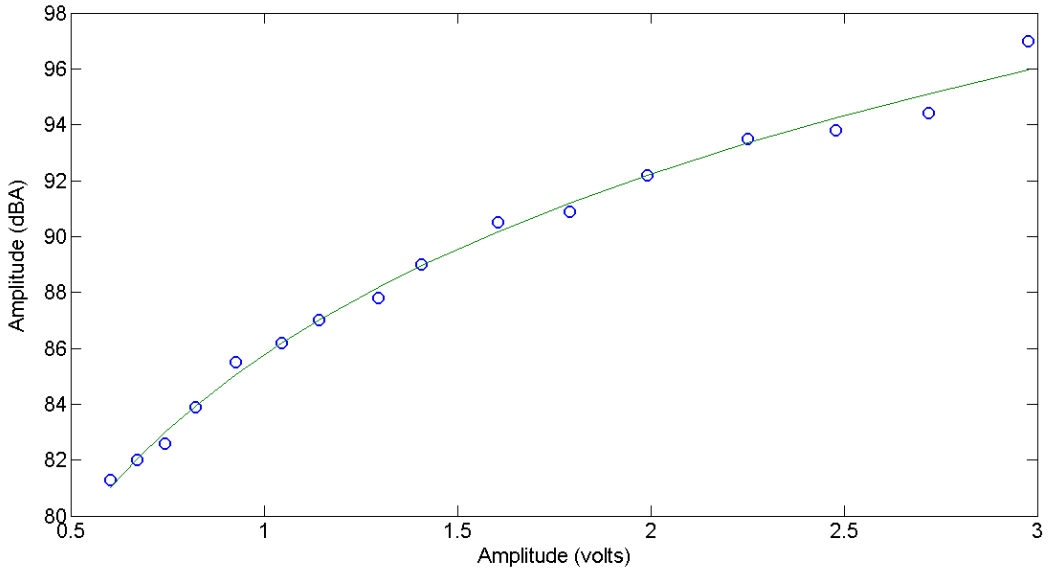

Figure A.8: Calibration plot for 3 kHz—microphone 1

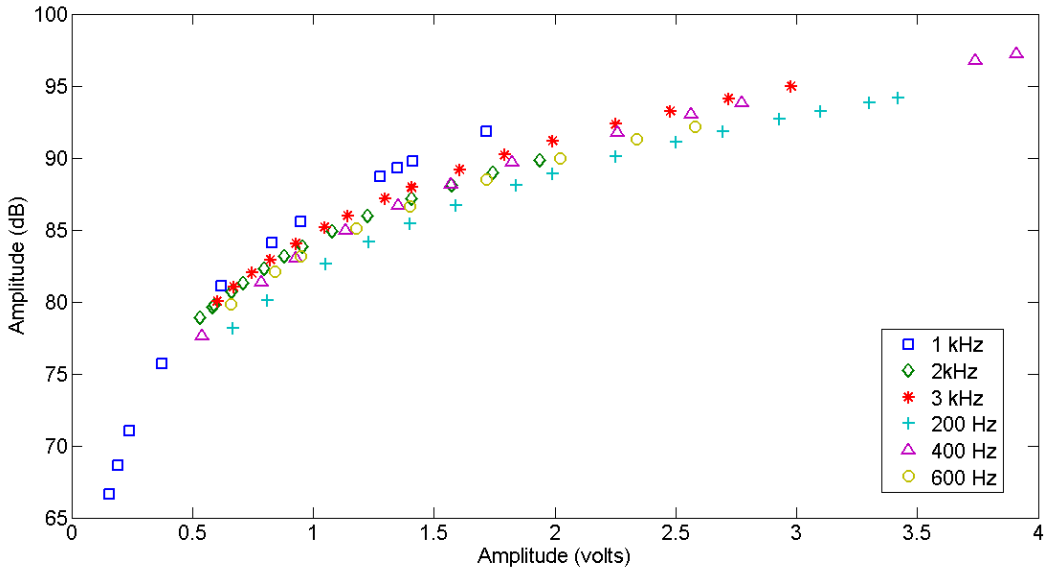

Figure A.9: Universal calibration plot—microphone 1

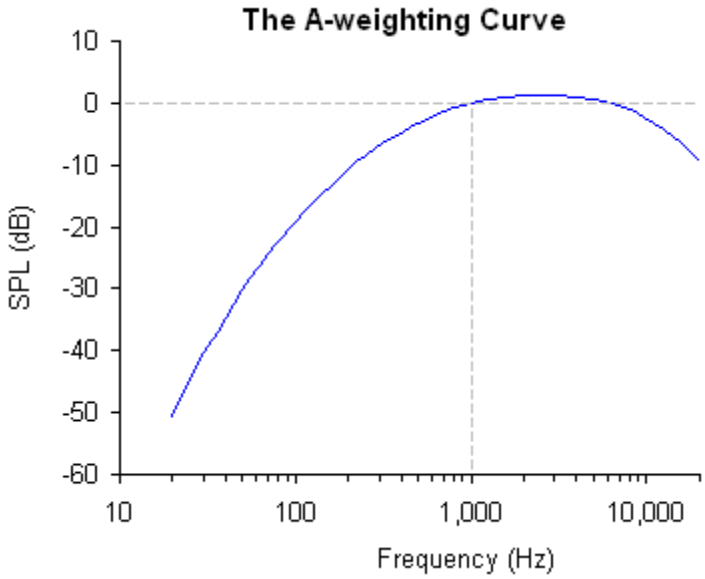

Figure A.10: A-Weighting curve

APPENDIX B

CAD DIAGRAMS OF THERMO-ACOUSTIC CONVERTERS

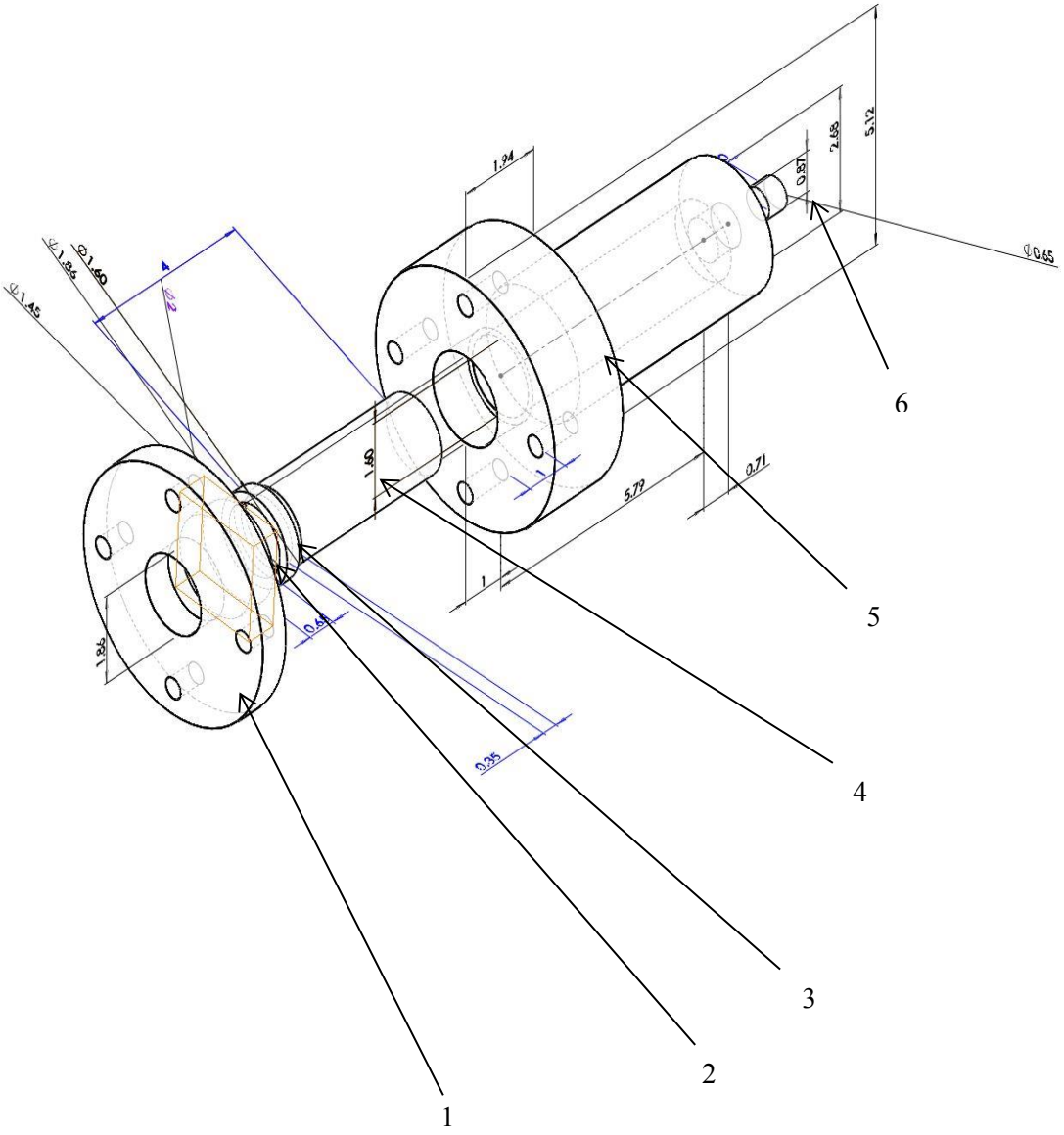

Figure B.1: 3D CAD diagram of TA converter 1. (1) TA converter cover. (2) Glass cover. (3) Silicon O-ring. (4) Steel wool. (5) TA converter housing. (6) Microphone.

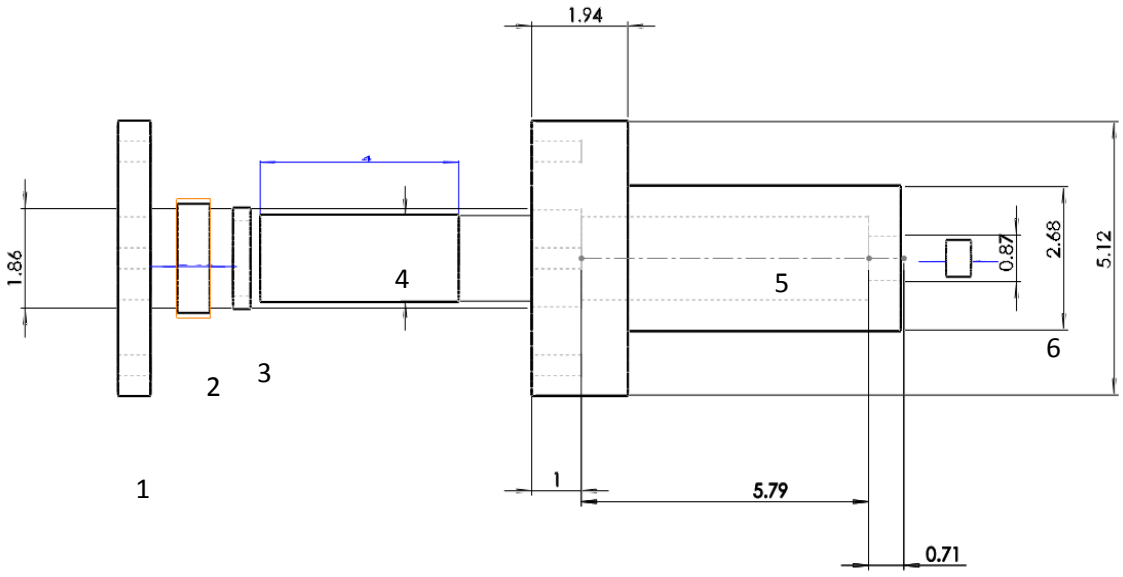

Figure B.2: Cross-sectional diagram of TA Converter 1. (1) TA converter cover. (2) Glass cover. (3) Silicon O-ring. (4) Steel wool. (5) TA converter housing. (6) Microphone.

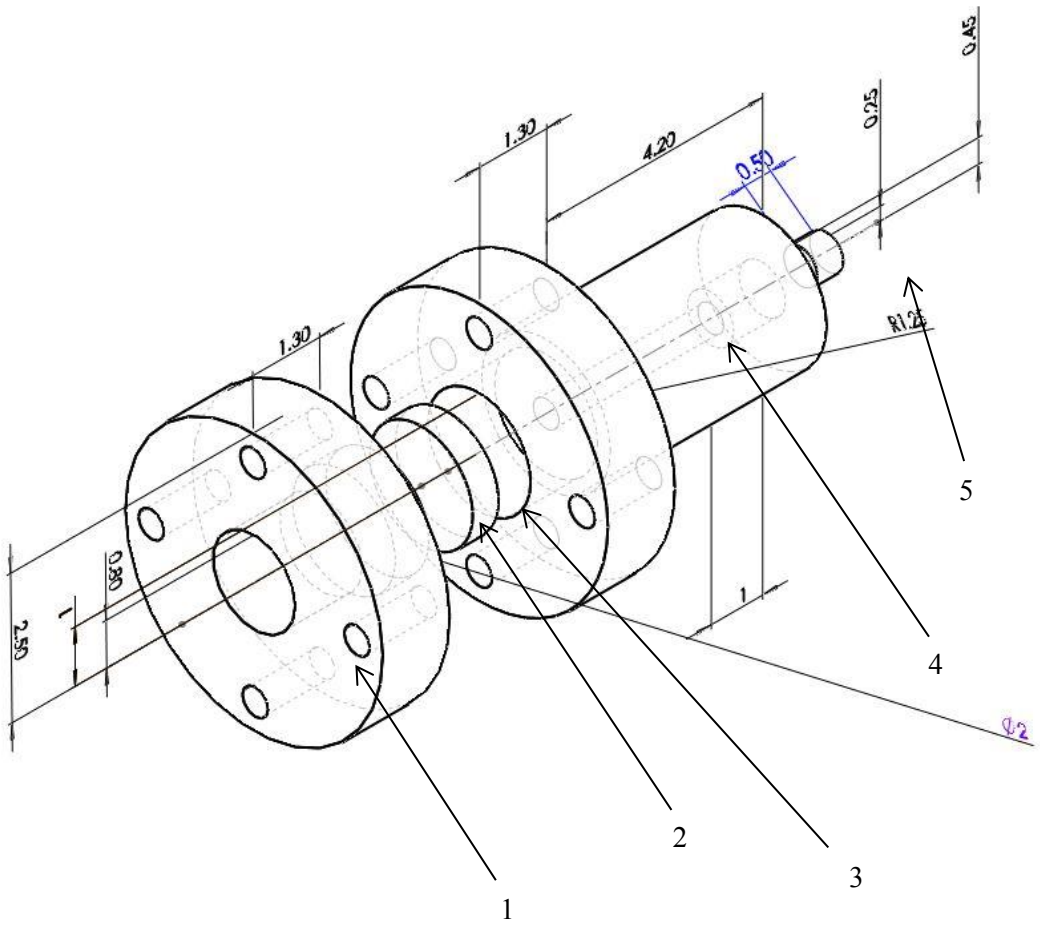

Figure B.3: 3D CAD diagram of TA Converter 3. (1) TA converter cover. (2) Glass cover. (3) Steel wool. (4) TA converter housing. (5) Microphone.

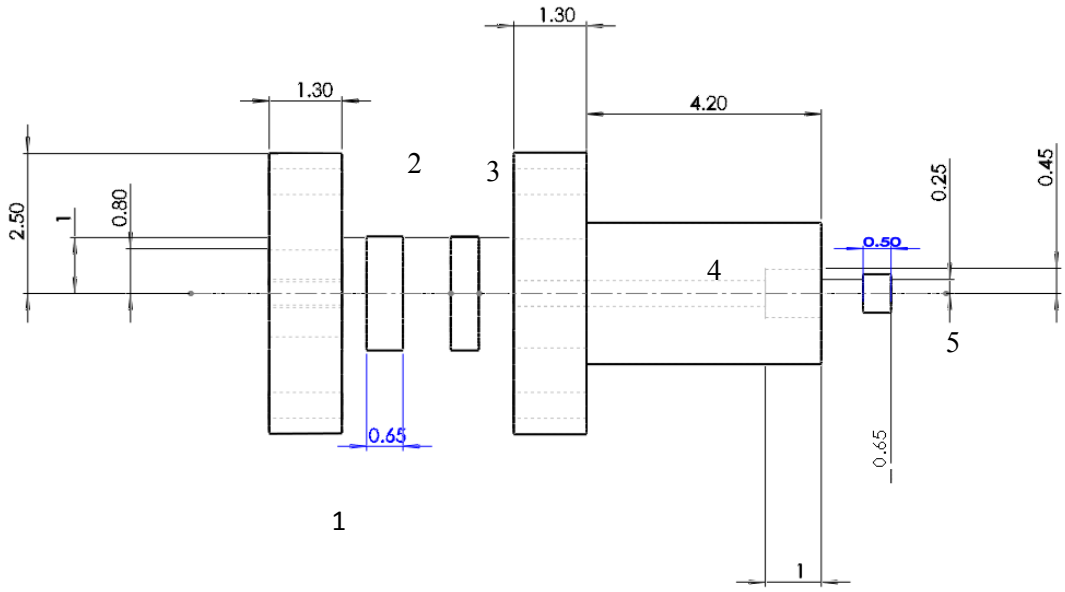

Figure B.4: Cross-sectional diagram of TA converter 3. (1) TA converter cover. (2) Glass cover. (3) Steel wool. (4) TA converter housing. (5) Microphone. (TA Converter 2 is almost identical in design to TA converter 3. The only difference between the two TA converters is the diameter of the TA converter opening, which is 1.3 cm in the case of TA converter 2.)

REFERENCES

[1] Swift, G. W., 2004, "What is Thermoacoustics?," LA-UR-04-2298, Condensed Matter and Thermal Physics Group, Los Alamos National Laboratory.

[2] Abd Settar, H. M. A., 2008, "Thermal performance of a thermoacoustic stack," M.S Thesis, University Teknologi Malaysia, Malaysia.

[3] Rayleigh, J., 1878, *The Theory of Sound*, Macmillan and Co., London, Vol II.

[4] Backhaus S. and Swift G. W., 2002, "New varieties of Thermoacoustic Engines," LA-UR-04-2298, Condensed Matter and Thermal Physics Group, Los Alamos National Laboratory.

[5] Wollan, J., Swift G. W., Backhaus S., and Gardner D. L., 2002, "Development of a Thermoacoustic Natural Gas Liquefier," AlChE *New Orleans Meeting*, New Orleans, LA.

[6] Chen, K., Oh, O. J., Lee, Y. J., Oh, W. J., Kim, K. H. and Chun, W., 2011, "Acoustic energy output and coupling effect of a pair of thermoacoustic lasers," Int. J. Energy Res. **36**(4), pp.477–485.

[7] Adeff, J. A. and Hofler, T. J., 2000, "Design and construction of solar-powered, thermo-acoustically driven, thermo-acoustic refrigerator," J. Accost. Soc. Am., **107(6)**, pp. 37–42.

[8] Keen, A. L. W. and Rilling, D., 2010, "Feasibility Study of Thermo-acoustic Laminar Flow Engine for Waste Heat Regeneration in Vehicles," *New Aspects of Fluid Mechanics, Heat Transfer and Environment*, pp. 84–88

[9] Zoontjens, L., Howard, C. and Cazzolato, B. Z. A., 2005, "Feasibility Study of an Automotive Thermo-acoustic Refrigerator," *Acoustics,* pp. 1–8

[10] Tijiani, H. and Spoelstra S., 2012, "High Temperature Thermoacoustic Heat Pump," *ICSV19,* pp.1–8.

[11] Spike, B.T., 2006, "The Photoacoustic Effect," Lecture Notes, University of Wisconsin-Madison, Madison.

[12] Bell, A. G., 1881, "Upon the Production of Sound by Radiant Energy," *Paper read before National Academy of Sciences.*

[13] Bell, A. G., 1880, Apparatus for Signaling and Communicating called Photophone, Patent no. 235,199

[14] Lyamshev, L. M., 2005, *Radiation Acoustics*, CRC Press, Moscow

[15] Pradeep, P. (Ed), 2011, *Optoelectronics – Devices and Applications*, InTech

[16] GE Energy, "Powerwave Acoustic Cleaning Systems," from www.ge-energy.com

[17] "Primasound," from http://www.primasound.gr/accoustic.html

[18] Chen, W., Hou, Y. and Hung, C., 2012, "A study of influence of acoustic excitation on carbondioxide capture by a droplet" Energy **37(**1), pp. 311–321

[19] Shabanian, J., Jafari, R. and Chaouki J., 2012, "Fluidization of Ultrafine Powders," Int. Rev. of Chem. Eng. **4**(1), pp. 16–45

[20] Ragamati, F., Ammendola, P. and Chirone, R., "Effect of Operating Conditions on CO_2 Adsorption in a Sound Assisted Fluidized Bed," *XXVI Meeting of the Italian Section of the Combustion Institute.*

[21] Raganati, F., Ammendola, P. and Chirone, R., 2013, "CO_2 Capture on Fine Activated Carbon Under Sound Assisted Fluidization Conditions," *The 14th International Conference on Fluidization – From Fundamentals to Products.*

[22] Zhu, C., Liu, G., Yu, Q., Pfeffer, R., Dave, R. N. And Nam, C. H., 2004, "Sound assisted fluidization of nanoparticle agglomerates," Powder Technol. **141**, pp. 119–123.

[23] Ammendola, P. and Chirone, R., 2010, "Aeration and Mixing Behaviors of Binary Mixtures of Nano-sized Powders Under Sound Vibration," *The 13th International Conference on Fluidization—New Paradigm in Fluidization Engineering.*

[24]"Thermoacoustic Heat Engine," Wikipedia, from en.wikipedia.org/wiki/ Thermoacoustic_heat_engine

[25] Rosencwaig, A. and Gersho, A., 1976, "Theory of Photoacoustic effect in solids," J. Appl. Phys. **47**(64), pp. 64–69

[26] Sigist, M.W., 1995, "Trace Gas Monitoring by Laser-Photoacoustic Spectroscopy," Infrared Phys. Technol. **36**(1) pp. 425–425.

[27] "Microphone Sensitivity and Conversion," Tontechnik-Rechner—sengpielaudio, from www.sengpielaudio.com/calculator-transferfactor.htm·

[28] Luft, K. F., 1943, " Über eine neue Methode der registriereden Gasanalyse mit Hilfe der Absorption ultraroter Strahlen onhe spektrale Zerlegaung," Z. Tech. Physics **24**, p. 97.

[29] Kerr, E. L. and Atwood J. G., 1968, "The laser illuminated absorptivity spectrophone: a method for measurement of weak absorptivity in gases at laser wavelengths," Appl. .Optics **7**(5), pp. 915–921

[30] Patel, C. K. N., Burkhardt, E. G. and Lambert, C. A., 1974 "Spectroscopic Measurements of Stratospheric Nitric Oxide and Water Vapor," Science **184**(4142), pp. 1173–1176

[31] Sigirist, M. W., "Laser generation of acoustic waves in liquids and gases," J. Applied Phys., **60**(83), pp. R83–R121.

[32] Fischer, C., Sorokin, E., Sorokina. I. T. and Sigirist, M. W., 2005, "Photoacoustic monitoring of gases using a novel laser source tunable around 2.5 μm," Optics and Laser in Engineering **43**, pp. 573–582.

[33] "Photoacoustic Effect," Wikipedia, from http://en.wikipedia.org/wiki/ Photoacoustic_effect.

[34] Mikolos, A., Hess, P. and Bozoki, Z., 2001, "Application of acoustic resonators in photoacoustic trace gas analysis and metrology," Rev. Sci. Instrum. **72**(4), pp. 1937–1957.

[35] Lei, G. and Di Bartolo, B., 1996, "Measurement of Rotational and Vibrational Relaxation in gases by photoacoustic resonance: Application to SF6," J. Appl. Phys. **79**(6), pp. 2890–2895.

[36] Utolia, J., 2009, "Use of Optical Cantilever Microphone in photoacoustic spectroscopy," M.S. Thesis, Department of Physics and Astronomy, University of Turku.

[37] Mota, J. P., Carvalho, J. L. C., Carvalho S. S., and Barja, P.R., 2011, *Acoustic Waves From Microdevices to Helioseismology*, Chap 13—Photoacoustic Technique Applied to Skin Research: Characterization of Tissue, Topically Applied Products and Transdermal Drug Delivery, InTech, Morn Hill, UK.

[38] Fernelius, N. C., 1980, "Extension of the Rosencwaig Gersho photoacoustic spectroscopy theory to include effects of sample coating," J. Appl. Phys. **51**(1), pp. 650–654.

[39] Benett, H. S. and Forman, R. A., 1977, "Photoacoustics methods for measuring surface and bulk absorption coefficients in highly transparent materials: theory of a gas cell," J. Appl. Phys.**15**(10), pp. 2405–2413.

[40] McDonald, F. A. and Wetsel G. C., 1978, "Generalized theory of photoacoustic effect," J. Appl. Phys. **49**, pp. 2313–2322.

[41] Park, S. M., Khan, M. I., Cheng, H. Z. and Diebold G.J., 1990, "Photoacoustic effect in strongly absorbing fluids," Ultrasonics **29**(1), pp. 63–67.

[42] Symko, O. G., 1999, "Energy Conversion Using Thermoacoustic Devices," The *18th International Conference on Thermoelectrics*, pp. 645–648.

[43] Sondhauss, C., 1850, "Über die Schallschwingungen der Luft in erhitzten Glas–Röhren und in gedeckten Pfeifen von ungleicher Weite," Ann. Phys. **155**(1), pp. 1–34

[44] Rijke, P. L., 1859, "On the vibration of the air in a tube open at both ends," Philosophical magazine **17**, pp. 419–422.

[45] Ryan T. S., 2009, "Design and Control of a Standing-wave Thermoacoustic Refrigerator," M.S. Thesis, University of Pittsburgh, Pittsburgh PA.

[46] Taconis, K. W., Beenakker, J. J. M., Nier, A.O.C. and Aldrich, L.T., 1949, "Measurements concerning the vapour-liquid equilibrium of solutions of He^3 in He^4 below 2.19 °K," Physica **15**, pp. 733–739.

[47] Rott, N., 1984, "Thermoacoustic heating at the closed end of an oscillating gas column," J. Fluid Mech. **145**, pp. 1–9.

[48] Garett, S. L., Hofler, T. J. and Perkins, D. K., 1993, "Thermoacoustic Refrigeration" 1993, *Refrigeration and Air-conditioning Workshop—Alternative Fluorocarbons Environmental Acceptability Study*

[49] Garett S. L., Hofler, T., Fitzpatrick, M., Susalla, M. P., Yolkert, R., Harris, D., Byrnes, R.B., Cameron, C.B. and Murray, F. M., 1989, "Thermoacoustic refrigerator for space applications," J. Accost. Soc. Am. **85**(48), pp. 595–599.

[50] Fahey, D., 2006, "Thermoacoustic Oscillations," Wave Motion and Optics.

[51] Garett, S. and Backhaus, S., 2000, "The Power of Sound," American Scientist **88**(6), pp. 516.

[52] The DeltaEC Home Page, "Design Environment for Low-Amplitude Thermo-acoustic Energy Conversion," from http://www.lanl.gov/projects/thermoacoustics/DeltaEC.html

[53] Backhaus, S. and Swift, G. W., 1999, "A Thermoacoustic Stirling Heat Engine," Nature **399**, pp. 355–358.

[54] Geller, D. A. and Swift, G. W., 2009, "Thermoacoustic mixture separation with an axial temperature gradient," J. Accost. Soc. Am. **125**(5), pp. 2937–2945

[55] Swift, G. W. and Geller, D. A., 2006, "Continuous thermoacoustic mixture separation," J. Accost. Soc. Am. **120**(5), pp. 2848–2857.

[56] Symko, O. G., Abdel-Rahman, R., Kwon, Y. S., Emmi, M. and Behunin, R., 2003, "Design and development of high-frequency thermoacoustic engines for thermal management in microelectronics," Microelectronics Journal **35**, pp. 185–191.

[57] Arnott, W. P, Bass, H. and Raspet, R., 1991, "General formulation of thermoacoustics for stacks having arbitrarily shaped cross-Sections," J. Accost. Soc. Am. **90**(6), pp. 3228–3237

[58] De Blok, K., 2008, "Low operating temperature integral thermo-acoustic devices for solar cooling and waste heat recovery," *Acoustics '08 Paris*.

[59] Surathu, R., 2012, "Study of Coupling Two Thermoacoustic Lasers," M.S Thesis, University of Utah, Salt Lake City.

[60] Kolhe, S., 2012, "An Experimental Investigation of Thermoacoustic Lasers Operating in Audible Frequency Range," M.S Thesis, University of Utah, Salt Lake City.

[61] "Infrafone," from www.infrafone.se

[62] Liu, J., Jie, W., Zhang, G., Zhou, J. and Cen, K., 2011, "Frequency comparative study of coal-fired fly ash acoustic agglomeration," J. Environ. Sci. Sciences **23**(11), pp. 1845–1851.

[63] Liu, J., Zhang, G., Zhou, J., Wang, J., Zhao W and Cen, K., 2009, "Experimental study of acoustic agglomeration of coal-fired fly ash particles at low frequencies," Powder Technol. **193**, pp. 20–25.

[64] Hoffman, T. L. and Kroppmann, G. H., 1997, "Visualisation of acoustic particle interaction and agglomeration: Theory Evaluation," J.Accost. Soc. Am. **101**(6), pp. 3421 –3429.

[65] Chen, W., Tsai, M. and Huang, C., 2013, "Numerical prediction of CO_2 capture process by a single droplet in alkaline spray," Appl. Energ. **109(**C), pp. 125–134.

[66] Guo, B., Chang, B. and Xiel, K., 2006, "Adsorption of Carbon Dioxide on Activated Carbon," J. Nat. Gas Chem. **15**, pp. 223–229.

[67] Arena, N., Raganati, P., Ammendola, P. and Chirone, R, "Carbon Dioxide Adsorption in a Fluidized Bed of Fine Powders," *XXIV Meeting of the Italian Section of the Combustion Institute.*

[68] Chen, K. and Rahman A., 2013, "CO_2 adsorption by acoustically and thermo-acoustically assisted fluidized bed of nano-powders," Private Communication

[69] "Engineering Toolbox," from http://www.engineeringtoolbox.com/

[70] Rodriguez, I.A., 2008, "Performance of Annular High Frequency Thermoacoustic Engines," Ph.D. Thesis, University of Utah, Salt Lake City.

[71] Bies, B. A., 1963, "Acoustic Properties of Steel Wool," J. Accost. Soc. Am. **35**, pp. 495.

[72] "Frequency and A-Weighting," Trusted Reviews, from www.trustedreviews.com/ opinions/a-silent-solution_Page-3

[73] Chen, K., Parker, N., Limb, S. H., Kim, N. J. and Chun, W., 2013, "Development and testing of a simple heat gauge for the measurement of high-intensity thermal radiation," University of Utah, Salt Lake City.

[74] Bejan, A., 2003, "Heat Transfer Handbook," Chap 13, Wiley-Interscience, New York.

[75] Liu, Q., Schlangen, E., van de Ven, M., and Poot, M, 2010, "Optimization of Steel Fiber Used for Induction Heating in Porous Asphalt Concrete," Traffic and Transportation Studies **2010**, pp. 1320–1330.

[76] Coquard, R. and Baillis, D., 2009, "Radiative properties of dense fibrous media in dependent scattering regime," Centre Scientifique et Technique du Bâtimen.

[77] "Butterworth Filters," MIT OpenCourseWare, from http://ocw.mit.edu/resources/ res-6-007-signals-and-systems-spring-2011/lecture-notes/MITRES_6_007S11_lec24.pdf.